



HAL
open science

Out of equilibrium dynamics in charged and soft matter systems

Haggai Bonneau

► **To cite this version:**

Haggai Bonneau. Out of equilibrium dynamics in charged and soft matter systems. Polymers. Université Paris sciences et lettres, 2023. English. NNT : 2023UPSLS046 . tel-04457201

HAL Id: tel-04457201

<https://pastel.hal.science/tel-04457201v1>

Submitted on 14 Feb 2024

HAL is a multi-disciplinary open access archive for the deposit and dissemination of scientific research documents, whether they are published or not. The documents may come from teaching and research institutions in France or abroad, or from public or private research centers.

L'archive ouverte pluridisciplinaire **HAL**, est destinée au dépôt et à la diffusion de documents scientifiques de niveau recherche, publiés ou non, émanant des établissements d'enseignement et de recherche français ou étrangers, des laboratoires publics ou privés.



THÈSE DE DOCTORAT

DE L'UNIVERSITÉ PSL

Préparée à l'ESPCI, laboratoire Gulliver

**Dynamique hors équilibre dans les systèmes chargés et de
matière molle**

**Out of equilibrium dynamics in charged and soft matter
systems**

Soutenue par

Haggai Bonneau

Le 29 Septembre 2023

École doctorale n°564

Physique en Île-de-France

Spécialité

Physique

Composition du jury :

Mme. Cécile APPERT-ROLLAND Laboratoire de Physique des 2 Infinis Irène Joliot-Curie	<i>Présidente</i>
M. Ralf BLOSSEY L'Unité de Glycobiologie Structurale et Fonctionnelle Lille	<i>Rapporteur</i>
M. Manoel MANGHI Laboratoire de Physique Théorique Toulouse	<i>Rapporteur</i>
M. David DEAN Laboratoire Ondes et Matière d'Aquitaine	<i>Examineur</i>
Mme. Hélène BERTHOUMIEUX Laboratoire Gulliver, ESPCI	<i>Invitée</i>
M. Vincent DÉMERY Laboratoire Gulliver, ESPCI	<i>Co-directeur de thèse</i>
M. Élie RAPHAËL Laboratoire Gulliver, ESPCI	<i>Directeur de thèse</i>

Résumé

L'objet de cette thèse est l'étude théorique de trois problèmes croisés en physique statistique hors équilibre. Le premier concerne l'étude de la réponse temporelle d'un système ionique soumis à une variation brusque d'un champ électrique extérieur. En particulier, nous étudions le comportement des fonctions de corrélation densité-densité et des courants électriques induits. En nous appuyant sur la théorie de la densité fonctionnelle stochastique et en intégrant les interactions hydrodynamiques, nous effectuons une étude complète du courant électrique total en fonction des corrélations ioniques. Nous montrons que les corrélations ne suivent pas la même trajectoire lorsque le champ est activé ou désactivé. Ainsi, le courant décroît exponentiellement lorsque le champ est désactivé, alors qu'il décroît algébriquement jusqu'à sa valeur stationnaire lorsque le champ est activé. Cette différence est due à un effet non linéaire. De plus, nous démontrons que le comportement à long terme des corrélations est dominé par un processus de diffusion anisotrope, ce qui explique la décroissance algébrique des courants. Le deuxième problème explore la diminution anormale de la température de transition vitreuse observée dans les films minces de polymères autoportés de haut poids moléculaire. En considérant les statistiques exactes de marches aléatoires de taille finie confinées entre deux plans, nous évaluons de manière critique le mécanisme original de relaxation proposé par de Gennes. Nos résultats indiquent que ce mécanisme ne permet pas d'expliquer les principales caractéristiques observées dans les expériences et qu'une nouvelle approche théorique s'avère donc être nécessaire. Enfin, le troisième problème se trouve dans l'étude des écoulements granulaires denses le long de plans inclinés. En analysant les simulations obtenues par la méthode des éléments discrets, nous retrouvons les caractéristiques essentielles des écoulements granulaires, notamment l'existence d'une contrainte critique, le profil de vitesse de Bagnold et des lois de frottement et de dilatation distinctes. Notre analyse microscopique détaillée met en évidence la formation d'amas de grains. Ces connaissances permettent le développement d'un modèle théorique de lois d'échelle, offrant une meilleure compréhension des principes régissant les écoulements granulaires denses.

Abstract

In this thesis, we examine three interrelated problems within the domain of non equilibrium statistical physics using theoretical tools. These problems share the existence of long range correlations where stationary flows and disorder prevent reaching an equilibrium state. Using the distinct properties of these systems we explore different aspects of non equilibrium states. The first problem centers around the examining temporal responses of ionic systems, subject to a quench of an external electric field. In particular, we study the response of the density-density correlation functions and induced electric currents. Leveraging Stochastic Density Functional Theory and integrating hydrodynamic interactions, we analyse the total electric current as a function of ionic density-density correlation functions. The correlations do not follow the same trajectory when the field is switched on or off. Accordingly, the current decays exponentially when the field is switched off, yet it relaxes algebraically to its stationary value when the field is switched on, rooted in a non-linear effect. Moreover we demonstrate that the long range behavior of the correlations is dominated by an anisotropic diffusion process, which accounts for the algebraic decay of the currents. The second problem explores the anomalous decrease in the glass-transition temperature observed in thin freestanding polymer films of high molecular weight. We critically assess the de Gennes' sliding mechanism, which proposes a hypothetical relaxation mode by considering the exact statistics of finite-sized random walks confined between two planes. Our findings challenge the hypothesis, indicating that the sliding mechanism cannot capture the main features observed in the experiments, thus necessitating a new theoretical approach. The third problem revolves around the study of dense granular flows down inclined planes. Analyzing discrete element method simulations, we recover critical features of granular flows; including the existence of a critical stress, the Bagnold velocity profile, and distinct friction and dilatancy laws. Our microscopic analysis uncovers the formation of grain clusters. These insights permit the development of a theoretical scaling model, providing a comprehensive understanding of the principles governing dense granular flows.

Keywords: Non-equilibrium statistical physics, electrolytes, polymers, granular matter, soft matter

Acknowledgments

I would like to express my sincere gratitude to those whose invaluable contributions have played a vital role in the completion of this thesis and have made my Ph.D. journey an enjoyable one.

First and foremost, my deep gratitude goes to my Ph.D. supervisors, Élie Raphaël and Vincent Démery. They introduced me to the world of soft matter and statistical physics, shared their knowledge, and gave me helpful advice as well as the freedom to make mistakes and explore independent research directions. I am thankful that they accepted me as their student.

I was also fortunate to work closely with Thomas Salez and Pascal Damman. Their elegant approach to seemingly complex problems was inspiring. Of course, their motivation to share a meal or drinks doesn't fall short. The work presented in this thesis has benefited greatly from insightful discussions with Michael Schindler, Michel Fruchart, and Tal Agranov. I am very grateful for their support and friendship.

In addition to my direct research collaborators, many people have made my Ph.D. studies a memorable and enjoyable experience. I am grateful to the staff at ESPCI, especially Elisa Silvera, who helped me navigate the French bureaucracy.

My time at ESPCI would not have been the same without the moral support and companionship of my friends and fellow students: Coline, Paul, Thibault, Vincent, Hedi, Charles, Mats and Armand. I am grateful for their constant support and encouragement at times when I felt stuck.

I would like to thank my parents, Avigail and Phillippe, for their endless support and encouragement, even when it meant flying far away. To my friends back home, in particular Nadav, Yael, Tal, Inbar, Omer³ and Amit. I am thankful for the many hours spent on video calls, bridging the geographical gap. Special thanks to Zoe Piran for her help in giving this manuscript its final form with her LaTeX skills. I am especially grateful to Elya Assayag for supporting my Ph.D. journey and making it feel achievable.

Finally, my sincere appreciation goes to the reviewers and jury members - Ralf Blossey, Manoel Manghi, Cécile Appert-Rolland, David Dean, and Hélène Berthoumieux - for investing their time and expertise in reviewing this thesis. Their contributions have enriched the quality of this work. I'd like to acknowledge the financial support of the UHJ-France association and the Scopus Foundation as well as the Ecole Doctorale ED564 'Physique en Ile de France'.

Contents

Introduction	7
I Of currents and correlations in ionic systems	9
1 Background on ionic systems	10
1.1 Electrolytes	11
1.2 Electrostatics of ionic solutions	12
1.2.1 Poisson-Boltzmann Theory	12
1.2.2 Debye-Hückel theory and the Debye length	13
1.3 Dynamics of electrolytes	14
1.3.1 Poisson-Nernst-Planck equation	14
1.3.2 Conductivity of electrolytes	15
1.3.3 Stochastic density functional theory	17
1.4 Hydrodynamic interaction	19
1.4.1 Stokeslet	19
1.5 Recent developments	20
2 Temporal response of the conductivity	22
2.1 Model	22
2.2 Correlations and electric current	24
2.2.1 Closed equations for the density fields	24
2.2.2 Average electric current from correlations	24
2.2.3 Correlations in the Debye-Hückel limit	26
2.3 Binary monovalent electrolyte	27
2.4 Dimensionless form	28
2.4.1 Correlations from equilibrium to NESS and back	29
2.5 From NESS to equilibrium	30
2.6 From equilibrium to NESS	31
2.6.1 Electrostatic correction	31
2.6.2 Hydrodynamic correction	35
2.7 Conclusions	38
3 Correlations in electrolyte systems – Long range behavior	39
3.1 Stationary case	39
3.1.1 Discontinuity at small wave number	40
3.1.2 quadrupole potential	42

3.2	Time dependent correlations	44
3.3	Equation for the long range correlations	48
3.3.1	Coarse grained equation	48
3.3.2	Relaxation rates of the conductivity	49
4	Perspectives	51
5	Appendix – Part I	53
5.1	Correlations	53
5.1.1	NESS to Equilibrium	53
5.1.2	Equilibrium to NESS	53
5.2	Derivation of the equation for the correlations	53
5.3	Regularity of the integrands from Equilibrium to NESS	54
II	Dense flow of granular matter	55
6	Introduction to granular media	56
6.1	Flow regimes	57
6.2	Friction in granular media	58
6.3	Athermal system	59
6.4	Jamming transition	60
6.5	$\mu(I)$ Rheology	61
6.6	Bagnold flow profile	62
7	Microscopic picture of the $\mu(I)$ rheology for dense granular flows on inclined planes	65
7.1	Simulation of the inclined plane	66
7.2	Theoretical analysis	69
7.3	Microscopic picture	73
7.4	Discussion	74
8	Appendix – Part II	76
8.1	Friction	76
8.2	Bagnold-like flows	77
8.3	Velocity correlations and diffusion	78
III	Polymer glasses and confinement	79
9	Basic concepts in glass and polymer physics	80
9.1	Glass Transition	80
9.1.1	Thermodynamic point of view	82
9.1.2	Dynamics	82
9.2	Polymer physics	85

9.2.1	Molecular weight	85
9.2.2	Gaussian chains	86
9.2.3	Persistence length	87
9.2.4	Polymer melts	88
9.2.5	Glass transition in polymers	88
9.3	Measuring the glass transition temperature	89
10	On the bridge hypothesis in the glass transition of freestanding polymer films	90
10.1	Thin glassy films	90
10.2	Sliding mechanism	93
10.3	Bridge statistics	94
10.4	Finite-size sliding mechanism	96
11	Perspective	98
11.1	Discussion	98
11.2	Proposed experiment	99
11.3	Conclusion	99
12	Appendix – Part III	101
12.1	Exit probabilities	101
	Bibliography	102

Introduction

A primary goal of statistical physics is to explain and predict the large-scale behaviors of interacting systems through the use of mathematical models and physical arguments. In systems where the degrees of freedom are weakly correlated, a simplified description using mean-field analysis often suffices [1]. This method seeks to reduce the influence of individual degrees of freedom to attain a system-wide perspective. Nevertheless, when fluctuations and correlations are significant, the coarse-grained distributions follow scaling functions, demanding more advanced field-theoretical techniques [2].

In equilibrium statistical mechanics, all thermodynamics properties are derived from the partition function. For a given Hamiltonian, the partition function can be computed approximately or exactly in certain cases. The situation is very different in non equilibrium statistical mechanics, where probability densities are not known and macroscopic quantities depend on the dynamics of the systems. One finds a variety of approaches to deal with these complications, but no universal procedure.

Away from equilibrium and in dynamical situations, strong correlations are common, giving rise to a variety of scaling behaviors. Such behaviors have been observed in numerous physical, biological, social, and financial systems [3–8]. This observation has been particularly relevant in recent times due to the advent of more advanced theoretical tools and computational methods.

This thesis discusses three physical systems that are fundamentally out of equilibrium, (I) driven electrolytes, (II) flow of granular matter, and (III) thin films of polymer glass. Notably, each system provides a unique setting, differing in the manner in which it exhibits non equilibrium. While all systems have been deeply studied over the last decade, many open questions are still waiting to be addressed. Here we utilize the distinct properties of each system to uncover different aspects of non equilibrium scenarios, as detailed bellow.

The study of the first system we address, electrolyte solutions, marks an early application of techniques provided to deal with non-equilibrium systems. Of the three types, this system stands out because it is capable of exploring the phase space relatively quickly and then reach a non-equilibrium steady state (NESS). In such states, the driving and dissipation balance each other out and the macroscopic quantities are independent of time. The driving and dissipation can come in many forms, heat or particles source and sink, external driving field and friction and so on. In Part I of this thesis we study the trajectory towards NESS, which so far has not been thoroughly analyzed. We present a novel approach to study the temporal response of ionic systems when driven out of equilibrium.

The second and third systems we consider, granular materials and polymers respectively, belong to a class of systems that exhibit jamming, or a glass transition i.e. a transition from a fluid-like to a disordered solid-like state that occurs out of thermal equilibrium. During the transition, the dynamics slow down dramatically and the system is unable to explore its phase space. The nature of the glass transition, and whether or not it is even a phase transition is one of the most important open questions in statistical physics. Granular matter propose even a larger challenge as it is a system which is indifferent to temperature at both sides of the transition. In such “athermal” system, the particles do not perform Brownian motion; they are only driven by external forces such as compression or shear.

In Part **II** we address the flow of granular matter over an inclined plane, which is a canonical setup in the study of granular systems. We propose a theoretical scaling model to rationalize some of the observed non local properties. This model provides a step towards understanding the underlying flow mechanism at a stationary state. Lastly, in Part **III** we consider polymer glasses under confinement. We question the de Gennes’ sliding model, which is an important hypothesis of an alternative relaxation process in thin polymer glasses. We show that the suggested sliding mechanism cannot reproduce the basic features appearing in the experiments. We further explore the model properties and provide the fundamental reasons which prevent it from reproducing the discussed features.

Author’s contribution

The work presented in this thesis was done under the supervision of Élie Raphaël and Vincent Démery, and in collaboration with Thomas Salez (Parts **II**, **III**) and Pascal Damman (Part **II**) as well as with Denis Dummont (Part **II**), James A. Forrest and Maxence Arutkin (Part **II**). Part **II** of this thesis contains a substantial part of numerical simulation, I did not contribute to their implementation and execution. Chapter 2 is based on the publication [9], Chapter 7 is based on [10] and Chapter 10 is based on [11].

Part I

Of currents and correlations in ionic systems

Chapter 1

Background on ionic systems

The study of electromagnetic phenomena stands as one of the pillars of modern science, technology, and engineering. This journey, which began centuries ago, has fundamentally changed our understanding of the world. Our story begins at this pivotal point, with the invention of the electric cell, by Galvani and Volta [12,13] at the end of the 18th century. The invention of the electric cell provided stable currents for electromagnetic experiments and established a link between chemical reactions and electricity. Faraday then formulated electrochemical terminology and defined the relationship between the mass and charge of ions transferred during electrolysis. However, he maintained that an applied voltage merely released ions from chemical compounds.

In parallel, the development of thermodynamics and kinetic theory was inspired by the study of heat engines and various states of matter. Early models by Arrhenius and Van 't Hoff treated ionized salts as an ideal gas [14,15]. This concept was validated by Raoult, who experimentally confirmed that mixtures of solutions followed the ideal gas law by measuring their partial pressure [16]. However, deviations from the ideal gas law even at low salt concentrations were observed. Kohlrausch noted that the molar conductivity of ions decreases with increasing salt concentration [17], suggesting a dependence on the cube or square root of the concentration. Initially, the decrease in conductivity was attributed to an increase in association at higher concentrations. This effect is relevant for weak electrolytes such as acetic acid and ammonia in water. Yet, studies by Sutherland and later by Bjerrum demonstrated that strong electrolytes – a different class of electrolytes – have a negligible degree of association [18,19].

The above led to the introduction of the Debye-Hückel model, a cornerstone of statistical physics [20]. Debye and Hückel understood that although ions are generally randomly distributed, there are strong positional correlations between anions and cations, with each ion being surrounded by an atmosphere of opposite but equal charge. This ionic atmosphere effectively screens the central charge, causing the effective potential to decay exponentially at large distances. Although the model is accurate in some respects, it predicted incorrect prefactors for the square-root dependence of conductivity on density. This discrepancy was corrected by Onsager, who introduced the “limiting law for the conductivity of strong electrolytes” [21]. Bjerrum introduced the first correction to the Debye-Hückel theory by including neutral pairs bound by the Coulomb interaction [22]. Subsequent improvements

to the theory of conductivity followed, including the theory by Fuoss and Onsager [23], which extends the Kohlrausch law to higher orders in the concentration of ions at infinitesimal external field, and the theory by Wilson to calculate the dependence of conductivity on the external electric field but at low ion concentration [24]. For a comprehensive overview see [25, 26].

In general, physical systems in which the interaction between particles is governed by a potential that satisfies a Poisson equation are called Coulomb gases. In d dimensions it decays with distance as $1/r^{d-2}$ and is prevalent in nature, for example in gravitational systems and plasmas [27, 28]. In addition, the Poisson equation also governs the long-time limit of a diffusion process with source terms; as such, collections of living or synthetic particles interacting through diffusive fields can also be considered as Coulomb systems in certain regimes [29]. Electrolytes are the first and perhaps best known example of a Coulomb gas.

1.1 Electrolytes

Electrolytes are substances that conduct electricity and are composed of a medium that contains charged particles, typically a solvent with dissolved salt. Electricity is conducted through the movement of the charged particles, not free electrons. The degree of ionization when an electrolyte is dissolved classifies it as either strong or weak. The properties of an electrolyte are determined by the properties of its constituent ions and the solvent. Typically, ions have complex properties such as size, shape, density, and charge magnitude and distribution. Nevertheless, an ion is often accurately represented by its diameter a and its charge, which is an integer multiple z of the elementary charge q . Similarly, the solvent, often with non-trivial charge distributions and orientation dynamics, can be approximated as a continuum with permittivity ε . The hydrodynamic properties of the solvent are characterized by its dynamic viscosity and density. A small ionic diameter typically results in a very low Reynolds number, meaning that hydrodynamic effects are adequately described by an incompressible laminar flow [30].

A fundamental property of electrolytes is electrostatic screening [31,32]. Without screening, the internal energy would diverge in the thermodynamic limit. However, electroneutrality ensures that the Coulomb potential is effectively short-range, as we will see later. This ensures the applicability of statistical mechanics concepts. For a comprehensive review of screening and convergence conditions for Coulomb gases, see [33].

Strong and weak electrolytes Strong electrolytes are substances that completely ionize in solution, i.e., break down into their constituent ions. Examples of strong electrolytes include sodium chloride (NaCl), potassium hydroxide (KOH), and hydrochloric acid (HCl). When these substances dissolve in water, they dissociate into their individual ions, which can conduct electricity through the solution. Strong electrolytes are usually good conductors of electricity because most of the ions are free and can therefore participate in the

transport of charge. Weak electrolytes are substances that are only partially ionized in solution. This means that only a small fraction of the substance dissociates into ions, while the rest remains in pairs (or small aggregates) that have a neutral charge. This fact results in a lower conductivity compared to strong electrolytes. Examples of weak electrolytes are acetic acid (CH_3COOH) and ammonia (NH_3).

The strength of an electrolyte can also be quantified by its dissociation constant (K_d). Strong electrolytes have high K_d values, indicating complete dissociation in solution, while weak electrolytes have low K_d values, indicating partial dissociation.

2nd Wien effect Specific to weak electrolytes is a phenomenon known as the Second Wien Effect. This effect refers to an increase in the electrical conductivity of weak electrolyte solutions under the influence of a high electric field. Under normal conditions, weak electrolytes are only partially ionized, resulting in a limited number of ions in the solution.

Microscopically, although the bulk of the salt is dissolved, in weak electrolytes the negative and positive particles (anions and cations) form pairs (called Bjerrum pairs) that do not participate in the conduction of electricity at vanishing small external fields. However, a high electric field can break these bonds (induce an increase in the degree of ionization), thereby increasing the concentration of ions and, consequently, the conductivity of the solution. This phenomenon was also discussed by Onsager in [34]. We continue by describing theories for the thermodynamics of electrolytes, starting with static treatment of the system and later discussing the dynamics.

1.2 Electrostatics of ionic solutions

1.2.1 Poisson-Boltzmann Theory

The Poisson-Boltzmann (PB) theory is a widely used theoretical framework in the fields of physics, chemistry, and biology for studying the behavior of charged particles in solution. The theory is based on the assumption that a dilute gas of point-like ions is dispersed in a continuous dielectric medium, and that the ions interact solely through Coulombic interactions. For a modern review and discussion see [35, 36].

The central equation of the PB theory is the PB equation, which describes the electrostatic potential and charge distribution in a solution of charged particles at thermal equilibrium. This equation is obtained by combining the Poisson equation, which describes the electrostatic potential due to charges, with the Boltzmann distribution, which describes the distribution of charged particles in a solution. The resulting equation takes into account the electrostatic interactions between charged particles and the effect of the solvent on their distribution. It is possible to derive the PB equation starting from a field theory and to obtain the PB equation as a first-order term in a systematic expansion [37–39]. Here we use a simpler and more heuristic approach.

Starting from the Poisson equation:

$$\nabla^2 \phi(\mathbf{x}) = -\frac{1}{\varepsilon} Q_e(\mathbf{x}), \quad (1.1)$$

where $\phi(\mathbf{x})$ is the electrostatic potential, Q_e is the total local electric charge density, and ε is the permittivity of the medium. The total charge density is the sum of all ionic charge densities $Q_e = \sum_{\alpha} z_{\alpha} q \rho_{\alpha}$, where ρ_{α} and z_{α} are the bulk number density and the valency of the species α . q is the elementary charge. The ion density distribution in the solution can be described by Boltzmann statistics, namely for each ion species density we find:

$$\rho_{\alpha}(\mathbf{x}) = \bar{\rho}_{\alpha} \exp\left(-\frac{q z_{\alpha} \phi(\mathbf{x})}{T}\right), \quad (1.2)$$

where $\bar{\rho}_{\alpha}$ is the average ion concentration in the bulk and T is the thermal energy (throughout this manuscript, the Boltzmann constant is absorbed in the definition of T). Substituting the Boltzmann statistics into the Poisson equations gives the Poisson-Boltzmann equation:

$$\nabla^2 \phi(\mathbf{x}) = -\frac{1}{\varepsilon} \sum_{\alpha} q z_{\alpha} \bar{\rho}_{\alpha} \exp\left(-\frac{1}{T} z_{\alpha} q \phi(\mathbf{x})\right). \quad (1.3)$$

The Poisson-Boltzmann equation is a nonlinear partial differential equation that can be solved numerically and in certain cases analytically to obtain the electrostatic potential and charge distribution in a solution of charged particles [40, 41]. The solution provides information on a wide range of properties, including the binding affinity of molecules, the stability of colloidal suspensions, and the ionization behavior of proteins. One of the major strengths of the Poisson-Boltzmann theory is its ability to handle charged systems with complex geometries, such as proteins and nucleic acids. The theory has been used extensively to study electrostatic interactions in biological systems, including the electrostatic contribution to protein-protein and protein-DNA interactions.

It should be noted that PB theory is a mean-field theory that considers only thermal averages and ignores fluctuations around the mean and any inter-ionic correlations. Nevertheless, it remains an invaluable tool for understanding the electrostatic properties of charged systems in solution.

1.2.2 Debye-Hückel theory and the Debye length

The Debye-Hückel (DH) approximation is a simplification of the PB equation. At low ion concentrations, the DH approximation assumes that the electrostatic energy is small compared to the thermal energy, leading to a linearization of the PB equation. More precisely, when the limit $\frac{1}{T} q \phi \ll 1$ holds. This approximation predicts the behavior of electrolyte solutions in terms of the Debye length, which characterizes the length scale over which electrostatic interactions are screened by the ionic atmosphere. The Debye-Hückel approximation is widely used in electrochemistry to calculate the activity coefficients of electrolyte solutions, but it is limited to dilute solutions and cannot accurately predict the

behavior of concentrated electrolytes or solutions with strong ionic correlations. The zero-order term vanishes because the solution is electrically neutral on average (so $\sum_{\alpha} \bar{\rho}_{\alpha} z_{\alpha} = 0$), leaving only the first-order term. The result has the form of the Helmholtz equation:

$$\nabla^2 \phi(\mathbf{x}) = \frac{1}{\lambda_D^2} \phi(\mathbf{x}), \quad (1.4)$$

where λ_D is the Debye length, which is given by:

$$\lambda_D = \left(\frac{\epsilon T}{\sum_{\alpha} z_{\alpha}^2 q^2 \bar{\rho}_{\alpha}} \right)^{1/2}. \quad (1.5)$$

The Debye length represents the distance over which charged particles can interact by electrostatic forces. It is proportional to the square root of the inverse of the ionic strength, and thus becomes smaller as the concentration of ions increases. This treatment gives a simple description of the many-body interactions between ions. The solutions to Eq. (1.4) have a screened Coulomb (or Yukawa) form and are thus exponentially screened beyond λ_D . This shows that despite the long-range nature of the electrostatic interactions, at equilibrium, an electrolyte solution is effectively short-range interacting because the electric potential mediating the interactions is screened in the presence of opposite charges. DH theory provides a convenient starting point for theoretical investigations of charged solutions under a variety of conditions.

1.3 Dynamics of electrolytes

So far we have focused on the equilibrium properties of ionic solutions. However, there are interesting phenomena that occur out of thermodynamic equilibrium. For example, an applied electric field can induce electrolyte flow in a capillary (electroosmosis) [42–45], and a salt concentration gradient in a capillary causes water flow (diffusio-osmosis) [46] and electric currents (osmotic current) [47]. In colloidal suspensions, the transport of charged colloids can be achieved by applying an external electric field (electrophoresis) [48–50]. An important example of a dynamical ionic system is a battery, where two electrodes made of different materials are placed in an electrolyte solution. When an external circuit connects the two electrodes, the charge of the electrons flowing in the external circuit is balanced by the ionic currents inside the battery. As the battery discharges, it converts the initial chemical energy into electrical energy. In a rechargeable battery, the opposite occurs when electrical energy is converted to chemical energy during the charging cycle.

1.3.1 Poisson-Nernst-Planck equation

A common theoretical framework for studying the dynamics of ionic systems is the Poisson-Nernst-Planck equation. This equation, which takes into account dynamics can be derived from the Poisson-Boltzmann electrochemical potential, (see ref. [40, 51] for the derivation

of the PB potential):

$$\mu_\alpha = T \ln(\rho_\alpha a^3) + qz_\alpha \phi, \quad (1.6)$$

where μ_α is the chemical potential of the species α , and a the ion's length scale. Within the linear response, the difference between the mean ionic velocities, \mathbf{v}_α and the solvent velocity, \mathbf{u} , is given by the chemical-potential gradient:

$$\mathbf{v}_\alpha - \mathbf{u} = -\kappa_\alpha \nabla \mu_\alpha, \quad (1.7)$$

where κ_α is the mobility of the ionic species in the solution. The flow field of the solution \mathbf{u} is governed by the the Navier-Stokes equation and in principle is coupled to the ion density fields. For the purposes of the following discussion, it will go beyond the scope to elaborate on this. See Sec. 1.4 for further details. Furthermore, the ion concentrations satisfy a continuity equation:

$$\dot{\rho}_\alpha = -\nabla \cdot (\rho_\alpha \mathbf{v}_\alpha). \quad (1.8)$$

Combining Eqs. (1.8) and (1.7) we get:

$$\dot{\rho}_\alpha = -\nabla \cdot [\rho_\alpha \mathbf{u} - \kappa_\alpha T \nabla \rho_\alpha + \kappa_\alpha q z_\alpha \rho_\alpha \nabla \phi], \quad (1.9)$$

with the Poisson equation (1.1) which relates the ionic densities to the electric potential. We can express the gradient of the electric potential ϕ as the sum of an interaction term and an external field term $\nabla \phi = \mathbf{E} - \nabla \sum_\beta V_{\alpha\beta} * \rho_\beta$ where $V_{\alpha\beta}$ is the interaction potential between the ionic species α and β , $*$ symbolizes a spatial convolution and \mathbf{E} is the external field. Finally we get the Poisson-Nernst-Planck equation:

$$\dot{\rho}_\alpha = -\nabla \cdot \mathbf{j}_\alpha \quad (1.10)$$

$$\mathbf{j}_\alpha = \rho_\alpha \mathbf{u} - \kappa_\alpha T \nabla \rho_\alpha + \kappa_\alpha q z_\alpha \rho_\alpha \left(\mathbf{E} - \nabla \sum_\beta V_{\alpha\beta} * \rho_\beta \right). \quad (1.11)$$

The ionic flux \mathbf{j}_α includes three terms. They are, respectively, advection, diffusion, and drift due to the (external and interactional) electric field. Since the Poisson-Nernst-Planck equation is derived from the PB electrochemical potential, it inherits its limitations. In particular, ionic correlations are neglected. This is justified for dilute solutions, but not for concentrated ones.

1.3.2 Conductivity of electrolytes

Ionic conductivity is a fundamental dynamical property of ionic solutions and is defined as the total averaged electric current divided by the external field, $\sigma_0 = \frac{\langle J \rangle}{E_0}$. The interaction of ions in solution through electrostatic forces affects the behavior of the ions and the ability of the solution to conduct an electric current. The flow of ions in solution is influenced not only by electrostatic interactions, but also by hydrodynamic interactions arising from the motion of ions through the solvent, which in turn affects conductivity [25].

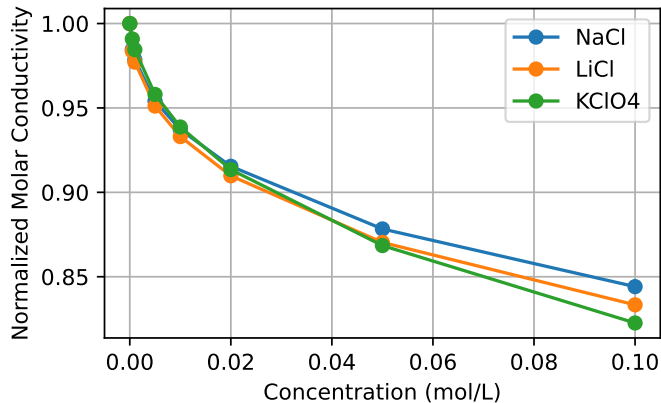


Figure 1.1: The molar conductivity of different ionic mixtures in aqueous solution, to compare with Eq. (1.14). One can see that the Nernst formula would predict a constant as we divided by the concentration to get the molar conductivity. Data points were taken from [52]. measurements were done in the linear response regime and at constant temperature ($298K$).

The conductivity of an ionic solution depends on several factors, including the ion concentration, the size and charge of the ions, the temperature of the solution, and the presence of other solutes or impurities. We can calculate the bulk conductivity of an electrolyte using the PNP equation. The total electric current reads:

$$\langle \mathbf{J} \rangle = q \sum \mathbf{j}_\alpha z_\alpha. \quad (1.12)$$

As we compute the current in the bulk, there are no gradients and the ionic densities are constants, therefore we find:

$$\langle \mathbf{J} \rangle = \sum_\alpha q z_\alpha \rho_\alpha \mathbf{u} + \sum_\alpha q^2 z_\alpha^2 \kappa_\alpha \rho_\alpha \mathbf{E}. \quad (1.13)$$

For an electroneutral system (or alternatively setting $\mathbf{u} = 0$) we find that the total charge current reduces to:

$$\sigma_0 = \sum_\alpha z_\alpha^2 q^2 \kappa_\alpha \bar{\rho}_\alpha. \quad (1.14)$$

This formula, which is known as the Nernst conductivity, is valid in the infinite dilution limit, where particle interactions are negligible. This result does not agree with experimental measurements, as can be seen qualitatively in Fig. (1.1), even at very low concentrations and external fields. This behavior was first seen by Kohlrausch [17] and it well demonstrates the limitations of the mean-field approach and motivates the integration of the particle-particle correlation into the theory. One framework that allows for the inclusion of correlations is the so-called Stochastic density functional theory.

1.3.3 Stochastic density functional theory

The main focus of our analytical investigations in the following will be on the overdamped dynamics of electrolyte systems, where inertial effects are negligible. The most common models of stochastic dynamics make use of the Langevin formalism, which was originally developed to study the motion of Brownian particles and later extended to the dynamics of interacting particles and fields. Currently, approaches based on coarse-grained Langevin dynamics have become a standard tool, widely used in the study of collective phenomena in active and non-equilibrium systems.

A sophisticated approach to studying the dynamics of ionic solutions, including ionic correlations, is stochastic density functional theory (SDFT), often referred to as the Dean-Kawasaki equation [53–57]. SDFT provides an exact equation obeyed by the density function (or concentration field) for a system of Langevin processes interacting via a pairwise potential.

Dean–Kawasaki equation

This part follows the steps taken in the original derivation [53]. Consider N particles interacting via the pairwise potential $V(r)$. The particles are subject to an external velocity field denoted by $\mathbf{U}(x, t)$. Each particle obeys the Langevin dynamics:

$$\frac{d\mathbf{X}_i(t)}{dt} = \mathbf{U}(\mathbf{X}_i, t) - \kappa \sum_{j=1}^N \nabla V(\mathbf{X}_i(t) - \mathbf{X}_j(t)) + \sqrt{\kappa T} \boldsymbol{\xi}_i(t). \quad (1.15)$$

We use the assumption $\nabla V(0) = 0$ to include the term i in the sum. $\boldsymbol{\xi}_i(t)$ is a vectorial noise that satisfies the statistics:

$$\langle \boldsymbol{\xi}_i(t) \boldsymbol{\xi}_j(t') \rangle = 2\delta_{ij} \delta(t - t'). \quad (1.16)$$

We define the density field of a single particle and the total density field by:

$$\rho_i(\mathbf{x}, t) = \delta(\mathbf{x} - \mathbf{X}_i(t)) \quad ; \quad \rho(\mathbf{x}, t) = \sum_{i=1}^N \delta(\mathbf{x} - \mathbf{X}_i(t)). \quad (1.17)$$

For any single-particle function $f(\mathbf{X}_i(t))$, we can write:

$$f(\mathbf{X}_i(t)) = \int d\mathbf{x} \rho_i(\mathbf{x}, t) f(\mathbf{x}, t). \quad (1.18)$$

Since $\mathbf{X}_i(t)$ is a stochastic function, analysis of its derivatives, as well as of functions of $\mathbf{X}_i(t)$, should be done according to specific calculus rules (which are linked to specific discretization schemes). In this work we use Itô calculus. Using Itô's lemma [58], the differential of a test function g of the stochastic process is $g(\mathbf{X}_i(t))$ is:

$$\frac{d}{dt} g(\mathbf{X}_i(t)) = [\nabla g](\mathbf{X}_i) \cdot \frac{d\mathbf{X}_i(t)}{dt} + \kappa T [\nabla^2 g](\mathbf{X}_i). \quad (1.19)$$

Using Eq. (1.18) with Eq. (1.19) we get:

$$\frac{d}{dt}g(\mathbf{X}_i(t)) = \int d\mathbf{x}\rho_i(\mathbf{x}, t) \left([\nabla g](\mathbf{x}) \cdot \frac{d\mathbf{x}}{dt} + \kappa T[\nabla^2 g](\mathbf{x}) \right), \quad (1.20)$$

where $\frac{d\mathbf{x}}{dt} = \mathbf{U}(\mathbf{x}, t) - \kappa \sum_j \nabla V(\mathbf{x} - \mathbf{X}_j) + \sqrt{\kappa T} \boldsymbol{\xi}_i$. We can now use integration by parts to find:

$$\frac{d}{dt}g(\mathbf{X}_i(t)) = \int d\mathbf{x}g(\mathbf{x}) \left[\nabla \cdot \left(-\rho_i(\mathbf{x}, t) \frac{d\mathbf{x}}{dt} \right) + \kappa T \nabla^2 \rho_i(\mathbf{x}, t) \right]. \quad (1.21)$$

On the other hand, the time derivative of $g(\mathbf{X}_i(t))$ is simply $\frac{d}{dt}g(\mathbf{X}_i(t)) = \int d\mathbf{x} \frac{d\rho_i(\mathbf{x}, t)}{dt} g(\mathbf{x}, t)$. By equating the two expressions for $\frac{d}{dt}g(\mathbf{X}_i(t))$ we find the an equation for the evolution of ρ_i :

$$\frac{d\rho_i(\mathbf{x}, t)}{dt} = -\nabla \cdot \left[\rho_i(\mathbf{x}, t) \left(\mathbf{U}(\mathbf{x}, t) - \kappa \sum_j \nabla V(\mathbf{x} - \mathbf{X}_j) + \sqrt{\kappa T} \boldsymbol{\xi}_i \right) \right] + \kappa T \nabla^2 \rho_i(\mathbf{x}, t). \quad (1.22)$$

Now summing the equations for every i we find:

$$\frac{d\rho(\mathbf{x}, t)}{dt} = -\nabla \cdot \left[\rho(\mathbf{x}, t) \left(\mathbf{U}(\mathbf{x}, t) - \kappa \int d\mathbf{x}' \rho(\mathbf{x}', t) \nabla V(\mathbf{x} - \mathbf{x}') \right) \right] + \kappa T \nabla^2 \rho(\mathbf{x}, t) - \Xi(\mathbf{x}, t), \quad (1.23)$$

with a global noise term that respect the following correlation function:

$$\langle \Xi(\mathbf{x}, t) \Xi(\mathbf{x}', t') \rangle = 2\kappa T \delta(t - t') \sum_i \nabla \cdot \nabla' \rho_i(\mathbf{x}, t) \rho_i(\mathbf{x}', t'). \quad (1.24)$$

Note that we have used Eq. (1.18) to rewrite the interaction term. Recalling that the ρ_j are Dirac delta functions, the expression simplifies using a property of these functions: $\rho_i(\mathbf{x}, t) \rho_i(\mathbf{x}', t) = \delta(\mathbf{x} - \mathbf{x}') \rho_i(\mathbf{x}, t) = \delta(\mathbf{x} - \mathbf{x}') \rho_i(\mathbf{x}', t)$. Applying that, we find that the noise correlation function can be written with in terms of the total density ρ :

$$\langle \Xi(\mathbf{x}, t) \Xi(\mathbf{x}', t') \rangle = -2\kappa T \delta(t - t') \nabla \cdot (\rho(\mathbf{x}, t) \nabla \delta(\mathbf{x} - \mathbf{x}')). \quad (1.25)$$

From the structure of this correlation function we see that Ξ is statistically equivalent to a new noise term $\hat{\Xi}$:

$$\hat{\Xi}(\mathbf{x}, t) = \nabla \cdot \left(\sqrt{\kappa T \rho(\mathbf{x}, t)} \boldsymbol{\zeta}(\mathbf{x}, t) \right), \quad (1.26)$$

where $\boldsymbol{\zeta}$ being is an Gaussian noise field with the following correlation function:

$$\langle \boldsymbol{\zeta}(\mathbf{x}, t) \boldsymbol{\zeta}(\mathbf{x}', t') \rangle = 2\delta(\mathbf{x} - \mathbf{x}') \delta(t - t'). \quad (1.27)$$

We replace Ξ by $\hat{\Xi}$ so that our equation can be written as:

$$\begin{aligned} \frac{d\rho(\mathbf{x}, t)}{dt} = \nabla \cdot \left[T\kappa \nabla \rho(\mathbf{x}, t) - \mathbf{U}(\mathbf{x}, t) \rho(\mathbf{x}, t) + \kappa \rho(\mathbf{x}, t) \int d\mathbf{x}' \rho(\mathbf{x}', t) \nabla V(\mathbf{x} - \mathbf{x}') \right] \\ + \nabla \cdot \left[\sqrt{\kappa T \rho(\mathbf{x}, t)} \boldsymbol{\zeta}(\mathbf{x}, t) \right]. \end{aligned} \quad (1.28)$$

This equation, known as the Dean-Kawasaki equation, has the same structure as the PNP equation, but includes a multiplicative noise term. It is important to note that the continuous fields in the SDFT equation are not averaged quantities as in the PNP equation, but stochastic fluctuating fields. The PNP equation is recovered from the Dean equation by taking the thermal average and neglecting correlations. In the following chapter, SDFT is used to derive the conductivity of ionic solutions at high ionic concentrations, and the inclusion of ionic correlations turns out to be essential. By including correlations, the advection term does not go to zero in an electroneutral system, and in the following section we discuss how to address it.

1.4 Hydrodynamic interaction

Hydrodynamic interactions are an important component of fluid dynamics, describing the reciprocal influence of particles within a fluid medium. As particles move through the medium, they displace and drag the surrounding fluid, changing the flow field. This flow, in turn, advects adjacent particles. Due to the dependence of this interaction on the distances between the particles and their velocities, it cannot be addressed by an interaction potential, and consequently the analysis must be done at the level of forces.

A useful simplification in the study of hydrodynamic interaction is the Stokes flow regime, which is a special case of fluid flow characterized by a low Reynolds number. The Stokes flow regime is often used to describe the behavior of small particles, such as bacteria or colloidal particles, which move slowly relative to the fluid around them [59]. In this regime, viscous forces dominate while inertial forces are negligible. In electrolytes, the hydrodynamic properties of the solvent can be characterized by its dynamic viscosity and density, and the small ionic diameter typically results in a very low Reynolds number, meaning that hydrodynamic effects in electrolyte systems are adequately described by incompressible laminar flow [30].

In the Stokes flow regime, the inertial terms in the Navier-Stokes equations governing fluid motion can be ignored. This approximation leads to the Stokes equations:

$$\nabla p - \eta \nabla^2 \mathbf{u} = \mathbf{f} \quad ; \quad \nabla \cdot \mathbf{u} = 0, \quad (1.29)$$

where p is the pressure, η is the dynamic viscosity of the fluid, \mathbf{u} is the velocity field, and \mathbf{f} is the external force. The first equation describes force balance, while the second equation enforces the incompressibility of the fluid.

1.4.1 Stokeslet

The Stokeslet, or the fundamental solution to the Stokes equations, represents the flow field induced by a point force applied at the origin within a viscous fluid. It can be used to describe the hydrodynamic interactions between particles in a Stokes flow. This solution

can be written as:

$$\mathbf{u}(\mathbf{x}) = \mathcal{O}(\mathbf{x})\mathbf{F}, \quad (1.30)$$

where \mathbf{F} is the point force, and $\mathcal{O}(\mathbf{x})$ is the Green's function for the Stokes equations, the Oseen tensor:

$$\mathcal{O}_{ij}(\mathbf{x}) = \frac{1}{8\pi\eta} \left(\frac{\delta_{ij}}{x} + \frac{x_i x_j}{x^3} \right). \quad (1.31)$$

For multi-particle systems, where each particle's motion is affected by every other particle via the fluid medium, the total flow field is the superposition of the individual Stokeslets solutions:

$$\mathbf{u}(\mathbf{x}) = \int \mathcal{O}(\mathbf{x} - \mathbf{x}')\mathbf{f}(\mathbf{x}')d\mathbf{x}'. \quad (1.32)$$

This known result will later be integrated into the SDFT, allowing us to compute the hydrodynamic correction to the conductivity of strong electrolytes.

1.5 Recent developments

The study of the conductivity of electrolytes has recently been revived. First, Stochastic density functional theory (SDFT) was used to calculate the ionic correlations in the absence of hydrodynamic interactions, giving access to the electrostatic correction of the conductivity [53,60]. This study recovers the results derived by Onsager for one of the two correction terms for the steady state conductivity of electrolytes at finite external field. The correction term it computes is usually referred to as the relaxation or electrostatic correction, and is related to the electrostatic interactions between the particles. Then, SDFT has been coupled with fluctuating hydrodynamics, providing a stochastic field theory for the ionic densities and the flow, allowing to derive the electrostatic correction together with the hydrodynamic one [61,62]. As we will see later on, at first order in the species density fluctuations, the hydrodynamic correction does not affect the particle particle correlation but still affects the total current in the system.

These more systematic approaches allowed further progress, such as taking into account the finite size of the ions using a slight modification of the interaction kernel, leading to quantitative predictions for the conductivity corrections up to larger densities [63,64]. More specifically, these studies have used particle particle interaction that follows the standard electrostatic interaction but is truncated for distances smaller than a parameter a , which represent the particle size. In this region, the potential is set to zero to account qualitatively for the short range repulsion between any pair of particles. Although the physical picture arising from this modification of the interaction potential is quite different from the one we would like to model, it seems to give a better averaged description of the interaction compared to the standard electrostatic one. It prevents the collapse of opposite charges towards one another, at the price of allowing same charges to bind with some finite energy barrier [65]. Other studies have used SDFT to reveal long-range forces between objects immersed in a driven electrolyte [66]. These forces were shown to be induced by long-

range fluctuations. The study used linearized SDFT and focused on the macroscopic limit, namely beyond the Debye length scale and time scale $t_D = \lambda_D^2/(\kappa T)$. In this limit the dynamics of the mass density simplifies to a noisy non-isotropic diffusion equation. This equation can be solved in certain confined geometries and its solutions can be related to the charge distribution and thus to the electric potential. The relationship between the stresses at the boundaries and the electric potential is established by using the Maxwell stress tensor.

In parallel, the effect of the correlations on the conductivity has been studied in weak electrolytes through numerical simulation of a lattice Coulomb gas [67]. This work provided a detailed characterization of the second Wien effect. Another group studied strong electrolyte systems using molecular dynamics [68,69], with an implicit or explicit solvent. That is, they simulated the ions in the bulk as underdamped Langevin processes, moving under the influence of an adjusted permittivity and drag force (implicit), or by adding the water molecules to the simulation, which in turn changes the electric field and drag on the ions in space (explicit). They find that explicit solvent effects act to suppress nonlinear responses, resulting in weakly field-dependent conductivity over the range of physically realizable field strengths.

Similar methods have been employed to study the correlation and effective mobility of a driven system with short ranged interaction [70], finding the formation of lanes along their direction of motion. This behavior is explained by the correlation functions which decay algebraically along the direction of motion. These calculations were carried out using the SDFT formalism.

The above mentioned work dealt with the non-equilibrium steady state (NESS) of a driven electrolyte. Under a time-dependent driving, new interesting effects appear, such as a long-ranged repulsion between oppositely charged surfaces under a periodic driving [71], or synapse-like memory effects in strongly confined electrolytes [72,73].

To date, there are few examples where the field theoretic machinery described above has been used to study transient effects in electrolytes. One is the calculation of the transient fluctuations induced forces between two objects immersed in a driven electrolyte upon a sudden field change [74]; however, the hydrodynamic interactions were neglected and the calculation of transient correlations was limited to distances much larger than the Debye length. Other related examples are the calculations of the relaxation of the Casimir force between two polarizable slabs or two conducting plates [75,76], but in these cases the transition takes place between two equilibrium states.

Chapter 2

Temporal response of the conductivity

This chapter is mostly an extraction from the paper [9]

In this chapter, we use SDFT with hydrodynamic interactions [60,62] to study the evolution of the electric current in a bulk electrolyte when the external field is suddenly switched on or off. First, we show that the correlations do not follow the same path when the system goes from equilibrium to NESS, or from NESS to equilibrium. Second, we turn to the current, and in particular to the electrostatic and hydrodynamic corrections. From NESS to equilibrium, the hydrodynamic correction is absent and we find that the electrostatic correction decays exponentially. On the contrary, from equilibrium to NESS, we unveil an algebraic decay of both corrections. At linear order in the field, the corrections decay exponentially, showing that the algebraic decay is a non-linear effect. Finally, we study the long range behavior of the correlation in real space, finding that a non isotropic diffusion governs the dynamics.

This chapter is organized as follows. The model is introduced in Sec. 2.1. In Sec. 2.2 we obtain a closed equation for the density fields of the ions, express the electric current as a function of the correlations of the density fields, and derive and solve the equation for the correlations in the transient regime, assuming Gaussian density fields. We compute and analyse the corrections from NESS to equilibrium in Sec. 2.5, and from equilibrium to NESS in Sec. 2.6. In the next chapter. (3), we analyse the long range behavior of the correlations.

2.1 Model

We consider a system of charged Brownian particles of different species in a three dimensional homogeneous solution, subjected to a uniform external electric field with a time dependent amplitude $\mathbf{E}(t) = E(t)\hat{\mathbf{e}}_x$, where $\hat{\mathbf{e}}_x$ is the unit vector along the x -axis. The particles interact via the electrostatic potential and are advected by the flow in the solution, which is generated by the forces transmitted by the particles on the solvent. We denote $\bar{\rho}_\alpha$ the average density of the particles of the species α , κ_α their mobility and qz_α their charge, with q being the elementary charge. We assume that the system is electroneutral:

$$\sum_{\alpha} z_{\alpha} \bar{\rho}_{\alpha} = 0.$$

We describe the evolution of the density field $\rho_{\alpha}(\mathbf{x}, t)$ of the species α using Stochastic Density Functional Theory [53, 60] with hydrodynamic interactions [61, 62]:

$$\dot{\rho}_{\alpha} = -\nabla \cdot \mathbf{j}_{\alpha}, \quad (2.1)$$

$$\mathbf{j}_{\alpha} = \mathbf{u} \rho_{\alpha} - T \kappa_{\alpha} \nabla \rho_{\alpha} + \kappa_{\alpha} \rho_{\alpha} \mathbf{f}_{\alpha} + \sqrt{\kappa_{\alpha} T \rho_{\alpha}} \boldsymbol{\zeta}_{\alpha}, \quad (2.2)$$

where $\mathbf{u}(\mathbf{x}, t)$ is the velocity field of the solution, T is the temperature (we set the Boltzmann constant to $k_B = 1$) and $\mathbf{f}_{\alpha}(\mathbf{x}, t)$ is the force acting on the particles of the species α . The noise term $\boldsymbol{\zeta}(\mathbf{x}, t)$ is a Gaussian white noise with the correlation:

$$\langle \boldsymbol{\zeta}_{\alpha}(\mathbf{x}, t) \boldsymbol{\zeta}_{\beta}(\mathbf{x}', t') \rangle = 2 \delta_{\alpha\beta} \delta(\mathbf{x} - \mathbf{x}') \delta(t - t'). \quad (2.3)$$

We use the Itô convention for the multiplicative noise in Eq. (2.2) and throughout the manuscript [53, 58].

The force on the particles of the species α is the sum of the force exerted by the external field and the force due to pair interactions:

$$\mathbf{f}_{\alpha} = z_{\alpha} q \mathbf{E} - \sum_{\beta} \nabla V_{\alpha\beta} * \rho_{\beta}, \quad (2.4)$$

where $V_{\alpha\beta}(\mathbf{x}) = q^2 z_{\alpha} z_{\beta} / (4\pi\epsilon r)$ is the electrostatic interaction, with $r = |\mathbf{x}|$, ϵ the dielectric permittivity of the solvent, and $*$ the convolution operator.

We assume that the fluid velocity field $\mathbf{u}(\mathbf{x}, t)$ satisfies the fluctuating Stokes equation for incompressible fluids [77] (Sec. 3.2):

$$\nabla \cdot \mathbf{u} = 0 \quad (2.5)$$

$$-\eta \nabla^2 \mathbf{u} - \nabla p = \sum_{\alpha} \rho_{\alpha} \mathbf{f}_{\alpha} + \sqrt{\eta T} \nabla \cdot (\boldsymbol{\nu} + \boldsymbol{\nu}^T), \quad (2.6)$$

where $\boldsymbol{\nu}(\mathbf{x}, t)$ is a Gaussian noise tensor field with correlation function:

$$\langle \nu_{ij}(\mathbf{x}, t) \nu_{kl}(\mathbf{x}', t') \rangle = \delta_{ik} \delta_{jl} \delta(\mathbf{x} - \mathbf{x}') \delta(t - t'). \quad (2.7)$$

We compute the total average electric current $\mathbf{J}(t)$:

$$\mathbf{J} = q \sum_{\alpha} z_{\alpha} \langle \mathbf{j}_{\alpha} \rangle = J \hat{\mathbf{e}}_x, \quad (2.8)$$

and then discuss the correction to the current without interactions, $\sigma_0 \mathbf{E}$, where $\sigma_0 = q^2 \sum_{\alpha} z_{\alpha}^2 \kappa_{\alpha} \bar{\rho}_{\alpha}$ is the bare conductivity of the solution. In particular, we are interested in the evolution of the current $J(t)$ when the electric field is suddenly switched on ($E(t) = E_0 H(t)$, where $H(t)$ is the Heaviside function), or off ($E(t) = E_0 H(-t)$). In the first case, the

system goes from equilibrium with $E = 0$ to a non-equilibrium steady state (NESS) with $E = E_0$; in the second case, the system relaxes from a NESS to equilibrium.

2.2 Correlations and electric current

2.2.1 Closed equations for the density fields

We can integrate the fluid degrees of freedom \mathbf{u} to obtain a closed equation for the densities ρ_α . The solution to Eqs. (2.5, 2.6) is given by the convolution of the force density (the right hand side of Eq. (2.6)) with the Oseen tensor, $\mathcal{O}_{ij}(\mathbf{x}) = \frac{1}{8\pi\eta} \left(\frac{\delta_{ij}}{r} + \frac{x_i x_j}{r^3} \right)$ [78] (Chap. 2). Inserting this result in the expression for the density current, Eq. (2.2), we get:

$$\mathbf{j}_\alpha = -\kappa_\alpha T \nabla \rho_\alpha + \kappa_\alpha \rho_\alpha \mathbf{f}_\alpha + \rho_\alpha \sum_\beta \mathcal{O} * [\rho_\beta \mathbf{f}_\beta] + \sqrt{\kappa_\alpha T \rho_\alpha} \boldsymbol{\zeta}_\alpha + \sqrt{\eta T \rho_\alpha} \mathbf{w}, \quad (2.9)$$

where we have introduced the Gaussian noise vector field $\mathbf{w}(\mathbf{x}, t)$ with correlation:

$$\langle w_i(\mathbf{x}, t) w_j(\mathbf{x}', t') \rangle = 2\mathcal{O}_{ij}(\mathbf{x} - \mathbf{x}') \delta(t - t'). \quad (2.10)$$

Equations (2.1, 2.3, 2.9, 2.10) form a closed set of equations for the densities.

Our procedure is however not completely correct: when a force is applied on a particle, it gives rise to a flow that is given by the Oseen tensor. However, this flow diverges at the location of the particle, giving the particle an infinite velocity [79]. Moreover, the motion of the particle resulting from the application of the force is already taken into account by the mobility of the particle. Hence, when computing the flow advecting a given particle, one should take care to omit the flow created by the forces acting on this particle. There is no simple way to do it in our field theory, but this flaw is easily corrected when the electric current is expressed with the correlations.

2.2.2 Average electric current from correlations

Using the expression (2.9) in the average electric current (Eq. (2.8)) leads to:

$$\mathbf{J} = q \sum_\alpha z_\alpha \left\langle \kappa_\alpha \rho_\alpha \mathbf{f}_\alpha + \rho_\alpha \sum_\beta \mathcal{O} * [\rho_\beta \mathbf{f}_\beta] \right\rangle. \quad (2.11)$$

Note that the noise terms cancel as they are uncorrelated to the density fields and the gradient term cancels as we assume spatial invariance.

We now express the average electric current as a function of the correlations of the density fields. We introduce the density fluctuations $n_\alpha(\mathbf{x}, t)$:

$$\rho_\alpha(\mathbf{x}, t) = \bar{\rho}_\alpha + n_\alpha(\mathbf{x}, t), \quad (2.12)$$

and the correlation:

$$C_{\alpha\beta}(\mathbf{x} - \mathbf{x}', t) = \langle n_{\alpha}(\mathbf{x}, t) n_{\beta}(\mathbf{x}', t) \rangle = \mathcal{C}_{\alpha\beta}(\mathbf{x} - \mathbf{x}', t) + \bar{\rho}_{\alpha} \delta_{\alpha\beta} \delta(\mathbf{x} - \mathbf{x}'), \quad (2.13)$$

where \mathcal{C} is the pair correlation function, which does not contain the self correlation.

Using electroneutrality, the average electric current (Eq. (2.11)) can be expressed with the density fluctuations:

$$\begin{aligned} \mathbf{J} = \sigma_0 \mathbf{E} - \sum_{\alpha, \beta} q z_{\alpha} \kappa_{\alpha} \langle n_{\alpha} \nabla V_{\alpha\beta} * n_{\beta} \rangle + \sum_{\alpha, \beta} q^2 z_{\alpha} z_{\beta} \langle n_{\alpha} \mathcal{O} * n_{\beta} \rangle \mathbf{E} \\ - \sum_{\alpha, \beta, \gamma} q z_{\alpha} \langle n_{\alpha} [\mathcal{O} * (n_{\beta} [\nabla V_{\beta\gamma} * n_{\gamma}])] \rangle. \end{aligned} \quad (2.14)$$

Writing the convolutions explicitly and using the correlation (Eq. (2.13)), we arrive at:

$$\begin{aligned} \mathbf{J} = \sigma_0 \mathbf{E} - \sum_{\alpha, \beta} q z_{\alpha} \kappa_{\alpha} \int \nabla V_{\alpha\beta}(\mathbf{x}) C_{\alpha\beta}(\mathbf{x}) d\mathbf{x} + \sum_{\alpha, \beta} q^2 z_{\alpha} z_{\beta} \int \mathcal{O}(\mathbf{x}) C_{\alpha\beta}(\mathbf{x}) d\mathbf{x} \mathbf{E} \\ - \sum_{\alpha, \beta, \gamma} q z_{\alpha} \int \mathcal{O}(\mathbf{x}) \nabla V_{\beta\gamma}(\mathbf{x}') C_{\alpha\beta\gamma}^{(3)}(\mathbf{x}, \mathbf{x}') d\mathbf{x} d\mathbf{x}', \end{aligned} \quad (2.15)$$

where we have introduced the three-point correlation $C_{\alpha\beta\gamma}^{(3)}(\mathbf{x} - \mathbf{x}', \mathbf{x}' - \mathbf{x}'') = \langle n_{\alpha}(\mathbf{x}) n_{\beta}(\mathbf{x}') n_{\gamma}(\mathbf{x}'') \rangle$.

The correction to the bare current $\sigma_0 \mathbf{E}$ is the sum of three contributions:

- The first involves the correlation and the electrostatic potential, we call it the *electrostatic correction* (it was originally called the relaxation correction). It represents the effect of the electric field of the cloud of counterions around a charged particle, which is deformed when an external field is applied.
- The second term involves the correlation, the Oseen tensor, and the external field, we call it the *hydrodynamic correction* (it was originally called the electrophoretic correction). It contains the effect of the flow created by the cloud of counterions under the action of the external field.
- The last term combines electrostatic and hydrodynamic effects: it contains the effect of the flow created by the counterions under the action of electrostatic interactions between the particles. As electrostatic and hydrodynamic interactions are involved, their interaction kernels are coupled to the three-point correlation $C^{(3)}$.

At this stage, we can make the correction mentioned in Sec. 2.2.1: remove the effect of the flow that is generated by a particle on this same particle. In the hydrodynamic correction, this is done by replacing the correlation $C_{\alpha\beta}(\mathbf{x})$ by the pair correlation $\mathcal{C}_{\alpha\beta}(\mathbf{x})$ (see Eq. (2.13)), which removes a term proportional to $\mathcal{O}(0)$. In the last term of Eq. (2.15), it is done by subtracting $\delta_{\alpha\beta} \delta(\mathbf{x}) C_{\beta\gamma}(\mathbf{x}')$ to $C_{\alpha\beta\gamma}^{(3)}(\mathbf{x}, \mathbf{x}')$. However, as we will compute the correlations in the Debye-Hückel limit where the odd correlations vanish, it is not

necessary to remove this term. Finally, note that replacing the correlation $C_{\alpha\beta}(\mathbf{x})$ by the pair correlation $\mathcal{C}_{\alpha\beta}(\mathbf{x})$ does not affect the electrostatic correction, allowing us to use the pair correlation in both corrections:

$$\begin{aligned} \mathbf{J} = \sigma_0 \mathbf{E} - \sum_{\alpha,\beta} qz_\alpha \kappa_\alpha \int \nabla V_{\alpha\beta}(\mathbf{x}) \mathcal{C}_{\alpha\beta}(\mathbf{x}) d\mathbf{x} + \sum_{\alpha,\beta} q^2 z_\alpha z_\beta \int \mathcal{O}(\mathbf{x}) \mathcal{C}_{\alpha\beta}(\mathbf{x}) d\mathbf{x} \mathbf{E} \\ - \sum_{\alpha,\beta,\gamma} qz_\alpha \int \mathcal{O}(\mathbf{x}) \nabla V_{\beta\gamma}(\mathbf{x}') C_{\alpha\beta\gamma}^{(3)}(\mathbf{x}, \mathbf{x}') d\mathbf{x} d\mathbf{x}'. \end{aligned} \quad (2.16)$$

Using the Parseval-Plancherel theorem and writing explicitly the time dependencies, we get:

$$\begin{aligned} \mathbf{J}(t) = \sigma_0 \mathbf{E}(t) + \sum_{\alpha,\beta} qz_\alpha \kappa_\alpha \int i\mathbf{k} \tilde{V}_{\alpha\beta}(\mathbf{k}) \tilde{\mathcal{C}}_{\alpha\beta}(\mathbf{k}, t) \frac{d\mathbf{k}}{(2\pi)^d} \\ + \sum_{\alpha,\beta} q^2 z_\alpha z_\beta \int \tilde{\mathcal{O}}(\mathbf{k}) \tilde{\mathcal{C}}_{\alpha\beta}(\mathbf{k}, t) \frac{d\mathbf{k}}{(2\pi)^d} \mathbf{E}(t) \\ + \sum_{\alpha,\beta,\gamma} qz_\alpha \int \tilde{\mathcal{O}}(\mathbf{k}) i\mathbf{k}' \tilde{V}_{\beta\gamma}(\mathbf{k}') \tilde{C}_{\alpha\beta\gamma}^{(3)}(\mathbf{k}, \mathbf{k}', t) \frac{d\mathbf{k} d\mathbf{k}'}{(2\pi)^{2d}}. \end{aligned} \quad (2.17)$$

We have used the fact that the Fourier transforms $\tilde{V}_{\alpha\beta}(\mathbf{k}) = \frac{q^2 z_\alpha z_\beta}{\epsilon k^2}$ and $\tilde{\mathcal{O}}_{ij}(\mathbf{k}) = \frac{1}{\eta k^2} (\delta_{ij} - \frac{k_i k_j}{k^2})$ are even: $\tilde{V}_{\alpha\beta}(\mathbf{k}) = \tilde{V}_{\alpha\beta}(-\mathbf{k})$ and $\tilde{\mathcal{O}}(\mathbf{k}) = \tilde{\mathcal{O}}(-\mathbf{k})$.

Now that we have expressed the correction to the bare current as a function of the correlations, we need to evaluate the correlations.

2.2.3 Correlations in the Debye-Hückel limit

The density correlations cannot be computed exactly. To evaluate them, we assume small density fluctuations $|n_\alpha| \ll \bar{\rho}_\alpha$ and take the Debye-Hückel limit, which amounts to linearize the deterministic terms in the current Eq. (2.9) and remove the fluctuations in front of the noise terms [60, 61]. Linearizing Eq. (2.9) and plugging it into Eq. (2.1), we get:

$$\dot{n}_\alpha = \kappa_\alpha T \nabla^2 n_\alpha - \kappa_\alpha q z_\alpha \mathbf{E} \cdot \nabla n_\alpha + \kappa_\alpha \bar{\rho}_\alpha \nabla^2 \left[\sum_\beta V_{\alpha\beta} * n_\beta \right] + \sqrt{\kappa_\alpha T \bar{\rho}_\alpha} \nabla \cdot \boldsymbol{\zeta}_\alpha. \quad (2.18)$$

Note that at this order, the terms coming from the hydrodynamic interaction disappear as the Oseen tensor and noise correlation function are divergence free. The fluctuations $n_\alpha(\mathbf{x}, t)$ are now Gaussian fields, so that odd correlations such as $C^{(3)}$ are zero.

We now write the dynamics in Fourier space:

$$\dot{\tilde{n}}_\alpha = -\kappa_\alpha T k^2 \tilde{n}_\alpha + i\kappa_\alpha q z_\alpha \mathbf{E} \cdot \mathbf{k} \tilde{n}_\alpha - \kappa_\alpha \bar{\rho}_\alpha k^2 \sum_\beta \tilde{V}_{\alpha\beta} \tilde{n}_\beta + \sqrt{\kappa_\alpha T \bar{\rho}_\alpha} i\mathbf{k} \cdot \tilde{\boldsymbol{\zeta}}_\alpha. \quad (2.19)$$

The dynamics of the fluctuations, Eq. (2.19), can be written in a vectorial form:

$$\dot{\tilde{n}} = -RA\tilde{n} + \chi, \quad (2.20)$$

where $R_{\alpha\beta}(\mathbf{k}) = \delta_{\alpha\beta}\bar{\rho}_\alpha\kappa_\alpha k^2$ is the mobility matrix and A is analogous to the gradient of the potential:

$$A_{\alpha\beta}(\mathbf{k}) = \delta_{\alpha\beta}\frac{T}{\bar{\rho}_\alpha} \left(1 + i\frac{z_\alpha q \mathbf{E} \cdot \mathbf{k}}{Tk^2} \right) + \tilde{V}_{\alpha\beta}, \quad (2.21)$$

we have introduced the scalar Gaussian noise $\chi_\alpha(\mathbf{x}, t)$ with correlation:

$$\langle \chi_\alpha(\mathbf{k}, t) \chi_\beta(\mathbf{k}', t') \rangle = 2(2\pi)^d TR_{\alpha\beta}(\mathbf{k}) \delta(\mathbf{k} + \mathbf{k}') \delta(t - t'). \quad (2.22)$$

In Fourier space, the correlation is given by:

$$\langle \tilde{n}_\alpha(\mathbf{k}, t) \tilde{n}_\beta(\mathbf{k}', t) \rangle = (2\pi)^d \delta(\mathbf{k} + \mathbf{k}') \tilde{C}_{\alpha\beta}(\mathbf{k}, t). \quad (2.23)$$

Using the Itô product rule on Eq. (2.20) we find that the correlation \tilde{C} follows (see Ref. [80], Sec. 4.4):

$$\dot{\tilde{C}} = 2TR - RA\tilde{C} - \tilde{C}A^*R, \quad (2.24)$$

where A^* is the the complex conjugate of A . This is a differential Lyapunov equation [81] and can be casted into a system of ODEs.

When the electric field is constant over the time interval $[0, t]$, which is the case for a switch on or a switch off of the field at $t = 0$, the solution to Eq. (2.24) is given by:

$$\text{vec} \left(\tilde{C}(t) \right) = e^{-Mt} \left[\text{vec} \left(\tilde{C}(0) \right) - 2TM^{-1}\text{vec}(R) \right] + 2TM^{-1}\text{vec}(R), \quad (2.25)$$

where $M = [\mathbb{I} \otimes (RA) + (RA^*) \otimes \mathbb{I}]$. The symbol \otimes is the tensor product and $\text{vec}(\cdot)$ is the vectorization operator. Another option would have been to integrate the differential linear equation (2.20) and then take the average, leading to the solution (2.25) [74–76].

2.3 Binary monovalent electrolyte

To further explore the general formulas derived in section 2.2, we focus on the specific case of binary monovalent electrolyte systems. An ionic solution that is classified as such is one in which there are only two species of particles with opposite charges and the same mobility. This simplification is of interest for two main reasons. First, many ionic solutions in practical use are very close in nature to binary monovalent solutions, as can be seen in Table 2.1. Secondly, this simplification allows us to manipulate analytically and derive some simple form expressions that still capture the global behavior of the system.

Ion	Diffusion Coefficient (cm ² /s)
Li ⁺	1.028×10^{-5}
Na ⁺	1.334×10^{-5}
K ⁺	1.569×10^{-5}
Cl ⁻	2.032×10^{-5}
Br ⁻	2.080×10^{-5}

Table 2.1: Diffusion coefficient $D = T\kappa$ of ions in aqueous solutions, data extracted from [40].

2.4 Dimensionless form

We restrict ourselves to the case of a binary monovalent electrolyte, where both species have the same mobility: $\alpha = \{+, -\}$, $z_+ = -z_- = 1$, $\bar{\rho}_\alpha = \bar{\rho}$, and $\kappa_\alpha = \kappa$.

We nondimensionalize Eq. (2.24) by setting $\tilde{C} = \bar{\rho}\tilde{c}$ and $\mathbf{k} = \mathbf{s}/\lambda_D$ where $\lambda_D = \sqrt{T\varepsilon/(2q^2\bar{\rho})}$ is the Debye length. Then we rescale time by the Debye time $t_D = \lambda_D^2/(\kappa T)$, $t = t_D\tau$. We rewrite the external field to separate the magnitude from the time dependence $E(t) = E_0g(t)$ and introduce the dimensionless field $f = q\lambda_DE_0/T$. The rescaled correlation $c_{\alpha\beta}(\tau)$ follows:

$$\dot{\tilde{c}} = 2s^2 - \omega\tilde{c} - \tilde{c}\omega^*, \quad (2.26)$$

where we have introduced the matrix ω , which is a dimensionless version of RA :

$$\omega_{\alpha\beta}(\mathbf{s}) = \delta_{\alpha\beta} (s^2 + iz_\alpha f s_x) + \frac{z_\alpha z_\beta}{2}. \quad (2.27)$$

Explicit expressions of the dimensionless correlations from Eq. (2.25) are given in App. 5.1 for the NESS to equilibrium and equilibrium to NESS cases.

Applying the same scaling to the current $J(\tau)$ (Eq. (2.17)) we find:

$$\frac{J(\tau)}{\sigma_0 E_0} = g(\tau) + \frac{1}{\bar{\rho}\lambda_D^3} \gamma_{\text{el}}(\tau, f) + g(\tau) \frac{r_s}{\lambda_D} \gamma_{\text{hyd}}(\tau, f), \quad (2.28)$$

where $r_s = (6\pi\eta\kappa)^{-1}$ is the hydrodynamic radius of the charged particles, and the electrostatic and hydrodynamic corrections read, respectively:

$$\gamma_{\text{el}}(\tau, f) = -\frac{1}{16\pi^2 f} \int_0^\infty ds \int_{-1}^1 du \, i s u \sum_{\alpha, \beta} z_\alpha [\tilde{c}_{\alpha\beta}(s, u, \tau, f) - \delta_{\alpha\beta}], \quad (2.29)$$

$$\gamma_{\text{hyd}}(\tau, f) = \frac{3}{4\pi} \int_0^\infty ds \int_{-1}^1 du \, (1 - u^2) \sum_{\alpha, \beta} z_\alpha z_\beta [\tilde{c}_{\alpha\beta}(s, u, \tau, f) - \delta_{\alpha\beta}]. \quad (2.30)$$

We have introduced the variable $u = s_x/s$. The dimensionless parameters in front of the correction terms in Eq. (2.28) imply that none can be neglected, and we study them separately. Note that the electrostatic correction involves the odd part of the correlations, as the prefactor is odd in the variable u , while the hydrodynamic correction involves the

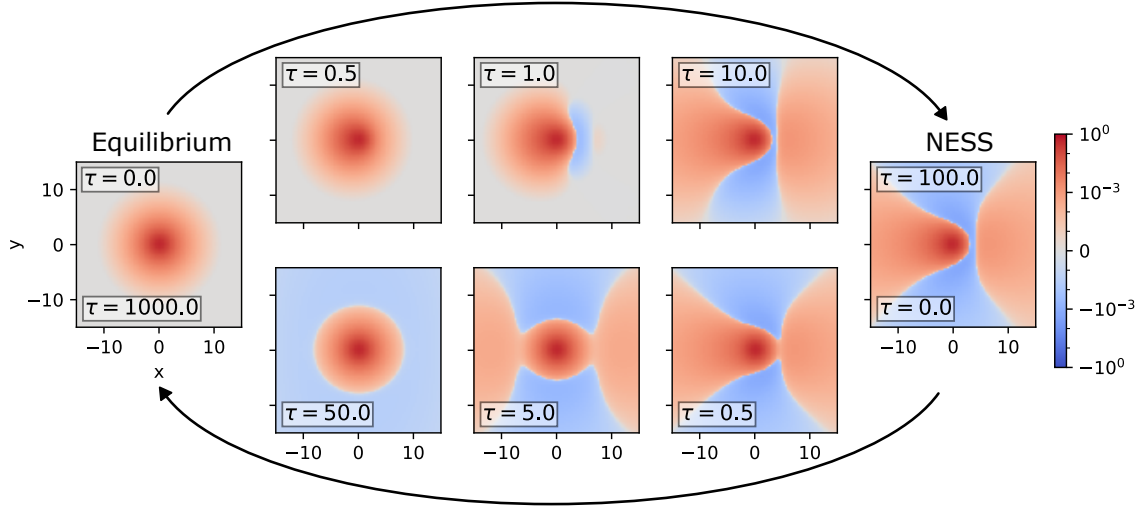


Figure 2.1: Evolution of the correlation $c_{-+}(\mathbf{x})$ in a binary monovalent electrolyte for $f = 1$, from equilibrium to NESS (top row), and from NESS to equilibrium (bottom row). The field is oriented along x .

even part of the correlation. Note also that the hydrodynamic correction is multiplied by the time dependence of the electric field, $g(\tau)$, hence it is absent in the transition from NESS to equilibrium.

The corrections in the steady state have been computed previously [24, 60]:

$$\gamma_{\text{el}}^{\infty} = -\frac{1}{32\pi f^3} \left[f\sqrt{f^2+1} - \sqrt{2}f + \tan^{-1}(\sqrt{2}f) - \tan^{-1}\left(\frac{f}{\sqrt{f^2+1}}\right) \right], \quad (2.31)$$

$$\begin{aligned} \gamma_{\text{hyd}}^{\infty} = & -\frac{1}{\sqrt{2}} - \frac{3(\sqrt{2} - \sqrt{f^2+1})}{8f^2} - \frac{3}{4f} \sinh^{-1}(f) \\ & + \frac{3(1+2f^2)}{8f^3} \left[\tan^{-1}(\sqrt{2}f) - \tan^{-1}\left(\frac{f}{\sqrt{f^2+1}}\right) \right]. \end{aligned} \quad (2.32)$$

2.4.1 Correlations from equilibrium to NESS and back

We present the evolution of the pair correlations for different species, c_{+-} , for the transitions from equilibrium to NESS, and from NESS to equilibrium, in Fig. 2.1. We see that the trajectory from NESS to equilibrium is not the inverse of the trajectory from equilibrium to NESS. In particular, it seems that from NESS to equilibrium, the correlation quickly becomes symmetric before slowly relaxing to its equilibrium value. In the next sections, we focus on the behavior of the conductivity, which we finally compare to the evolution of the correlation.

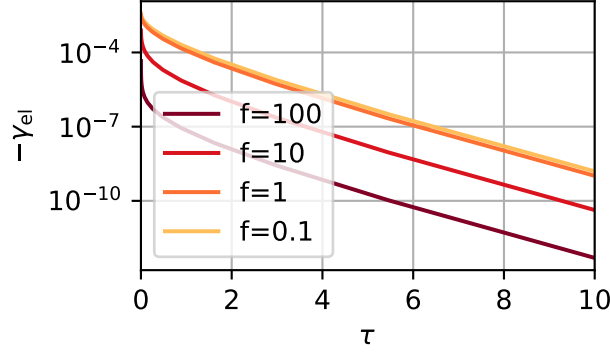


Figure 2.2: Electrostatic correction term $\gamma_{\text{el}}(\tau)$ from NESS to equilibrium (Eq. (2.33), integrated numerically) as a function of time for different values of the field f .

2.5 From NESS to equilibrium

We start by studying the dynamics of the conductivity as a response to a sudden switch off of the electric field (NESS to equilibrium). We solve Eq. (2.26) under $f = 0$ with the initial condition being the steady state solution to Eq. (2.26) for a finite value of f . After the switch off of the field, the bare current is zero, hence the only current comes from the out of equilibrium correlations through the electrostatic correction, as there is no hydrodynamic correction in this case.

By plugging the solution of Eq. (2.26) as described to Eq. (2.29), we find that the electrostatic correction is

$$\gamma_{\text{el}}(\tau) = -\frac{1}{8\pi^2 f} \int_0^\infty ds \int_{-1}^1 du \frac{s^2 u^2 e^{-(2s^2+1)\tau}}{(2s^2+1)(f^2 u^2 + s^2 + 1)}. \quad (2.33)$$

This integral is integrated numerically with the package Quadpack implemented in SciPy [82, 83]; it is plotted as a function of time in Fig. 2.2. Differentiating Eq. (2.33), one can show that the correction decays monotonically, as seen in Fig. 2.2.

At short time, the electrostatic correction behaves as:

$$\gamma_{\text{el}}(\tau) \underset{\tau \rightarrow 0}{\sim} \frac{\sqrt{\tau}}{12\sqrt{2}\pi^{3/2}}. \quad (2.34)$$

At long times, it decays exponentially:

$$\gamma_{\text{el}}(\tau) \underset{\tau \rightarrow \infty}{\sim} -\frac{e^{-\tau} [f - \tan^{-1}(f)]}{32\sqrt{2}\pi^{3/2} f^3 \tau^{3/2}}, \quad (2.35)$$

with a field dependent prefactor that is constant at weak field and decays as f^{-2} at large field (Fig. 2.3).

As a conclusion, after a switch off of the external field there is a recoil coming from the

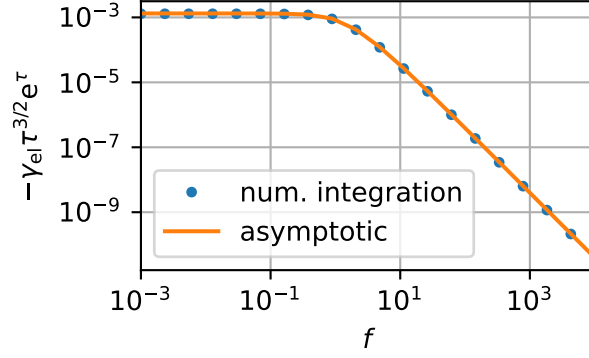


Figure 2.3: Field dependency of the electrostatic correction $\gamma_{el}(\tau)$ at large time. Analytical result (Eq. (2.35), solid line) and from numerical integration of Eq. (2.33) at $\tau = 100$ (dots).

electrostatic correction. This recoil decays exponentially on the time scale of the Debye time. This decay is compatible with the evolution of the correlations (Fig. 2.1): the antisymmetric part, which enters in the electrostatic correction, indeed seems to decay on the time scale of the Debye time.

2.6 From equilibrium to NESS

We now turn to the dynamics of the conductivity after a sudden switch on of the electric field, the system being initially in its equilibrium state. Here both electrostatic and hydrodynamic corrections are present, and we study them separately.

2.6.1 Electrostatic correction

The integrand of γ_{el} in Eq. (2.29), which we denote $y(s, u, f, \tau)$ is obtained from the solution (2.25):

$$y(s, u, f, \tau) = \frac{2fs^2u^2e^{-\tau(2s^2+1)}}{(s^2+1)(2s^2+1)(f^2u^2+s^2+1)(1-4f^2s^2u^2)} \left[- (f^2u^2 + s^2 + 1) + f^2u^2(2s^2+1) \left((2s^2+1) \cosh\left(\tau\sqrt{1-4f^2s^2u^2}\right) + \sqrt{1-4f^2s^2u^2} \sinh\left(\tau\sqrt{1-4f^2s^2u^2}\right) \right) \right] + \frac{2fs^2u^2}{(2s^2+1)(f^2u^2+s^2+1)}. \quad (2.36)$$

The last term in y is independent of time and corresponds, after integration, to the steady state result γ_{el}^∞ (Eq. (2.31)). Note that the integrand is regular at the pole corresponding to $4s^2u^2f^2 = 1$ (App. 5.3).

The electrostatic correction is integrated numerically and shown as a function of time in Fig. 2.4(a) for different values of the field. Contrary to the monotonic behavior from NESS to equilibrium, here we observe an overshoot of the conductivity, which has a global minimum, lower than the steady state value γ_{el}^∞ . The time location of the minimum

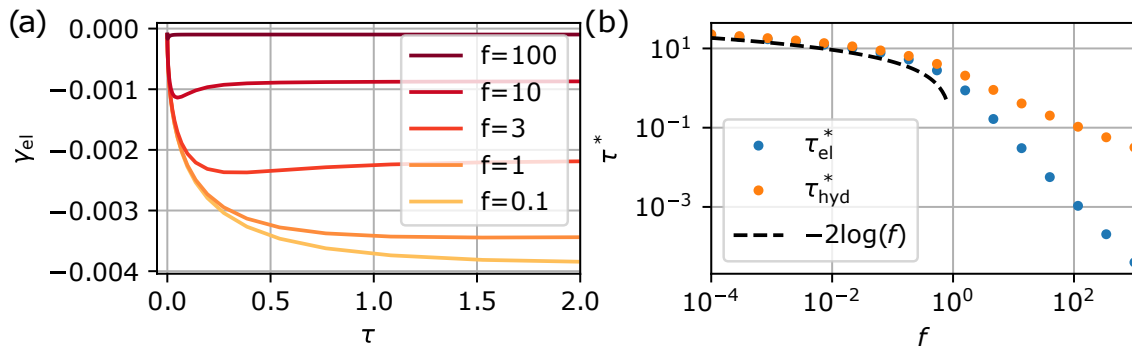


Figure 2.4: (a) Electrostatic correction $\gamma_{\text{el}}(\tau)$ from equilibrium to NESS from numerical integration of Eq. (2.29), for different values of the field f . (b) Times $\tau_{\text{el}}^*(f)$ and $\tau_{\text{hyd}}^*(f)$ of the extrema of the electrostatic and hydrodynamic corrections, as a function of the magnitude of the external field f . Numerical evaluation of the time location of the extrema for the electrostatic correction (blue points) and for the hydrodynamic correction (orange points), and weak field asymptotics (2.46,2.55) (solid line).

as a function of the field, $\tau_{\text{el}}^*(f)$, is shown in Fig. 2.4(b): we see that the minimum is always present and that it occurs sooner and sooner as the field increases. We also observe in Fig. 2.4(a) that the correction converges to a well defined limit at weak field, which corresponds to the linear response of the system. We now focus on the short and long time behaviors of the correction.

Short time limit

The behavior of the conductivity can be obtained by the change of variables $w = \sqrt{\tau}s$ followed by a Taylor expansion of the integrand to lowest order around $\tau \rightarrow 0$, leading to:

$$\gamma_{\text{el}}(\tau) \underset{\tau \rightarrow 0}{\sim} -\frac{1}{16\pi^2} \sqrt{\tau} \int_0^\infty dw \int_{-1}^1 du u^2 \frac{1 - e^{-2w^2}}{w^2}. \quad (2.37)$$

Note that to obtain the asymptotic form, the steady state part of the integrand in Eq. (2.29) cannot be computed separately, but has to be part of the expanded expression. Evaluating the integral gives:

$$\gamma_{\text{el}}(\tau) \underset{\tau \rightarrow 0}{\sim} -\frac{\sqrt{\tau}}{12\sqrt{2}\pi^{\frac{3}{2}}}. \quad (2.38)$$

The short time asymptotics is compared to the numerical integration in Fig. 2.5. We recover the square root dependence observed from NESS to equilibrium. Interestingly, the short time asymptotics does not depend on the field; as this is the correction to the conductivity, it means that the short time response is linear. However, the higher the field is, the sooner the conductivity departs from the short time asymptotics.

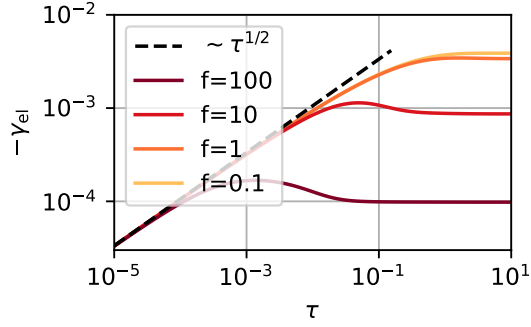


Figure 2.5: Short time behavior of the electrostatic correction. Numerical integration for different values of the field (solid lines) and short time asymptotics (Eq. (2.38), dashed line).

Long time limit

To estimate the behavior of the conductivity at long times, we first separate the time independent part in the integrand (2.36), which integrates to $\gamma_{\text{el}}^{\infty}$. The remaining time dependent part of the integrand gives us access to the large time asymptotic behavior of the conductivity. We perform the same change of variables $w = \sqrt{\tau}s$ and expand the integrand to the lowest order around $\tau \rightarrow \infty$, yielding:

$$\gamma_{\text{el}}(\tau) - \gamma_{\text{el}}^{\infty} \underset{\tau \rightarrow \infty}{\sim} -\frac{1}{16\pi^2} \frac{1}{\tau^{3/2}} \int_0^{\infty} dw \int_{-1}^1 du \frac{2w^2 u^4 f^4 e^{-2w^2}}{(f^2 u^2 + 1)} e^{-2f^2 w^2 u^2}. \quad (2.39)$$

Evaluating the integral gives:

$$\gamma_{\text{el}}(\tau) - \gamma_{\text{el}}^{\infty} \underset{\tau \rightarrow \infty}{\sim} -\frac{3(f^2 + 1)^{3/2} \sinh^{-1}(f) - 4f^3 - 3f}{96\sqrt{2}\pi^{3/2} f^3 (f^2 + 1)^{3/2} \tau^{3/2}}. \quad (2.40)$$

The algebraic decay of the electrostatic correction is visible in the numerical evaluation in Fig. 2.6(a); the prefactor obtained from the numerical evaluation is compared to the expression (2.40) in Fig. 2.6(b).

Our main observation is that the relaxation of the electrostatic correction towards its stationary value is algebraic, $\gamma_{\text{el}}(\tau) - \gamma_{\text{el}}^{\infty} \sim \tau^{-3/2}$, contrary to the exponential relaxation when going from NESS to equilibrium. This algebraic behavior is reminiscent of the one seen for the relaxation of the long range force between two boundaries of an electrolyte in the same configuration [74]. As the prefactor of the algebraic decay goes to zero as the field goes to zero, it is a non-linear effect. To better understand the non-linear effects, we turn to focus on the weak field limit.

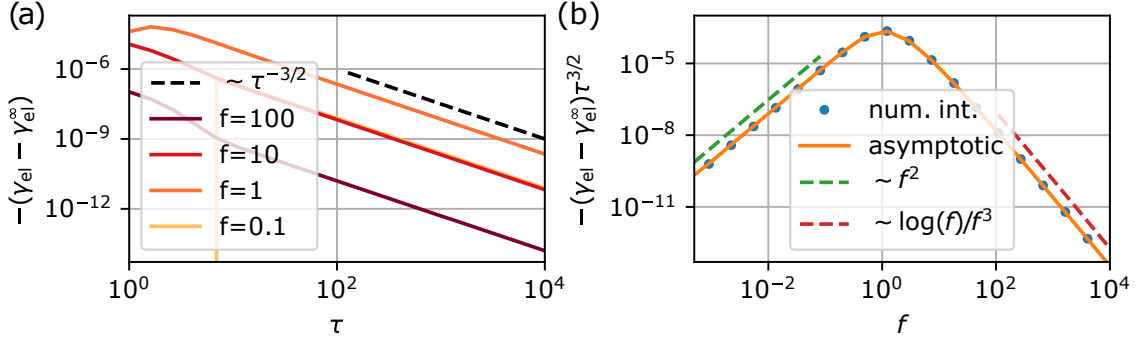


Figure 2.6: Long time behavior of the electrostatic correction. (a) Difference with the stationary value as a function of time for different values of the field (solid lines) and $\tau^{-3/2}$ power law (dashed line). Note that the correction is regular, the apparent jump for $f = 0.1$ is due to the logarithmic scale. (b) Prefactor of the algebraic decay as a function of the field f from numerical integration (blue points), from the long time asymptotics (Eq. (2.40), solid line), and small and large field asymptotics (dashed lines).

Weak field limit

The weak field limit of the electrostatic correction can be obtained by expanding the integrand (2.36), leading to:

$$\gamma_{\text{el}} = \sum_{n=0}^{\infty} f^{2n} \gamma_{\text{el}}^{(2n)}. \quad (2.41)$$

The first two terms are:

$$\gamma_{\text{el}}^{(0)}(\tau) = -\frac{\sqrt{2} \operatorname{erfc}(\sqrt{\tau}) - 2e^{\tau} \operatorname{erfc}(\sqrt{2\tau}) + 2 - \sqrt{2}}{48\pi}, \quad (2.42)$$

$$\begin{aligned} \gamma_{\text{el}}^{(2)}(\tau) = \frac{1}{20\pi} & \left[\frac{3 - 2\sqrt{2}}{4} + \frac{4\tau - 8e^{\tau} + 2e^{2\tau} + 3}{4} \operatorname{erfc}(\sqrt{2\tau}) \right. \\ & \left. + \frac{\sqrt{\pi} \operatorname{erfc}(\sqrt{\tau}) - e^{-2\tau} \sqrt{\tau}}{\sqrt{2\pi}} - \frac{(1 - e^{-\tau})^2}{2\sqrt{2\pi\tau}} \right]. \end{aligned} \quad (2.43)$$

The long time behavior of the lowest order term (Eq. (2.42)) is given by:

$$\gamma_{\text{el}}^{(0)}(\tau) - \gamma_{\text{el}}^{\infty(0)} \underset{\tau \rightarrow \infty}{\sim} \frac{e^{-\tau}}{96\sqrt{2}\pi^{3/2}\tau^{3/2}}. \quad (2.44)$$

It decays exponentially, confirming that the algebraic decay at finite field is rooted in the non-linear response. Moreover, the asymptotics (2.44) matches exactly the long time asymptotics when going from NESS to equilibrium (obtained from a weak field expansion of Eq. (2.35)). Indeed, expanding the equation (2.26) for the correlation at weak field reveals that the NESS to equilibrium and equilibrium to NESS trajectories are identical in the linear regime.

At the next order, the algebraic behavior is recovered:

$$\gamma_{\text{el}}^{(2)}(\tau) - \gamma_{\text{el}}^{\infty(2)} \underset{\tau \rightarrow \infty}{\sim} -\frac{1}{160\sqrt{2}\pi^{3/2}\tau^{3/2}}, \quad (2.45)$$

in agreement with the f^2 dependence of the prefactor of the algebraic decay (Fig. 2.6(b)).

The lowest order term, $\gamma_{\text{el}}^{(0)}(\tau)$, is a decreasing function of τ , while the next order, $\gamma_{\text{el}}^{(2)}(\tau)$, is increasing. The time location of the minimum, τ_{el}^* , can be obtained at low field by comparing these two terms. As τ_{el}^* seems to diverge as the field goes to zero (Fig. 2.4(b)), it is sufficient to use the long time asymptotics, Eqs. (2.44, 2.45). Differentiating the long time asymptotics of $\gamma_{\text{el}}^{(0)}(\tau) + f^2\gamma_{\text{el}}^{(2)}(\tau)$ gives the following equation for the time location of the minimum: $9f^2e^\tau - 10\tau - 15 = 0$. To leading order in f , the solution is:

$$\tau_{\text{el}}^*(f) \underset{f \rightarrow 0}{\sim} -2\log(f). \quad (2.46)$$

This asymptotic behavior is compared to the numerical evaluation of the time location of the minimum in Fig. 2.4(b).

2.6.2 Hydrodynamic correction

The integrand of γ_{hyd} in Eq. (2.30), which we denote $h(s, u, f, \tau)$ is obtained from the solution (2.25):

$$\begin{aligned} h(s, u, f, \tau) = & -\frac{f^2 s^2 u^2 (u^2 - 1) e^{-\tau(2s^2+1)}}{(s^2 + 1) (2s^2 + 1) (f^2 u^2 + s^2 + 1) (1 - 4f^2 s^2 u^2)^{3/2}} \\ & \times \left(-4 (f^2 u^2 + s^2 + 1) \sqrt{1 - 4f^2 s^2 u^2} \right. \\ & + (2s^2 + 1) \left[2f^2 u^2 \left(\sqrt{1 - 4f^2 s^2 u^2} + 2s^2 \right) + \sqrt{1 - 4f^2 s^2 u^2} - 1 \right] e^{\tau \sqrt{1 - 4f^2 s^2 u^2}} \\ & \left. + (2s^2 + 1) \left[2f^2 u^2 \left(\sqrt{1 - 4f^2 s^2 u^2} - 2s^2 \right) + \sqrt{1 - 4f^2 s^2 u^2} + 1 \right] e^{-\tau \sqrt{1 - 4f^2 s^2 u^2}} \right) \\ & + \frac{2 (u^2 - 1) (f^2 u^2 + 2s^2 + 1)}{(2s^2 + 1) (f^2 u^2 + s^2 + 1)}. \quad (2.47) \end{aligned}$$

The last term in h is independent of time and corresponds to the steady state correction $\gamma_{\text{hyd}}^\infty$ (Eq. (2.32)).

The hydrodynamic correction is integrated numerically and shown as a function of time in Fig. 2.7. The main difference with the electrostatic correction is the finite value at $\tau = 0$. This is due to the fact that the hydrodynamic correction involves the even part of the correlation, which is finite for the equilibrium initial condition. As for the electrostatic correction, the relaxation towards the stationary value is non-monotonic; the time location of the maximum as a function of the field is plotted in Fig. 2.4(b). We now study the short and long time behaviors of the correction.

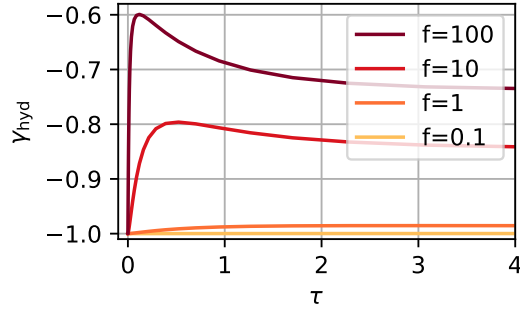


Figure 2.7: Hydrodynamic correction $\gamma_{\text{hyd}}(\tau)$ from equilibrium to NESS from numerical integration of Eq. (2.30) for different values of the field f .

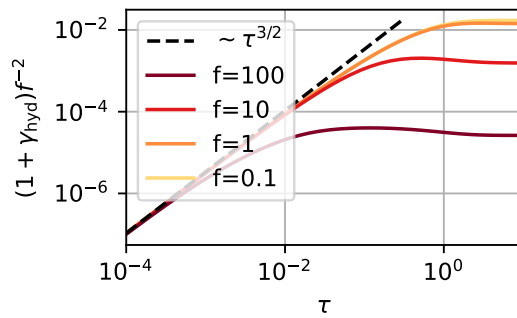


Figure 2.8: Short time behavior of the hydrodynamic correction. Numerical integration for different values of the field (solid lines) and short time asymptotics (Eq. (2.48), dashed line).

Short time limit

Using the same method as for the electrostatic correction, we find the short time behavior of the hydrodynamic correction. We find $\gamma_{\text{hyd}}(\tau) \xrightarrow{\tau \rightarrow 0} -1$ and

$$\gamma_{\text{hyd}}(\tau) + 1 \underset{\tau \rightarrow 0}{\sim} \frac{2}{15} \sqrt{\frac{2}{\pi}} f^2 \tau^{3/2}; \quad (2.48)$$

it is compared to the numerical integration in Fig. 2.8. The short time evolution is slower than for the electrostatic correction and depends on the field. We also observe that the departure from the short time asymptotics occurs sooner for a larger field.

Long time limit

To estimate the behavior of the hydrodynamic correction at long times, we first separate the time independent part in the integrand (2.47), which integrates to $\gamma_{\text{hyd}}^\infty$. The remaining time dependent part of the integrand gives us access to the large time asymptotic behavior of the conductivity. We perform the same change of variables, $w = \sqrt{\tau}s$ and then expand

the integrand to the lowest order around $\tau \rightarrow \infty$, yielding:

$$\gamma_{\text{hyd}}(\tau) - \gamma_{\text{hyd}}^{\infty} \underset{\tau \rightarrow \infty}{\sim} \frac{1}{16\sqrt{2\pi}\tau^{3/2}} \left[\frac{15 + 6f^2}{f^3} \sinh^{-1}(f) - \frac{15 + 11f^2}{f^2\sqrt{f^2 + 1}} \right]. \quad (2.49)$$

This asymptotics is compared to the numerical integration in Fig. 2.9(a). We find again an algebraic relaxation towards the stationary value, with the same exponent $3/2$ as for the electrostatic correction. Similarly, the prefactor goes to zero as the field goes to zero (Fig. 2.9(b)), indicating that the algebraic decay is a non-linear effect.

Weak field limit

The weak field limit of the hydrodynamic correction can be obtained by expanding the integrand (2.47), leading to:

$$\gamma_{\text{hyd}} = \sum_{n=0}^{\infty} f^{2n} \gamma_{\text{hyd}}^{(2n)}. \quad (2.50)$$

The lowest order term is $\gamma_{\text{hyd}}^{(0)}(\tau) = -1$. It relaxes instantaneously, so that its difference with its value in the stationary state is zero, mirroring the absence of the hydrodynamic correction when going from NESS to equilibrium. This instantaneous relaxation also shows that the algebraic decay is, as for the electrostatic correction, a non-linear effect.

The following terms are:

$$\gamma_{\text{hyd}}^{(2)} = \frac{3 - 2\sqrt{2}}{10} + \frac{1}{10} \left[(4\tau - 4e^{\tau} + 1) \operatorname{erfc}(\sqrt{2\tau}) + 2\sqrt{2} \operatorname{erfc}(\sqrt{\tau}) - 2\sqrt{\frac{2}{\pi}} e^{-2\tau} \sqrt{\tau} \right], \quad (2.51)$$

$$\begin{aligned} \gamma_{\text{hyd}}^{(4)} = & \frac{3}{280} (16\sqrt{2} - 23) + \frac{3}{280} \left[- (16\tau^2 + 48\tau - 64e^{\tau} + 8e^{2\tau} + 33) \operatorname{erfc}(\sqrt{2\tau}) \right. \\ & \left. - 16\sqrt{2} \operatorname{erfc}(\sqrt{\tau}) + 2\sqrt{\frac{2}{\pi}} e^{-2\tau} \frac{4\tau^2 + 11\tau - 8e^{\tau} + 2e^{2\tau} + 6}{\sqrt{\tau}} \right]. \end{aligned} \quad (2.52)$$

They behave at long time as:

$$\gamma_{\text{hyd}}^{(2)}(\tau) - \gamma_{\text{hyd}}^{\infty(2)} \underset{\tau \rightarrow \infty}{\sim} \frac{e^{-2\tau} - 2e^{-\tau}}{20\sqrt{2\pi}\tau^{3/2}}, \quad (2.53)$$

$$\gamma_{\text{hyd}}^{(4)}(\tau) - \gamma_{\text{hyd}}^{\infty(4)} \underset{\tau \rightarrow \infty}{\sim} \frac{3}{140\sqrt{2\pi}\tau^{3/2}}. \quad (2.54)$$

Here, the algebraic decays appears at the fourth order in the field, in agreement with the f^4 dependence of the prefactor of the algebraic decay (Fig. 2.9(b)).

Finally, as for the electrostatic correction, comparing the orders 2 and 4 (Eqs. (2.53, 2.54)) allows to find the asymptotic behavior of the time location of the minimum at weak field:

$$\tau_{\text{hyd}}^*(f) \underset{f \rightarrow 0}{\sim} -2 \log(f). \quad (2.55)$$

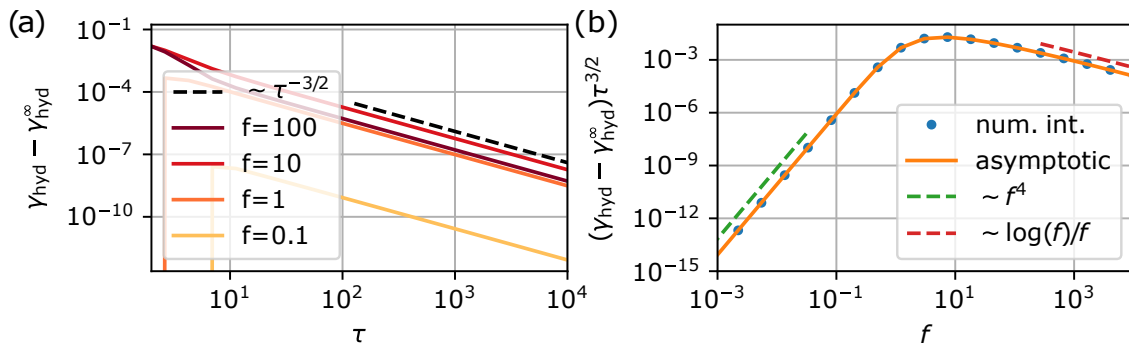


Figure 2.9: Long time behavior of the hydrodynamic correction. (a) Difference with the stationary value as a function of time for different values of the field (solid lines) and $\tau^{-3/2}$ power law (dashed line). (b) Prefactor of the algebraic decay as a function of the field from numerical integration (blue points), from the long time asymptotics (Eq. (2.49)), and small and large field asymptotics (dashed lines).

This asymptotics is the same as for the electrostatic correction Fig. 2.4(b).

2.7 Conclusions

In this chapter we have computed the transient ionic correlations in an electrolyte under a sudden switch on or off of an external electric field of arbitrary magnitude using linearized SDFT. It was shown that the correlations do not follow the same trajectory when the field is turned on or off. Using SDFT formalism, we derived an exact expression for the total electric current in terms of the two-point and three-point correlation functions. We used linearized SDFT to compute the correlation function and derived the electrostatic and hydrodynamic corrections from the ionic correlations. When the field is turned off, the hydrodynamic correction is absent and the electrostatic correction decays exponentially. This fast decay seems to correspond to the fast decay of the odd part of the correlations; in contrast, the even part of the correlations, which is not involved in the electrostatic correction, decays more slowly. On the contrary, when the field is switched on, we found that both corrections algebraically relax to their stationary value with the same exponent. In the linear response regime, an exponential relaxation is recovered when the field is switched on, showing that the algebraic relaxation is a nonlinear effect.

Chapter 3

Correlations in electrolyte systems – Long range behavior

The results presented in this chapter are based on unpublished work.

In the previous chapter, the electrostatic and hydrodynamic corrections to the conductivity were given in terms of the ionic correlation functions (Eqs. (2.29,2.30)), and we discussed the relationship between the temporal behavior of the correlations and the conductivity corrections. However, the discussion of the evolution of the correlations was limited to qualitative aspects. In fact, while in equilibrium the correlations are of the Yukawa form, isotropic and decaying exponentially with distance, in the NESS they are long range [66]. The algebraic decay of the correlations out of equilibrium has been shown to give rise to long-range forces, but it has not been precisely characterized in the steady state, nor in the transient regime.

A better understanding of the behavior of the correlations at large distances (compared to the Debye length λ_D) might suggest a certain degree of universality of the correlation function in driven systems with long-range interacting particles. Such a characterization has been obtained for a driven binary mixture with short-range interactions [70]. Although the correlations of both systems are short-range at equilibrium and long-range at the NESS, as we will see in this chapter, the correlation structure is intrinsically different. Examining Fig. 3.1, which presents the NESS correlation elements in real space at large distances, we can see a clear conical structure. This unique conical shape that changes its head angle with the external field in a non trivial way raises the question of its origin. In general, the small wavenumber limit of the correlation function in Fourier space contains thermodynamic information related to isothermal compressibility [84]. Finally, the dynamics of the correlation at large distances and long times (compared to the Debye length and time λ_D, t_D) after switching on the driving field will allow us to rationalize the algebraic relaxation of the conductivity found in the previous chapter.

3.1 Stationary case

We begin by considering the simpler case of the non-equilibrium steady state. The correlation elements in Fourier space for binary monovalent electrolytes can be calculated using

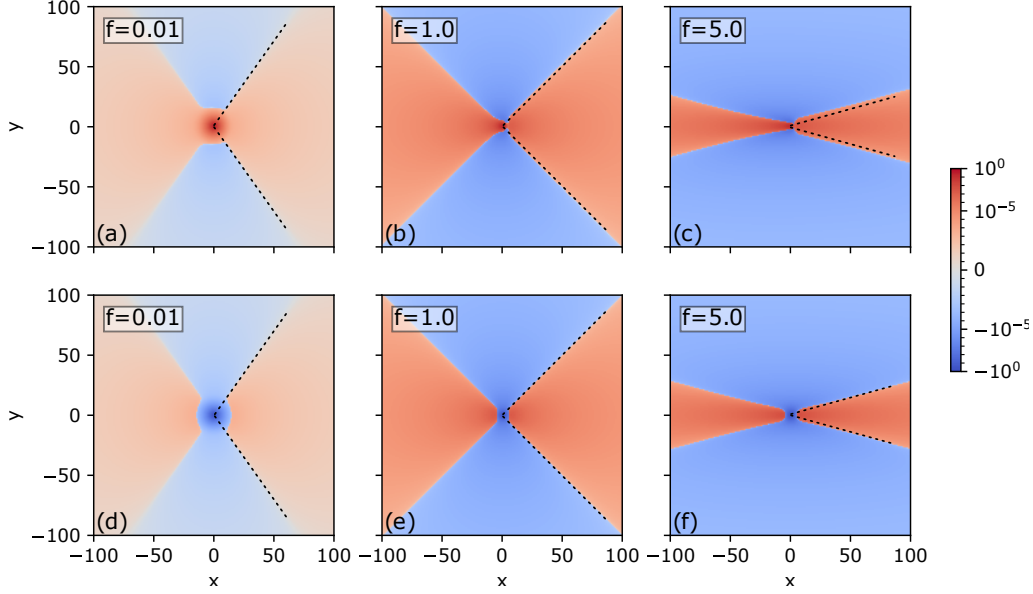


Figure 3.1: The correlation function in the non-equilibrium steady state, for different values of the normalized external field f . panels (a,b,c) are the anion-cation correlation c_{-+} and panels (d,e,f) are the equal charge correlation $c_{\alpha\alpha}$. One can observe that far from the origin, a cone develops and that at vanishing fields the angle of the cone reaches a finite value, as predicted in Eq. (3.12). Surprisingly, the long-range shape of any ion-ion correlation function is the same. In dashed black line is the prediction of Eq. (3.12).

Eq. (2.26). In the steady state case, as shown in [60], the equation reduces to a set of algebraic equations to which the solution is:

$$\tilde{c}(\mathbf{s}) = \frac{s^2}{2(1+2s^2)(s^2+s^4+f^2s_{\parallel}^2)} \begin{pmatrix} 1+4s^2+4s^4+4f^2s_{\parallel}^2 & 1+2s^2-2ifs_{\parallel} \\ 1+2s^2+2ifs_{\parallel} & 1+4s^2+4s^4+4f^2s_{\parallel}^2 \end{pmatrix}. \quad (3.1)$$

We remind the reader that the system of equations is dimensionless and that the length is measured in Debye length units. We arrange the correlation terms in this way, which is not necessarily the most reduced version, to make the behavior around the origin more visible. Note that the diagonal terms (\tilde{c}_{++} and \tilde{c}_{--}) include the self-interaction term, which is a constant in Fourier space and a delta function centered out the origin in real space. Since we are focusing on the large distance behavior, this will not affect the result we derive.

3.1.1 Discontinuity at small wave number

Examining $\tilde{c}(\mathbf{s})$, we see that there is a discontinuity at the origin, since approaching the origin from the direction perpendicular or parallel to the electric field does not have the same limit:

$$\tilde{c}_{\alpha\beta}(s_{\parallel}=0, s_{\perp}) \underset{s_{\perp} \rightarrow 0}{=} \frac{1}{2} \quad \tilde{c}_{\alpha\beta}(s_{\parallel}, s_{\perp}=0) \underset{s_{\parallel} \rightarrow 0}{=} \frac{1}{2(1+f^2)} \quad (3.2)$$

The fact that the Fourier transform of the correlation function is not continuous at the origin usually indicates an algebraic decay in real space. To determine the long-range properties of the correlation function, we can separate this discontinuity from the full expression. By doing so, we are left with a term called the singular part \tilde{c}_s , which encompasses the discontinuity and accounts for the long range behavior in real space, and the rest, namely $\tilde{c} - \tilde{c}_s$, which is (more) regular at the origin and hence its contribution decays faster in real space.

Note that with this definition, the singular part is defined up to a regular function. We can extract the discontinuity from Eq. (3.1) by recalling that $s^2 = s_{\perp}^2 + s_{\parallel}^2$ and discarding higher powers of s_{\perp} and s_{\parallel} . This way we find the singular part, which is identical for all correlation elements:

$$\tilde{c}_s = \frac{s^2}{2(s^2 + f^2 s_{\parallel}^2)} \quad (3.3)$$

One can verify that subtracting this term from the correlation elements regularizes the behavior at the origin, and the regularized term goes to 0 as s goes to 0. Therefore, the inverse Fourier transform of the singular part is the behavior of the correlation elements at long distances in real space. We can calculate the its inverse Fourier transform:

$$c_s = \frac{1}{(2\pi)^d} \int ds \frac{s^2}{2(s^2 + f^2 s_{\parallel}^2)} e^{-isx}. \quad (3.4)$$

One can rewrite the expression as the Laplacian of an integral:

$$c_s = -\frac{1}{2(2\pi)^d} \nabla_x^2 \int ds \frac{e^{-isx}}{s^2 + f^2 s_{\parallel}^2}. \quad (3.5)$$

Separating the variable s to the parallel and perpendicular parts we get:

$$c_s = -\frac{1}{2(2\pi)^d} \nabla_x^2 \int ds \frac{e^{-isx}}{s_{\perp}^2 + (1 + f^2) s_{\parallel}^2}. \quad (3.6)$$

Now we apply the following change the variables $\hat{s} = \{s_{\parallel} \sqrt{1 + f^2}, s_j\}$ and $\hat{x} = \{x_{\parallel} / \sqrt{1 + f^2}, x_j\}$, where x_j and s_j represent all the perpendicular axes. One gets in the new variables:

$$c_s = -\frac{1}{2\sqrt{1 + f^2} (2\pi)^d} \nabla_x^2 \int d\hat{s} \frac{e^{-i\hat{s}\hat{x}}}{\hat{s}^2}, \quad (3.7)$$

which can be written in terms of the Green's function for the electrostatic interaction:

$$c_s = -\frac{1}{2\sqrt{1 + f^2} (2\pi)^d} \nabla_x^2 G_{es}(\hat{x}). \quad (3.8)$$

This expression can be evaluated in d dimensions to get:

$$c_s = -\frac{f^2}{4\pi^{d/2}} (f^2 + 1)^{\frac{d-3}{2}} \Gamma\left(\frac{d}{2}\right) g_d\left(\sqrt{1+f^2}\frac{x_\perp}{x_\parallel}\right) \quad \text{with} \quad g_d(y) = \frac{y^2 - (d-1)}{(y^2 + 1)^{\frac{d}{2}+1}}, \quad (3.9)$$

where Γ is the gamma function. When we set the dimension to $d = 3$, we get:

$$c_s = -\frac{1}{8\pi\sqrt{1+f^2}} \nabla_x^2 \frac{1}{\sqrt{x_\perp^2 + \frac{x_\parallel^2}{1+f^2}}}. \quad (3.10)$$

One can see that this function can be written as:

$$c_s = -\frac{f^2}{8\pi x_\parallel^3} g_3\left(\sqrt{1+f^2}\frac{x_\perp}{x_\parallel}\right) \quad \text{with} \quad g_3(y) = \frac{y^2 - 2}{(y^2 + 1)^{5/2}}. \quad (3.11)$$

The expression in Eq. (3.11) has several interesting features. First, as the argument of the function g_3 , which contains the ratio between x_\parallel and x_\perp , implies the conical shape that is clearly visible in Fig. 3.1. This is an intrinsic difference from systems with short-range interactions. Both types of systems – those with short-range interactions and those with long-range interactions – exhibit short-range particle-particle correlation functions at equilibrium. Out of equilibrium, however, the correlations become long-range. Yet the structure of the correlation function is different. In systems with short-range interactions, instead of a cone, we find a paraboloid aligned with the driving field [70]. Second, the angle of the cone does not approach $\frac{\pi}{2}$, as one might expect, while the field is decreased towards zero. Instead, it settles at an angle, unlike for example, the Mach cone. Finally, the way Eq. (3.11) is arranged shows that there is a self-similar shape for each cut along the x_\parallel axis. In fact, by stretching this scaling function g_d by the factor $\sqrt{1+f^2}$, we find a universal shape for any cut and external field. We can see the shape of the function g_3 against a numerical inversion of the Fourier transform of the correlation element in Fig. (3.2).

From Eq. (3.9) we can see that the angle Θ of the cone where the value of the correlation is 0 is given by:

$$\Theta_d = \sin^{-1}\left(\sqrt{\frac{d-1}{d+f^2}}\right) \quad (3.12)$$

This expression shows that the angle of the cone in any dimensions does not converge to $\pi/2$, as one might expect, and that the spherically symmetric correlation shape is not recovered by decreasing the magnitude of the external field f . This prediction is clear in Fig. (3.1) where the limiting angle will be $\Theta_3 = \sin^{-1}\left(\sqrt{\frac{2}{3}}\right) \approx 54.74^\circ$.

3.1.2 quadrupole potential

To get insight into the shape of the correlations, we draw the following analogy with a quadrupole moment potential. Consider the following configuration of 4 point charges : 2 negative charges are placed at the origin and one positive point charge is placed at each

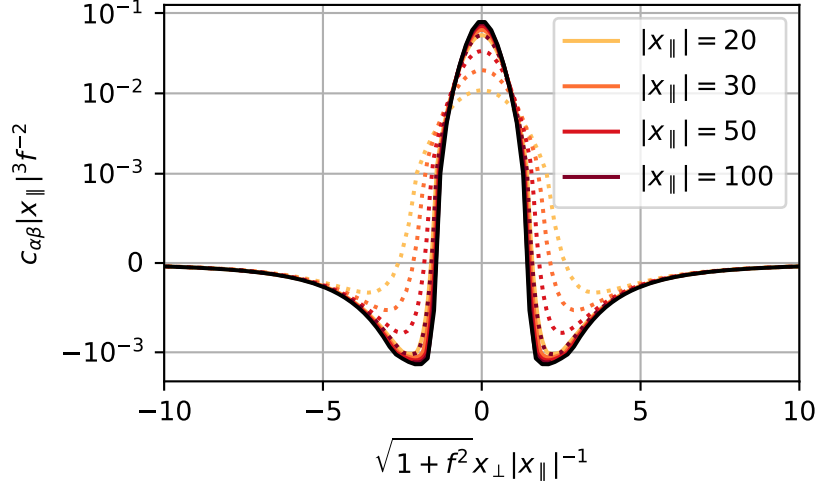


Figure 3.2: The correlation function times $|x_{\parallel}|^3 f^{-2}$ along slices of constant x_{\parallel} values. This allows us to compare it to the scaling function g_3 . The dotted lines correspond to $f = 1$ while the solid lines correspond to $f = 5$. We can see in solid black the evaluation of Eq. (3.11).

side of the negative ones, along the x_{\parallel} axis, at distance b . See Fig. 3.3 for an illustration of the charge layout. The electric potential in space would be:

$$\phi = \frac{q}{4\pi\epsilon\ell} \left(\frac{1}{\sqrt{x_{\perp}^2 + (x_{\parallel} - b)^2}} - \frac{2}{\sqrt{x_{\perp}^2 + x_{\parallel}^2}} + \frac{1}{\sqrt{x_{\perp}^2 + (x_{\parallel} + b)^2}} \right), \quad (3.13)$$

where ℓ is the length unit and x_{\parallel}, x_{\perp} and b are dimensionless. Expanding this formula around small values of b , one finds:

$$\phi = -\frac{b^2 q}{4\pi\epsilon\ell x_{\parallel}^3} g_3 \left(\frac{x_{\perp}}{x_{\parallel}} \right) \quad (3.14)$$

where g_3 is defined in Eq. (3.11). This shows us that the long range shape of the particle-particle correlation function has the shape of the electric potential of a quadrupole moment of a charge distribution, where f^2 is analogous to the magnitude of the quadrupole moment tensor b^2 . To push the analogy between the systems further, one can assume that the space permittivity is anisotropic, such that it would scale as $\epsilon_{\perp} = \epsilon_0 \sqrt{1 + b^2}$ while in the other direction it is constant $\epsilon_{\parallel} = \epsilon_0$. This would lead to a complete functional identification between the correlation function and the electric potential of the 4-charge system:

$$\phi = -\frac{b^2 q}{4\pi\epsilon_0\ell x_{\parallel}^3} g_3 \left(\sqrt{1 + b^2} \frac{x_{\perp}}{x_{\parallel}} \right) \quad (3.15)$$

Even though the origin of this analogy is not completely clear to us, it suggests a relation to the deformation of the picture of the ionic cloud, as it has been proposed in the work of Onsager [24, 85]. The identification of the correlation function and effective electrostatic

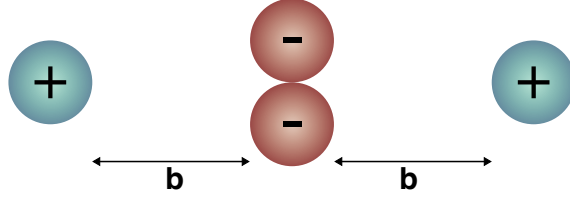


Figure 3.3: An illustration of the point charge configuration to which the long distance electric potential is analogous to the long range particle particle correlation function.

potential is no coincidence in equilibrium for the DH limit and further investigation might lead to interesting relations to the equilibrium case.

3.2 Time dependent correlations

As we saw in chapter 2, an algebraic relaxation of the transient was found in the long time regime of the conductivity. In this section we study the time dependent behavior of the correlations to further detail. This will shed light on the transient of macroscopic quantities of the system. In particular we focus on the spatial regime where the Debye length λ_D is small and diffusion length $\sqrt{\kappa T t}$ is large.

Eq. (2.26) can be solved exactly for an immediate switch on of the electric field, to give:

$$\tilde{c}_{++} = \frac{f^2 u^2 e^{-B\tau}}{2ABC\Delta} \left[B^2 \cosh(\sqrt{\Delta}\tau) + B\sqrt{\Delta} \sinh(\sqrt{\Delta}\tau) - 4Cs^2 \right] + \frac{1}{2BC} - \frac{1}{B} + 1, \quad (3.16)$$

$$\begin{aligned} \tilde{c}_{+-} = & \frac{fue^{-B\tau}}{2ABC\Delta} \left[B\sqrt{\Delta}fu \sinh(\sqrt{\Delta}\tau) (B - 2ifsu) + Bfu \cosh(\sqrt{\Delta}\tau) (\Delta - 2iBfsu) + 2iCs \right] \\ & + \frac{1}{2C} - \frac{ifsu}{BC}, \end{aligned} \quad (3.17)$$

where $A = 1 + s^2$; $B = 1 + 2s^2$; $C = f^2 u^2 + s^2 + 1$ and $\Delta = 1 - 4f^2 s^2 u^2$. The other terms satisfy: $\tilde{c}_{--} = \tilde{c}_{++}$ and $\tilde{c}_{-+} = \tilde{c}_{+-}^*$. At long times, the dominant term is the one that correspond to the smallest eigenvalue of the system. In this case, it corresponds to $B - \sqrt{\Delta}$. We can read it of the expressions in Eq. (3.16):

$$\tilde{c}_{++} = \frac{f^2 u^2 e^{-\tau(B-\sqrt{\Delta})}}{4AC\Delta} \left[B + \sqrt{\Delta} \right] + \frac{1}{2BC} - \frac{1}{B} + 1, \quad (3.18)$$

$$\begin{aligned} \tilde{c}_{+-} = & \frac{f^2 u^2 e^{-\tau(B-\sqrt{\Delta})}}{4AC\Delta} \left[\sqrt{\Delta}(B - 2ifsu) + (\Delta - 2iBfsu) \right] \\ & + \frac{1}{2C} - \frac{ifsu}{BC}. \end{aligned} \quad (3.19)$$

These correlation terms can be approximated in the long range regime, which translates to $s \rightarrow 0$ in non dimensionalised Fourier space. Again, we find that the behavior of all the

correlation terms is the same:

$$\tilde{c}_{\alpha,\beta} = \frac{f^2 s_{\parallel}^2}{2(s^2 + f^2 s_{\parallel}^2)} e^{-2\tau(s^2 + f^2 s_{\parallel}^2)} + \frac{s^2}{2(s^2 + f^2 s_{\parallel}^2)}, \quad (3.20)$$

where we replaced $u = \frac{s_{\parallel}}{s}$. One sees that when $\tau \rightarrow 0$, the correlation is $1/2$ which is the equilibrium correlation at large distances. When $\tau \rightarrow \infty$ one recovers the NESS result from the previous section. We can identify the exponential as the solution to the diffusion equation in Fourier space, which means that the transition between these two states follows a diffusive dynamics. The term $f^2 s_{\parallel}^2$ enhances the diffusion in the direction of the driving field. To see better the diffusion coefficient we revert to dimensional quantities $\tau s^2 = \frac{t\kappa T}{\lambda_D^2} k^2 \lambda_D^2 = tk^2 \kappa T$. The correlation spreads like a non isotropic diffusion with diffusion constants κT in the perpendicular directions and $\kappa T(1 + f^2)$ in the field direction.

We can invert the time dependent term back to real space. To do so, we start by examining a change of variables to the Fourier transform. In general, the correlation in real space satisfy:

$$c(x, \tau) = \frac{1}{(2\pi)^d} \int \tilde{c}(s, \tau) e^{-isx} ds. \quad (3.21)$$

Motivated by the shape of the correlation in Fourier space, we apply the following change of variables $\tilde{s} = \{s_{\parallel} \sqrt{\tau} \sqrt{1 + f^2}, s_j \sqrt{\tau}\}$ and $\tilde{x} = \left\{ \frac{x_{\parallel}}{\sqrt{\tau} \sqrt{1 + f^2}}, \frac{x_j}{\sqrt{\tau}} \right\}$, the index j runs for all the perpendicular axes to the external field. One gets the new variables:

$$c(x, \tau) = \frac{1}{(2\pi)^d \tau^{d/2} \sqrt{1 + f^2}} \int \tilde{c}(\tilde{s}, t) e^{-i\tilde{s}\tilde{x}} d\tilde{s}. \quad (3.22)$$

In the new \tilde{s} coordinates, Eq. (3.20) have the form:

$$c_s(\tilde{s}) = \frac{1}{2} + \frac{f^2}{2(1 + f^2)} \frac{(e^{-2\tilde{s}^2} - 1)}{\tilde{s}^2} \tilde{s}_{\parallel}^2. \quad (3.23)$$

Discarding the constant $\frac{1}{2}$ as it will give a delta function at the origin and substituting back into Eq. (3.22) we get:

$$c(x) = \frac{f^2}{2(2\pi)^d \tau^{d/2} (1 + f^2)^{3/2}} \int \frac{e^{-2\tilde{s}^2} - 1}{\tilde{s}^2} \tilde{s}_{\parallel}^2 e^{-i\tilde{s}\tilde{x}} d\tilde{s}. \quad (3.24)$$

We can replace \tilde{s}_{\parallel}^2 with a minus second derivative with respect to \tilde{x}_{\parallel} . By doing so, we are left with as radially symmetric Fourier transform:

$$c(x) = -\frac{f^2}{2(2\pi)^d \tau^{d/2} (1 + f^2)^{3/2}} \frac{\partial^2}{\partial \tilde{x}_{\parallel}^2} \left[\int \frac{e^{-2\tilde{s}^2} - 1}{\tilde{s}^2} e^{-i\tilde{s}\tilde{x}} d\tilde{s} \right]. \quad (3.25)$$

Using the radial symmetry, the integral is reduced the single integral:

$$c(x) = -\frac{f^2}{2(2\pi)^d \tau^{d/2} (1+f^2)^{3/2}} \frac{\partial^2}{\partial \tilde{x}_{\parallel}^2} \left[\frac{(2\pi)^{d/2}}{\tilde{x}^{d/2-1}} \int_0^{\infty} \frac{e^{-2\tilde{s}^2} - 1}{\tilde{s}^2} \tilde{s}^{d/2-1} J_{d/2-1}(\tilde{s}\tilde{x}) \tilde{s} d\tilde{s} \right]. \quad (3.26)$$

The integral is the Hankel transform of order $(\frac{d}{2} - 1)$ of the function $\frac{e^{-2\tilde{s}^2} - 1}{\tilde{s}^2} \tilde{s}^{d/2-1}$. It can be evaluated to get:

$$c(x) = -\frac{f^2}{8\pi^{d/2} \tau^{d/2} (1+f^2)^{3/2}} \frac{\partial^2}{\partial \tilde{x}_{\parallel}^2} \left[\frac{\Gamma_{d/2-1}\left(\frac{\tilde{x}^2}{8}\right)}{\tilde{x}^{d-2}} \right], \quad (3.27)$$

where $\Gamma_{d/2-1}$ is the (upper) incomplete gamma function of $d/2 - 1$. This shape of the correlation can be written as:

$$c(x) = \frac{1}{8\pi^{d/2}} \frac{1}{\tau^{d/2}} \frac{f^2}{(1+f^2)^{3/2}} \Phi\left(\frac{\mathbf{x}}{\sqrt{\tau}}\right). \quad (3.28)$$

The function Φ is anisotropic in space but presents diffusive scaling between the spatial and temporal coordinates. It's behavior can summed as:

$$\Phi(\mathbf{x}) \sim 2(f^2 + 1)^{d/2} \Gamma\left(\frac{d}{2}\right) \frac{(du^2 + f^2(u^2 - 1) - 1)}{(1 - f^2(u^2 - 1))^{\frac{d}{2}+1}} \frac{1}{x^d} \sim \frac{1}{x^d} \text{ when } x \rightarrow 0, \quad (3.29)$$

$$\Phi(\mathbf{x}) \sim \frac{u^2}{1 + f^2(1 - u^2)} \exp\left(-\frac{1 + f^2(1 - u^2)}{8(f^2 + 1)} x^2\right) \sim \exp(-x^2) \text{ when } x \rightarrow \infty, \quad (3.30)$$

where $u = \frac{z}{x}$. We can see that in the regime where $\frac{|x|}{\sqrt{\tau}} \ll 1$, namely, when the diffusion length scale is large compared to the region of interest, we recover the time independent NESS solution. In the opposite regime, where the diffusion length scale is small compared to region of interest, we find that the correlation decays exponentially fast, and the correlation elements are effectively zero as in equilibrium. Note that under the approximation we took, the Debye length scale was taken to zero. In Fig. 3.4 one can see the different regimes, at different time stamps, in rescaled and real axes. Eq. (3.27) is reduced, in three dimensions, to the following expression:

$$c(x) = -\frac{f^2}{8\pi\tau^{3/2} (1+f^2)^{3/2}} \frac{\partial^2}{\partial \tilde{x}_{\parallel}^2} \left[\frac{\text{erf}\left(\frac{\tilde{x}}{2\sqrt{2}}\right)}{\tilde{x}} \right]. \quad (3.31)$$

Together with the stationary result in Eq. (3.11) we get that the behavior of the correlation

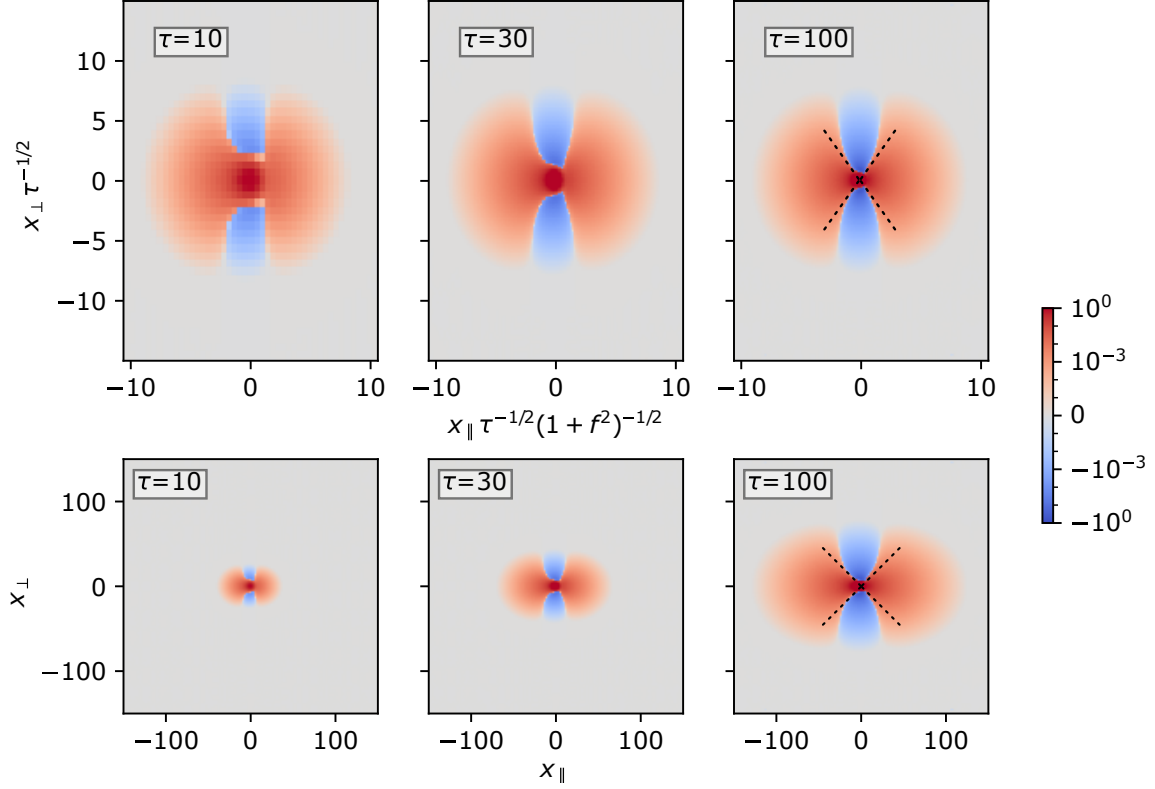


Figure 3.4: A time series of the correlation element rescaled by time $c_{-+}\tau^{3/2}$, along rescaled (upper row) and real (lower row) axes. The figure has been evaluated for $f = 1$. Near the center one can see the conical shape found in the NESS. Away from the center we find the exponentially small equilibrium value. In between we find the term corresponding to the second term in the r.h.s of Eq. (3.32). Its magnitude decays like $\tau^{-1/2}$ and so it is visible in the correlation even at large times. In the rightmost panels the angle predicted by Eq. (3.12) was added, it allows to appreciate visually the different regimes of behavior.

is of the form:

$$\begin{aligned}
 c(x, \tau) = & -\frac{f^2}{8\pi x_{\parallel}^3} g_3 \left(\sqrt{1+f^2} \frac{x_{\perp}}{x_{\parallel}} \right) \operatorname{erfc} \left[\sqrt{\frac{x_{\parallel}^2}{f^2+1} + x_{\perp}^2} \right] \\
 & - \frac{f^2 \exp \left[-\frac{x_{\parallel}^2}{f^2+1} + \frac{x_{\perp}^2}{8\tau} \right]}{8\sqrt{2}\pi^{3/2} \sqrt{(f^2+1)} \tau} \left(\frac{(f^2+1)x_{\perp}^2 + 2x_{\parallel}^2}{((f^2+1)x_{\perp}^2 + x_{\parallel}^2)^2} - \frac{x_{\parallel}^2}{4(f^2+1)\tau((f^2+1)x_{\perp}^2 + x_{\parallel}^2)} \right).
 \end{aligned} \tag{3.32}$$

This expression is reminiscent of the known solution to the diffusion equation under switching on a constant source term at the origin. What differentiates our case, is the fact that the diffusion coefficient is not isotropic and that the source located at the origin is the Laplacian of a Dirac delta function.

3.3 Equation for the long range correlations

Another way to derive the long-range behavior of the correlation elements is by approximating the Langevin equations, which results in a coarse grained equation for the correlation elements.

3.3.1 Coarse grained equation

Similarly to [74], we start by considering the Eq. (2.20) for the density of the species α in Fourier space, for the special case of binary monovalent electrolytes we get

$$\dot{\tilde{n}}_{\pm} = -\kappa T k^2 \tilde{n}_{\pm} \pm i\kappa q \mathbf{E} \cdot \mathbf{k} \tilde{n}_{\pm} - \kappa \bar{\rho} k^2 \sum_{\beta} \tilde{V}_{\pm\beta} \tilde{n}_{\beta} + \chi_{\pm}. \quad (3.33)$$

where χ is a Gaussian white noise with a correlation function that follows:

$$\langle \chi_{\alpha}(\mathbf{k}, t) \chi_{\beta}(\mathbf{k}', t') \rangle = 2(2\pi)^d \kappa T \bar{\rho} k^2 \delta_{\alpha\beta} \delta(\mathbf{k} + \mathbf{k}') \delta(t - t'). \quad (3.34)$$

Now we will consider the equations for the sum and difference variables, $U = \tilde{n}_{+} + \tilde{n}_{-}$ and $\Delta = \tilde{n}_{+} - \tilde{n}_{-}$, namely:

$$\dot{U} = -\kappa T k^2 U + i\kappa q \mathbf{E} \cdot \mathbf{k} \Delta + \sqrt{2} \chi_U. \quad (3.35)$$

$$\dot{\Delta} = -\kappa T k^2 \Delta + i\kappa q \mathbf{E} \cdot \mathbf{k} U - 2\kappa \bar{\rho} \frac{q^2}{\varepsilon} \Delta + \sqrt{2} \chi_{\Delta}. \quad (3.36)$$

In order to address the asymptotic long-distance behavior of a system, it is often useful to simplify the analysis by identifying certain regimes where the dynamics are dominated by particular physical processes. In the context of charge fluctuations, for example, it is known that the behavior is strongly influenced by the Debye screening mechanism at short length and time scales. However, when considering longer length and time scales, it is often possible to approximate the charge fluctuations with a quasi-stationary solution that captures the dominant features of the system. Note that when E is set to 0 the equation for U describes diffusion and the equation for Δ describes diffusion in the presence of screening, which flatten even the very slow modes (small wavenumber) after the Debye time.

Applying a field couples the equations, in particular, this coupling gives rise to a charge fluctuation that persists beyond the Debye time. Following this logic, we examine the behavior of Eqs. (3.36) in the regime where $\frac{\lambda_D^2}{\kappa T}$ and λ_D are small. Eq. (3.36) simplifies to:

$$2\kappa \bar{\rho} \frac{q^2}{\varepsilon} \Delta = i\kappa q \mathbf{E} \cdot \mathbf{k} U. \quad (3.37)$$

Note that the noise term is also of higher order in λ_D . Now we can use Eqs. (3.37, 3.35) to

write a closed equation for U :

$$\dot{U} = -\kappa T \left(k^2 + f^2 k_{\parallel}^2 \right) U + \sqrt{2} \chi_U. \quad (3.38)$$

where we denote the direction of the field as k_{\parallel} . We recall the definition $f = q\lambda_{\text{D}}E_0/T$. With Eq. (3.37,3.38) we can write an equivalent version of Eq. (2.24) that is valid only for large distances compared to the Debye length. As in Eq. (2.23), we have $\langle U(k, t)U(k', t) \rangle = (2\pi)^d \delta(k+k') C_{UU}(k, t)$, where $C_{UU}(k, t)$ is the Fourier transform of the correlation function in real space:

$$\dot{C}_{UU}(k, t) = -2\kappa T \left(k^2 + f^2 k_{\parallel}^2 \right) C_{UU}(k, t) + 4\kappa T \bar{\rho} k^2 \quad (3.39)$$

We can nondimensionlize the equation in the same way done in subsection 2.4 to get:

$$\dot{c}_{UU}(s, \tau) = -2 \left(s^2 + f^2 s_{\parallel}^2 \right) c_{UU}(s, \tau) + 4s^2. \quad (3.40)$$

We recall that $c_{UU} = \sum_{\alpha\beta} \tilde{c}_{\alpha\beta}$ so we need to solve for $c_{UU} = 4C_{sp}$, substituting this definition into Eq. (3.40) gives:

$$\dot{C}_{sp}(s, \tau) = -2 \left(s^2 + f^2 s_{\parallel}^2 \right) C_{sp}(s, \tau) + s^2, \quad (3.41)$$

with the initial condition $C_{sp}(s, 0) = \frac{1}{2}$. It is easy to see that the solution to this equation is given by Eq. (3.20). At this stage we can gain some insight into the relaxation rates of the conductivity corrections that we found in Eqs. (2.35,2.40,2.49).

3.3.2 Relaxation rates of the conductivity

Recalling the electrostatic correction in Eq. (2.29) we see that the integral depends on the term $\sum_{\alpha,\beta} z_{\alpha} [\tilde{c}_{\alpha\beta}(s, u, \tau, f) - \delta_{\alpha\beta}]$. This term is equivalent in a binary monovalent electrolyte, under the approximation we have taken, to $c_{U\Delta} = \langle U(s, t)\Delta(s', t) \rangle$. It is clear by expanding the expression:

$$\begin{aligned} \langle U(s, t)\Delta(s', t) \rangle &= \langle n_+(s, t)n_+(s', t) \rangle - \langle n_+(s, t)n_-(s', t) \rangle \\ &\quad + \langle n_-(s, t)n_+(s', t) \rangle - \langle n_-(s, t)n_-(s', t) \rangle. \end{aligned} \quad (3.42)$$

Similarly, for the hydrodynamic correction that is given in Eq. (2.30), we see that the integral depends on the term $\sum_{\alpha,\beta} z_{\alpha} z_{\beta} [\tilde{c}_{\alpha\beta}(s, u, \tau, f) - \delta_{\alpha\beta}]$. Under the same assumptions, this term is equivalent to $c_{\Delta\Delta} = \langle \Delta(t, s)\Delta(s', t) \rangle$. This tells us that the electrostatic correction depends on the correlation function between the mass and the charge fields while the hydrodynamic correction depends on the correlation function of the charge field with itself.

First, we see that the exponential decay, when going from NESS to equilibrium is manifested in Eq. (3.37) due to the fact that $f = 0$. This implies that $c_{U\Delta}$ is strictly zero and thus the relaxation of the correction as well.

Second, for the equilibrium to NESS process, we can rewrite Eq. (3.37) in a nondimensionalized form $\Delta = if s_{\parallel} U$. This formula can be used to write an equation for the correlation function between the mass field U and the charge field Δ , as well as the equation for the charge-charge correlation function:

$$\dot{c}_{U\Delta}(s, \tau) = -2 \left(s^2 + f^2 s_{\parallel}^2 \right) c_{U\Delta}(s, \tau) + if s_{\parallel} s^2 \quad (3.43)$$

$$\dot{c}_{\Delta\Delta}(s, \tau) = -2 \left(s^2 + f^2 s_{\parallel}^2 \right) c_{\Delta\Delta}(s, \tau) - f^2 s_{\parallel}^2 s^2, \quad (3.44)$$

with the initial condition $c_{U\Delta}(s, 0) = c_{\Delta\Delta}(s, 0) = 0$.

The time-dependent parts of the solutions of these two diffusion equations are of the form:

$$c_{U\Delta} = H(s\sqrt{\tau})s \quad \text{and} \quad c_{\Delta\Delta} = H(s\sqrt{\tau})s^2, \quad (3.45)$$

where H is some rapidly decreasing function. Note that we have kept only the scaling form of the expressions. Looking again at the original expressions in Eq. (2.17) we can see that the integral of the two corrections to the conductivity, each with the corresponding solution in Eq. (3.45) ($c_{U\Delta}$ for first term and $c_{\Delta\Delta}$ for the second) are:

$$I(\tau) \sim \int H(s\sqrt{\tau}) ds, \quad (3.46)$$

again, we kept only the scaling form of the expressions. In particular, the Oseen tensor and the electrostatic potential both scale as $\tilde{\mathcal{O}} \sim \tilde{V} \sim \frac{1}{s^2}$. By changing the integration variable we see the the integral scales like $I \sim \frac{1}{\tau^{d/2}}$. In $d = 3$ we find that this is the relaxation exponent, $-3/2$ we have found in Eqs. (2.40,2.49). In other words, the underlying diffusive nature of the system is responsible for the algebraic decay of the currents to their steady state values. We have shown that the algebraic decay is related to the large distance correlations, while the short range behavior is important to capture the details of the conductivity correction.

Chapter 4

Perspectives

Through chapter 2 and 3 of this manuscript we have addressed several questions about the dynamics and long range behavior of electrolyte systems from a theoretical point of view. We start this chapter with a brief summary of the results.

In chapter 2 the transient ionic correlations in an electrolyte were analyzed under the sudden switch on or off of an external electric field of arbitrary magnitude using linearized SDFT. It was observed that the correlations do not follow the same trajectory depending on whether the field is switched on or off. By employing the SDFT formalism, we obtained an exact expression for the total electric current, which relies on the two-point and three-point correlation functions. The electrostatic and hydrodynamic corrections were determined based on the ionic correlations. When the field is switched off, the hydrodynamic correction is absent, and the electrostatic correction decays exponentially. This rapid decay appeared to correspond to the decay of the odd part of the correlations. In contrast, the even part of the correlations, which did not contribute to the electrostatic correction, decayed at a slower rate. Conversely, when the field was switched on, both corrections exhibited algebraic relaxation towards their steady-state values, with the same rate of decay. In the linear response regime, an exponential relaxation was recovered upon switching on the field, indicating that the algebraic relaxation is a nonlinear effect.

In chapter 3 we have characterized the behavior of the particle-particle correlation functions in the long range regime, in the non equilibrium steady state and in the transient regime as the steady state is approached. At NESS, the correlation function has a conical shape, which differentiates the ionic system from systems with short-range interactions. The particle-particle correlations of both types of systems (short and long ranged interactions) are short ranged at equilibrium and long range at NESS. However the structure of the correlation is conical and not paraboloid [70]. Moreover, the spherical symmetry of the correlation is not recovered and the cone's angle reaches a finite value. Lastly we find that a self-similar universal shape for cuts along the x_{\parallel} axis. The universal shape accounts for any cut and external field.

There are still many questions about electrolyte systems, and we would like to discuss some of them which seems of particular interest here.

We have analyzed the response to the application of an external electric field, but to better

understand the dynamics of the system, it would be complementary to study its response to an oscillating external field. This question has been partially addressed by [74], but only under the assumption that the driving field changes on a timescale much larger than the Deybe time. We have seen that macroscopic quantities can depend on small scale features, for example the long range correlation function is insufficient to capture the details of the corrections to the conductivity. This suggests that going beyond the slow change limit of the driving field may give rise to interesting phenomena [71]. Moreover, the effects of confinement on ionic systems were studied and are of major interest especially in the context of soft biological matter [86, 87]. It is not clear whether the formalism presented in this work could provide further insight into these types of problems. In particular, in confinement to narrow channels, due to the effect of short-range repulsion between the ions.

Another direction is to better understand the effect of the interaction potential between the particles. In [70] short range interactions have been studied in the NESS, and in [63, 64] modified electrostatic potential has been studied to account for the short range repulsive interactions. First, it seems relevant to study the transient regime within these potentials, especially whether or not it has a profound effect on relaxation times. Second, the common point between these studies is that the interaction between the particles can always be factored as an interaction kernel G times a product of the species valences (i.e. $V_{\alpha\beta}(x) = z_{\alpha}z_{\beta}G(x)$). Since real particle-particle interactions do not respect such a factorization, it would be interesting to further investigate the consequences of such interaction potentials. Recent studies have started examining the robustness of this modification of the interaction potential [88].

Lastly, the relationship between diffusive systems with (and without) interacting particles and certain types of pink noise has received some attention [89, 90]. Since non-Gaussian noise appears in a wide range of physical systems, further investigation of these preliminary results seems of great interest. The findings of Ref. [90] relate the fractal noise to finite observation volumes where the fluctuations of charge and mass relax differently. This fact can be linked in a general sense to the relationship we have discussed between the relaxation of the conductivity and the underlying diffusive nature of the ionic fields.

Chapter 5

Appendix – Part I

5.1 Correlations

Here, we give the dimensionless correlations obtained by solving equation (2.26) when going from NESS to Equilibrium, and Equilibrium to NESS.

5.1.1 NESS to Equilibrium

The correlations are:

$$\tilde{c}_{++} = -\frac{1}{2A} - \frac{f^2 u^2 e^{-B\tau}}{2ABC} [B \sinh(\tau) + \cosh(\tau)], \quad (5.1)$$

$$\tilde{c}_{+-} = -\frac{f^2 s^2 u^2 e^{-2A\tau}}{2ABC} - \frac{f^2 u^2 e^{2\tau-2A\tau}}{2BC} - \frac{ifsu e^{\tau-2A\tau}}{BC} + \frac{1}{2A}, \quad (5.2)$$

where $A = 1 + s^2$; $B = 1 + 2s^2$ and $C = f^2 u^2 + s^2 + 1$. By symmetry, the other terms are $\tilde{c}_{--} = \tilde{c}_{++}$ and $\tilde{c}_{-+} = \tilde{c}_{+-}^*$.

5.1.2 Equilibrium to NESS

The correlations are:

$$\tilde{c}_{++} = \frac{f^2 u^2 e^{-B\tau}}{2ABC\Delta} \left[B^2 \cosh(\sqrt{\Delta}\tau) + B\sqrt{\Delta} \sinh(\sqrt{\Delta}\tau) - 4Cs^2 \right] + \frac{1}{2BC} - \frac{1}{B}, \quad (5.3)$$

$$\begin{aligned} \tilde{c}_{+-} = & \frac{fue^{-B\tau}}{2ABC\Delta} \left[B\sqrt{\Delta}fu \sinh(\sqrt{\Delta}\tau) (B - 2ifsu) + Bfu \cosh(\sqrt{\Delta}\tau) (\Delta - 2iBfsu) + 2iCs \right] \\ & + \frac{1}{2C} - \frac{ifsu}{BC}, \end{aligned} \quad (5.4)$$

where $A = 1 + s^2$; $B = 1 + 2s^2$; $C = f^2 u^2 + s^2 + 1$ and $\Delta = 1 - 4f^2 s^2 u^2$. The other terms are $\tilde{c}_{--} = \tilde{c}_{++}$ and $\tilde{c}_{-+} = \tilde{c}_{+-}^*$.

5.2 Derivation of the equation for the correlations

In this appendix we derive the equation for the evolution of the correlations, Eq. (2.24) (see Ref. [80], Sec. 4.4). We start from the stochastic equation for the density fluctuations,

Eq. (2.20), which we write with the Itô integral notation [58]:

$$d\tilde{n}(\mathbf{k}) = -R(\mathbf{k})A(\mathbf{k})\tilde{n}(\mathbf{k})dt + d\chi(\mathbf{k}). \quad (5.5)$$

We then differentiate the definition of the correlations, $(2\pi)^d\delta(\mathbf{k}+\mathbf{k}')\tilde{C}(\mathbf{k}, t) = \langle n(\mathbf{k}, t)n(\mathbf{k}', t)^\top \rangle$ (Eq. (2.23)), using the Itô formula [58]:

$$\begin{aligned} (2\pi)^d\delta(\mathbf{k} + \mathbf{k}')d\tilde{C}(\mathbf{k}, t) &= \langle d\tilde{n}(\mathbf{k}, t)\tilde{n}(\mathbf{k}', t)^\top + \tilde{n}(\mathbf{k}, t)d\tilde{n}(\mathbf{k}', t)^\top + d\chi(\mathbf{k})d\chi(\mathbf{k}')^\top \rangle \\ &= dt \left[-R(\mathbf{k})A(\mathbf{k})\langle \tilde{n}(\mathbf{k}, t)\tilde{n}(\mathbf{k}, t)^\top \rangle - \langle \tilde{n}(\mathbf{k}, t)\tilde{n}(\mathbf{k}, t)^\top \rangle A(\mathbf{k}')^\top R(\mathbf{k}')^\top \right] \\ &\quad - dt 2(2\pi)^d T\delta(\mathbf{k} + \mathbf{k}')R(\mathbf{k}). \end{aligned} \quad (5.6)$$

Using that $R(-\mathbf{k})^\top = R(\mathbf{k})$ and $A(-\mathbf{k})^\top = A(\mathbf{k})^*$, we obtain

$$d\tilde{C}(\mathbf{k}) = [-R(\mathbf{k})A(\mathbf{k})C(\mathbf{k}) - C(\mathbf{k})A(\mathbf{k})^*R(\mathbf{k}) + 2TR(\mathbf{k})] dt, \quad (5.7)$$

which recovers Eq. (2.24).

5.3 Regularity of the integrands from Equilibrium to NESS

The integrands of the electrostatic and hydrodynamic corrections, Eqs. (2.36, 2.47), seem to be singular when $1 - 4f^2s^2u^2$ approaches zero. However, they are continuous and their limits are:

$$\begin{aligned} y &= \frac{2f^3u^4e^{-\tau\left(\frac{1}{2f^2u^2}+1\right)}}{(2f^2u^2+1)^3(4f^2u^2+1)} \\ &\quad \times \left[(2f^2\tau u^2 + \tau)^2 + (8f^2u^2 + 2)e^{\tau\left(\frac{\tau}{2f^2u^2}+1\right)} - 8f^2u^2 + 4\tau(2f^4u^4 + f^2u^2) - 2 \right], \end{aligned} \quad (5.8)$$

$$\begin{aligned} h &= -\frac{4f^2u^2(u^2-1)}{(2f^2u^2+1)^3(4f^2u^2+1)} \left[f^2u^2e^{\tau\left(-\frac{1}{2f^2u^2}-1\right)} \left((2f^2\tau u^2 + \tau)^2 - 2\tau(2f^2u^2+1) - 4f^2u^2 \right) \right. \\ &\quad \left. - 2(8f^6u^6 + 10f^4u^4 + 6f^2u^2 + 1) \right]. \end{aligned} \quad (5.9)$$

Part II

Dense flow of granular matter

Chapter 6

Introduction to granular media

Soft matter is a category of materials composed of basic elements that are significantly larger than atoms or molecules, but still much smaller than the dimension of the global system. Examples of soft matter include liquid crystals, colloids, foams, gels, pastes, emulsions, slurries, cellular aggregates, polymers, and granular media. The elementary building blocks, such as bubbles, grains, or cells, have a size that introduce a new and intermediate typical length scale, known as the mesoscale, which is responsible for many specific properties. These materials are easily deformed, dissipative, out of equilibrium, nonlinear, affected by gravity, non-ergodic, and can exhibit yield stress, among other properties. Soft matter is clearly distinct and does not fall into the categories of simple fluids or elastic materials, and new theoretical frameworks are needed to properly describe this class of materials. Even today, understanding soft matter remains a challenge for researchers.

Granular materials represent a class of materials consisting of a large number of macroscopic solid particles, called grains, that have a range of sizes and shapes and interact primarily through inelastic collisions and friction. Specifically, grains have dimensions larger than 0.1 mm. Below this threshold, Van der Waals forces must be considered, leading to the classification of such materials as powders formed from cohesive particles. In the case of dry particles, capillary forces can be discarded and only frictional and repulsive contact forces come into play. For particles with dimensions smaller than 1 μm , called colloids, thermal fluctuations become important.

Grain-based materials have a wide range of applications in a variety of industries, including construction, mining, agri-food, pharmaceutical, and petrochemical. In these areas, overcoming the challenges of storing, transporting and handling granular materials is of great importance. In addition, granular materials play a key role in various geophysical phenomena such as landslides, avalanches, soil liquefaction, and cliff destabilization.

At first glance, dry granular media may appear simple and straightforward, given that these are systems that have been known for centuries, consisting of a fixed number of macroscopic particles driven by gravity. Each grain obeys the laws of classical mechanics and interacts through what might be perceived as “simple” frictional collisions. Furthermore, it might seem that this type of system could be completely characterized by a small number of parameters: gravitational acceleration g , grain density ρ , grain diameter d , and friction between grains μ .

However, despite this apparent simplicity, accurately predicting the collective motion of grains within a large assembly proves to be a complex task. Even when considering the most idealized granular system of spherical beads. This complexity manifests itself in many counterintuitive phenomena in granular media, such as i) The medium can dramatically change its behavior based on mechanical constraints, behaving like a solid, liquid, or gas [91]. ii) Inhomogeneous force propagation along chains, leading to the Janssen effect [92,93]. iii) The presence of shear banding similar to that seen in foams [94,95]. iv) Segregation phenomena such as the Brazil nut effect [96]. v) Jamming [97,98] and Reynolds dilatancy [99].

Despite several decades of intensive research, some of the mechanisms underlying dense granular flows remain largely unresolved. A universal framework to describe the numerous configurations and observations studied in the laboratory is still lacking [100]. Most models remain semi-empirical and are not supported by strong microscopic justifications [101–104]. The global flow properties are usually described by the popular $\mu(I)$ rheology. This approach consists of two empirical relations between the macroscopic friction coefficient μ (defined as the ratio of shear stress to pressure) or volume fraction ϕ on one hand, with the inertial number:

$$I = \dot{\gamma}d\sqrt{\frac{\rho_p}{P}}, \quad (6.1)$$

on the other hand. I involves the shear rate $\dot{\gamma}$, the grain size d , the mass density $\rho_p \sim m/d^3$ of the grains (or their individual mass m) and the pressure P [91, 101]. Essentially, in this Amontons-Coulomb-like description, a granular layer starts to flow when the applied shear stress exceeds a critical frictional stress $\mu_c P$. Nevertheless, this description fails to properly rationalize some important observable features, such as the presence of a metastable region [105, 106] and the layer thickness dependence of the angle at which the flow stops [107–110]. In the last decades, it has been shown that non-local/cooperative effects are essential to properly describe dense granular flows [111–118].

6.1 Flow regimes

Classical fluids are well described by the Navier-Stokes equations, but no constitutive law can reproduce the diversity of behavior observed in dry granular materials. This difficulty arises from fundamental properties of granular materials such as negligible thermal fluctuations and highly dissipative interactions. As a result, granular flows are often classified into three different regimes [100, 119]: A dense quasi-static regime in which deformations are very slow and the particles interact by frictional contacts; a gaseous regime in which the flow is very fast and dilute and the particles interact by collision; and an intermediate liquid regime in which the material is dense but still flows like a liquid and the particles interact by both collision and friction. See Fig. 6.1. These regimes can of course co-exist, as presented in the figure.

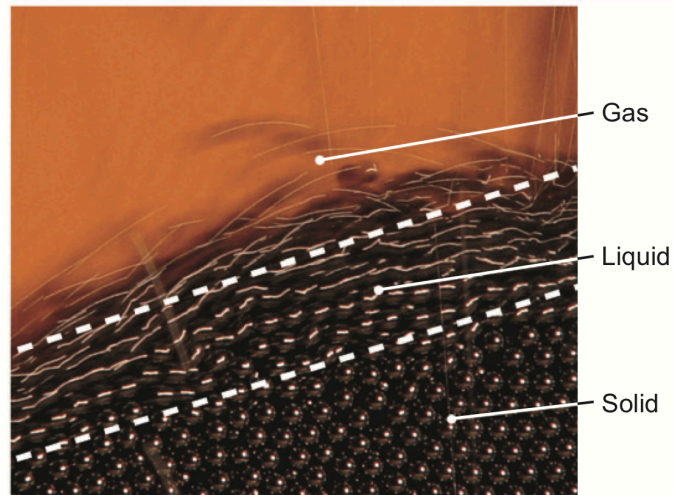


Figure 6.1: An illustration of the quasi-static, liquid, and gaseous flow regimes obtained by pouring steel beads on a pile. A solid-like region under the pile in which grains do not move or creep very slowly, a liquid region in which a dense layer flows, and a gaseous region in which the beads bounce in all directions creating a dilute chaotic medium. The picture was taken from [120].

6.2 Friction in granular media

In granular media, friction occurs naturally during particle-particle and particle-boundary contact and is therefore a critical factor in understanding granular media behavior. However, frictional phenomena can be complex and poorly understood, even beyond the granular media domain. This is a significant barrier to a comprehensive description of granular materials.

Studies have demonstrated the need to account for rolling friction in numerical simulations to accurately reproduce experimental observations of granular systems [121]. In addition, rolling friction plays a critical role in the packing structure and dynamics of granular media [122, 123]. Simulations reveal extensive regions of rotating grains, indicating the need to include rotational motion, and hence rotational friction, in modeling efforts.

Contrary to the behavior of Newtonian fluids, a container filled with granular material does not maintain a horizontal free surface (perpendicular to gravity) while it is gradually tilted. No significant change occurs until the slope reaches a critical angle. At this point, an avalanche is inevitably induced, resulting in a reduced slope. Similarly, when a granular pile is constructed, the slope of the pile cannot exceed a maximum threshold angle, beyond which avalanches are invariably triggered. Interestingly, the slope seems to remain constant, at least approximately, regardless of the size of the heap. This curious observation is widely believed to be directly related to the friction between individual grains. This is one way to characterize the effective coefficient of friction of the media with the angle of repose:

$$\mu = \tan(\theta), \quad (6.2)$$

where θ is the slope angle of the heap. Unfortunately (or maybe fortunately), even this characterization is insufficient, since approaching this angle from the static direction, namely the maximum angle that does not initiate flow (commonly called the critical angle of repose θ_c), gives a larger angle than approaching it from the dynamic direction, meaning the minimum angle at which flow stops (usually referred to as the angle of rest θ_r). In fact, hysteresis is an important feature of the solid-liquid transition in granular materials [124, 125].

6.3 Athermal system

Grains, due to their macroscopic size, are unaffected by thermal energy. Compared to their gravitational potential energy, the thermal energy is negligible. To see this, we can make an order of magnitude estimation for the two energies:

A 1 mm grain with a density of 10^3 Kg/m^3 (\lesssim density of most rocks) at room temperature, $E_{thermal} \sim k_b T \sim 10^{-21} \text{ J}$. On the other hand, the energy needed to elevate a grain on top of an adjacent grain is $E_{gravity} \sim \rho d^3 g d \sim 10^{-8} \text{ J}$, which is a difference of 13 orders of magnitude. The critical size for thermal effects is given by $d^* \sim (k_b T / \rho g)^{1/4} \sim 10^{-6} \text{ m}$. This is, in fact the typical size of a colloidal particle (1 μm).

Therefore, unlike molecules, grains do not undergo Brownian motion due to their significant inertia, resulting in granular systems that are locked into a singular configuration unless externally perturbed. These systems are called athermal systems and are inherently out of equilibrium. This distinguishes granular materials from other soft matter materials.

One might be tempted to assume that since temperature does not play a significant role in granular materials, there would be no fluctuations. In fact, the opposite is true. Since temperature cannot relax inhomogeneities, granular materials can exist in states with large local variations. Granular media exhibit pronounced mechanical fluctuations, suggesting that statistical approaches could help predict their emergent properties [126, 127]. However, established statistical mechanics, based primarily on the concept of temperature, may not be applicable here. Edwards proposed replacing the energy function with a volume function, allowing the probability of a state to be defined solely by particle positions [128]. This introduced the notion of compactivity, a temperature-like variable that measures the proximity of the system to its densest state. However, this doesn't account for force and torque balances in the presence of friction, which later led to the introduction of another temperature-like variable corresponding to stress [129] (angoricity).

Recent research [130] suggests that angoricity depends on the loading protocol, implying its inadequacy as a state variable. Therefore, yet another temperature analog has been introduced that is independent of the loading protocol. Further studies have also found conditions under which the Edwards conjecture holds, providing new perspectives on granular systems [131]. In addition, a granular equivalent of the thermodynamic zeroth law has been proposed [132].

Extending the scope to granular flows, collisions between grains become crucial. Here, the collision rate emerges as a key descriptor. The “granular temperature”, derived from velocity fluctuations, characterizes the collision rate and provides insight into granular systems that behave like gases [133, 134]. This concept of granular temperature is used to describe dense granular layers flowing down an inclined plane.

6.4 Jamming transition

The jamming transition represents a change in the state of athermal media from a fluid to an amorphous, solid-like state. Observations of this transition have been documented in a variety of soft materials, including granular materials, colloidal or granular suspensions, foams, and cellular aggregates [135–138]. When a threshold density ϕ_J , is exceeded, the material transitions into a metastable and disordered state and refrains from evolving to a slightly denser crystalline form. Reverting the material to its liquid state requires the application of significant shear stress or a reduction in density. Thus, jamming suggested to be an athermal version of the glass transition. Thinking of the jamming transition as a glass transition of a liquid in the limit case of hard core interaction potential [139, 140] is a useful analogy that allows us to draw ideas from the the glass domain. This perspective gained prominence due to the work of Liu and Nagel [141], even though later it was shown to be overly simplified [142].

The distinction of glass and jamming transitions have been the subject of considerable attention [142–144]. More specifically, the distance from equilibrium, the origin of rigidity and timescales. Identifying the specific transition a system undergoes is far from straightforward due to: the proximity of their density thresholds (ϕ_G and ϕ_J), the technical complexity of the measurement and the sensitivity to parameters, such as particle morphology, dispersity, and friction. Nevertheless, it is important to emphasize that despite their apparent similarities in macroscopic flow behavior, these transitions manifest on different timescales and under different stress conditions [144].

Focusing on the jamming transition, It is widely accepted that for monodisperse spherical grains, the transition typically occurs at $\phi_J \simeq 0.64$. From a theoretical point of view, defining the jammed states is not straightforward, since there are jammed configurations with varying values of ϕ in the phase space. A common definition that is well posed¹ is the “Maximally random jamming” (MRJ), the least ordered jammed state. Evaluation of the MRJ state suggests that it is manifested at a density of $\phi_{MRJ} \simeq 0.637$ [145].

A packing is said to be “jammed” when particles and their nearest neighbors establish contacts that give mechanical stability to the assembly. In other words, the total force and torque are zero for each grain [146]. Alternatively to the description in terms of volume fraction, it is common to evaluate the mean contact number, Z , to characterize

¹Apparently the notion of “random close parking” presents ambiguity in its mathematical definition [145].

the transition. The MRJ state is isostatic, which means that first, all degrees of freedom are confined by contacts, and second, the number of contacts is minimal [145]. From these considerations, the mean contact number Z_{iso} at which jamming occurs can be identified. Depending on the dimension of the system D , $Z_{\text{iso}} = 2D$ for a collection of frictionless spheres [147].

Up to this point, our discussion of jamming has (mostly) revolved around frictionless assemblies. Incorporating friction naturally increases the mechanical stability of system. In the extreme case of infinite friction, the degrees of freedom are reduced to $Z_{\text{iso}} = D + 1$ [145, 147]. Another fundamental difference is the well-known Reynolds dilatancy [148], which is directly related to the shearing of a jammed assembly. In frictionless assemblies, no dilatancy is observed, thus eliminating shear jamming [125, 149].

6.5 $\mu(I)$ Rheology

Upon the motion of granular media, a variety of regimes exist due to dramatic changes in flow characteristics. In the absence of a theoretical framework for granular media, dimensional analysis provides a decent starting point. In this context, the inertial number, I , allows a simple dimensional analysis to classify these different regimes. This dimensionless number is derived from the ratio of two different time scales. It compares the macroscopic time scale, which is related to the plastic deformation of the material and defined by the mean shear rate, $t_{\text{macro}} = 1/\dot{\gamma}$, with the microscopic time scale $t_{\text{micro}} = d/\sqrt{P/\rho_p}$, which is defined as the time taken for a grain to pass through a d -sized gap under pressure P . The ratio between these time scales, gives:

$$I = \frac{t_{\text{micro}}}{t_{\text{macro}}} = \frac{|\dot{\gamma}| d}{\sqrt{P/\rho_p}}. \quad (6.3)$$

The inertial number thus allows us to distinguish between the quasi-static, dense and dilute regimes, reflecting the solid, liquid and gaseous states, respectively [91].

For quasi-static flows, characterized by extremely small values of $I \lesssim 10^{-3}$, the grain flow rate is negligible compared to microscopic grain rearrangements. In this regime non-local effects are observed [103].

In contrast, as I increases, $I \gtrsim 1$, the flow regime becomes fast and dilute, with grains interacting primarily by inelastic collisions. This regime has led to the development of modified kinetic theories, inspired by molecular gases, to adequately describe these flow types [150, 151]. Between these extremes, one can observe the dense/inertial flow regime. Considered “dense” due to a volume fraction slightly less than the jammed packing, $\phi \simeq 0.5$, the grains in this regime interact through both collisions and sustained contacts, courtesy of friction. Typical granular flows observed in natural scenarios – landslides, avalanches on sand dunes, or grains descending in a hopper – all correspond to this dense regime. Hydrodynamic-like approaches and the $\mu(I)$ rheology are often used to describe

this intermediate state, although it is poorly understood at the grain scale.

A challenge in understanding granular materials is to define the rheology of these systems, i.e., to predict the behavior of the material under mechanical constraints. The $\mu(I)$ rheology is an accepted empirical model suitable for describing dense granular flows [101]. The granular fluid behavior is governed by the macroscopic friction coefficient (the macroscopic effective friction coefficient of the media, which is different from the microscopic friction coefficient between particles) μ and the volume fraction ϕ . Both depend exclusively on the inertial number I . The constitutive relations for the shear stress, τ , and the volume fraction, ϕ , are expressed as follows:

$$\tau = \mu(I)P \quad ; \quad \phi = \phi(I). \quad (6.4)$$

Usually the empirical expression for the effective friction $\mu(I)$, which is used to fit experiments is:

$$\mu(I) = \mu_s + \frac{\mu_2 - \mu_s}{\frac{I_0}{I} + 1}, \quad (6.5)$$

where μ_s, μ_2 and I_0 are parameters of the model. The $\mu(I)$ rheology is of course a local theory, since shear rate and pressure are local quantities. This means that at small values of I , as the system approaches a jammed state, we expect a deviation from such a theory because, as we saw earlier, long-range correlations appear in such assemblies that require nonlocal behavior. A simple experiment to observe this nonlocal behavior is to tilt an inclined plane with a layer of thickness h of granular material. It is observed that the angle at which the flow starts changes with the thickness of the layer h [107]. See Fig. 6.2.

6.6 Bagnold flow profile

When observing the flow of a dense granular layer over an inclined surface, the velocity profile typically follows $v(z) \sim h^{3/2}$, a profile famously known as the Bagnold profile [100, 152, 153].

Derived from Bagnold's postulates on the interactions of flowing grains, one can extract the structure of the velocity profile. It is generally accepted that granular media start to flow beyond a minimum critical angle θ_c . Therefore, it seems logical to propose a law that correlates the flow rate J with the angle of inclination θ as $J \propto (\theta - \theta_c)^m$, [154], where experimentally $m = 1/2$ has been observed [154]. For comparison, in the case of a Newtonian fluid with thickness h , density ρ , and viscosity η flowing down an inclined surface at an angle θ relative to the horizontal, the known rate is $J = \frac{\rho g h^3}{3\eta} \sin(\theta)$.

In simple terms, a regular fluid has a zero critical angle and an exponent $m = 1$. It is important to note that in fluids, the velocity of Brownian particles significantly exceeds the mean velocity of the flow, and the viscosity η captures all the details of dissipation. Conversely, in granular flows, the instantaneous velocity of the grains is equal to the mean

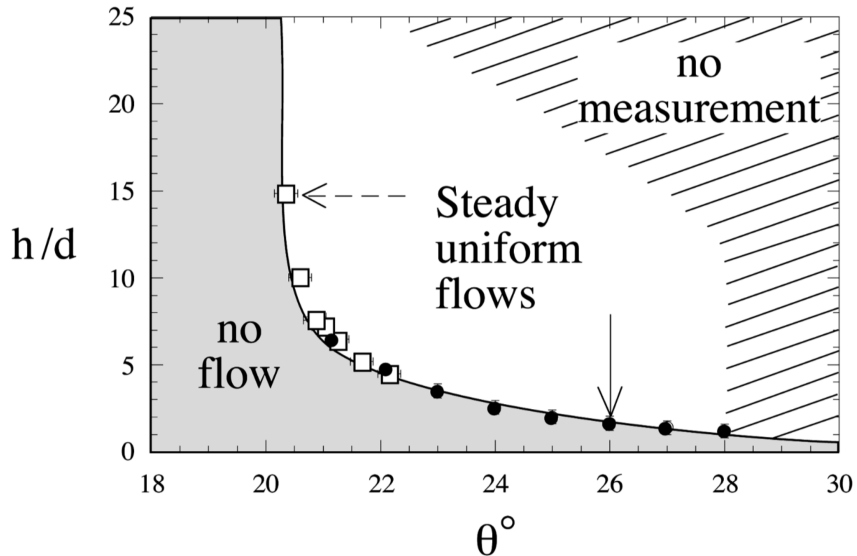


Figure 6.2: Flow of granular matter over a rough inclined plane, controlled by the two parameters, slope angle and layer thickness $(\theta, h/d)$. The figure shows regions in the parameter space where steady uniform flows are established. The measurements show a clear dependence of the stop angle on the layer thickness. The figure is taken from [107].

velocity of the flow. In 1954, Bagnold proposed that in an inertial granular flow, the shear stress is proportional to the square of the strain rate [155]. This proposition can be justified by visualizing the flow as a series of layers, where collisions between two successive layers are nearly tangential, which shows that: the collision rate between particles increases proportionally to ∇v and that the momentum loss after a collision is also proportional to ∇v .

The above considerations suggest that the dissipation resulting from the collisions is proportional to $(\nabla v)^2$. This form of dissipation should counterbalance the kinetic energy gained by descending the inclined plane.

$$\alpha(\nabla v)^2 = \rho g(h - z)(\sin(\theta) - \mu_c \cos(\theta)) \quad (6.6)$$

Here, $\mu_c = \tan(\theta_c)$ is the friction coefficient of a granular layer sliding over an adjacent one, and z is the downward direction in line with the gravitational force, with α being the combined constant of proportionality resulting from the two assumptions about collision rate and momentum dissipation. Assuming that ρ and μ vary minimally with velocity, the Bagnold velocity profile can be derived by first order expansion around $(\theta - \theta_c)$ and integration considering the boundary condition $v(0) = 0$ one gets:

$$v(z) = \frac{2}{3} \sqrt{\frac{\rho g}{\alpha \cos(\theta_c)}} h^{3/2} \left(1 - \left(1 - \frac{z}{h} \right)^{3/2} \right) (\theta - \theta_c)^{1/2}. \quad (6.7)$$

While the exponent governing the depth dependence (3/2) agrees with simulations and

experiments, the exponent $m = \frac{1}{2}$, which controls the angle, does not align with the findings from simulations and experiments. In Chapter 7, we will try to understand the origin on this exponent m , and what is missing in the theory to correct it.

Chapter 7

Microscopic picture of the $\mu(I)$ rheology for dense granular flows on inclined planes

This chapter is for the most part an extraction from [10]. All the numerical results were obtained by D. Dumont (Mons University).

In this chapter, using a combination of Discrete-Element-Method (DEM) simulations and a model based on microscopic arguments, we address the rheology of dense granular matter from the canonical setting of a layer flowing down an inclined plane. Therein, the inclination angle θ and the layer thickness H are the two external control parameters, see an illustration for a experimentally realizable set up in Fig. 7.1. Previous experimental and numerical studies have shown that the local average velocity profile of a thick granular layer flowing over an inclined plane exhibits a so-called Bagnold profile [100, 152, 153], namely:

$$\langle v(z, t) - v(0, t) \rangle \sim H^{3/2} - (H - z)^{3/2}, \quad (7.1)$$

where $v(z, t)$ is the local velocity field along the flow direction, at normal coordinate z and time t . Besides, it has been suggested that nonlocal cooperative effects are essential to describe the layer-thickness dependence of the stop angle [117, 118], that is to say the smallest angle for which a stationary flow is observed. We will see here that the mechanical noise related to grain-grain collisions determines an effective temperature. This concept coupled to the formation of clusters appears to be a fundamental issue to derive a model for granular flow based on the hard sphere fluid limit. The proposed model is able to predict the size of dynamic clusters, the Bagnold velocity profile as well as the two empirical relations, $\mu(I)$ and $\phi(I)$, commonly used to fit experimental and numerical data [91, 101]. The numerical simulations were performed with the software LIGGGHTS [156]. The system consists in a layer of identical grains, with diameter $d = 1$ mm, mass $m = \frac{4}{3}\pi\rho_p d^3/8$ and elastic modulus, $E = 1$ MPa, placed on an inclined plane with an inclination angle θ (see Fig. 7.2a). The interactions between grains are described through a Hertz-Mindlin model and a restitution coefficient equal to 0.5. We focus here on thick-enough layers, in order to avoid the thickness dependence of the stop angle observed for thin layers [107–110]. The mechanical properties of the simulated grains are set to be exactly the same as in our

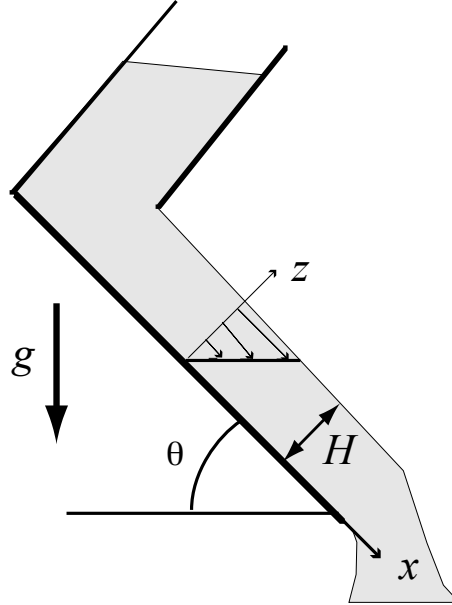


Figure 7.1: An illustration of a realizable set up of the experiment simulated by the DEM. Flow of granular material on a rough inclined plane with an angle θ . The upper channel is the reservoir of grains, which allows to observe the steady state flow. The illustration was adapted from [100].

previous study [118], and correspond to glass beads [107]. In particular, the microscopic coefficients μ_s and μ_r of sliding and rolling frictions are set to 0.5 and 0.01, respectively. In addition, frictionless grains (i.e., $\mu_s = \mu_r = 0$) are also simulated. The influence of the microscopic friction has also been studied. The substrate is made of immobile grains to mimic the glued grains in inclined-plane experiments. We impose periodic boundary conditions in the x and y directions to get rid of side-wall effects [157]. The size of the base has been carefully chosen in order to be large enough to avoid autocorrelations due to periodicity. We stress that similar set-ups have already been reported [105, 152, 153].

Before the inclination of the plane, the layer has an initial vertical thickness H_i ranging between $10d$ and $60d$, with a base of $20d \times 20d$ in the horizontal plane. The plane is subsequently inclined briefly at 30° to initiate the flow. Subsequently, the inclination is fixed at the desired angle θ , ranging between 20° and 40° . For each value of H_i and θ , the actual layer thickness H along z , and the mean volume fraction ϕ of the whole layer (averaged over at least 10 time steps in the steady state) are measured. The average local velocity profiles $\langle v(z, t) \rangle$ and the inertial number I are also computed. As a remark, we have the relation $\dot{\gamma}(z) = d\langle v(z, t) \rangle / dz$. The averages $\langle \rangle$ are performed over time and realizations, at fixed z .

7.1 Simulation of the inclined plane

In agreement with previous works [100, 105, 152, 153], we observe that: i) there is a critical stress to induce flow for dense granular layers, corresponding to a macroscopic friction

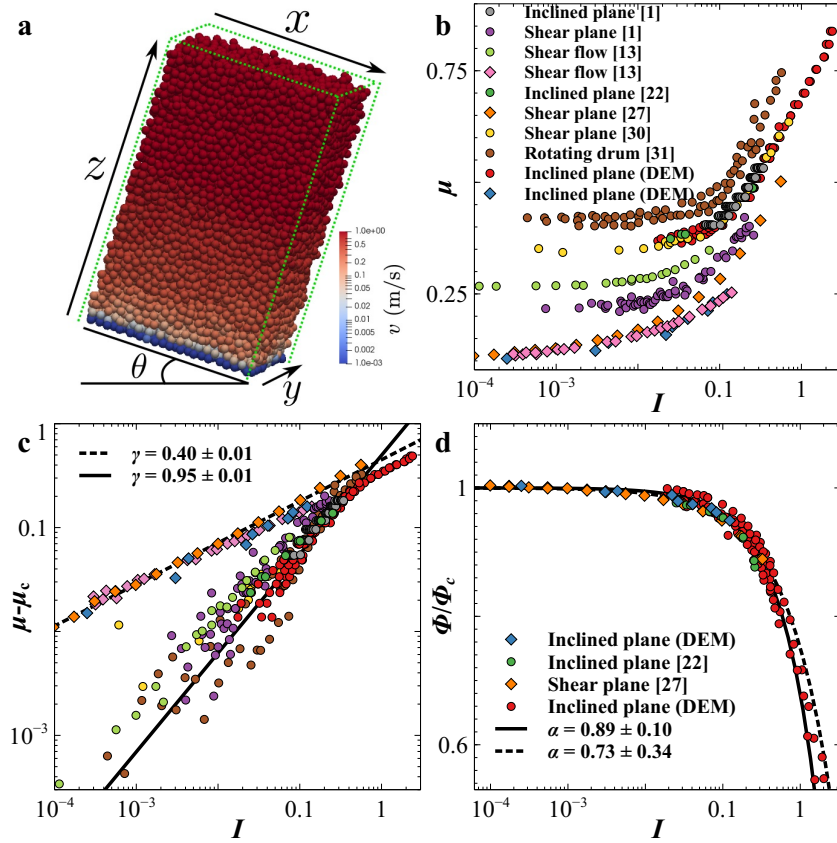


Figure 7.2: a) Typical snapshot of a DEM simulation, with initial layer thickness $H_i = 30d$ and inclination angle $\theta = 24^\circ$. The color code indicates the velocity $v(z, t)$. b) Macroscopic friction coefficient μ as a function of inertial number $I = \dot{\gamma}d\sqrt{\rho_p/P}$ for frictionless (diamonds) and frictional (circles) grains, as well as various inclination angles θ , initial layer thicknesses H_i , and various setup configurations [100, 111, 149, 152, 158, 159]. c) Difference $\mu - \mu_c$ in friction coefficient as a function of inertial number I , where $\mu_c = \mu(I \rightarrow 0)$, for the same data as in the previous panel. The solid and dashed lines correspond to fit with $\mu - \mu_c \sim I^\gamma$, the values of γ are provided in legend. d) Ratio of volume fraction ϕ/ϕ_c as a function of inertial number I for frictionless (diamonds, $\phi_c \simeq 0.64$) and frictional (circles, $\phi_c \simeq 0.6$) grains. Data from [149, 152] are added for comparison. The solid and dashed lines correspond to fit with $\phi/\phi_c = 1 - aI^\alpha$, the values of α are provided in legend.

coefficient $0.2 \leq \mu_c \leq 0.4$ for frictional grains, and 0.1 for frictionless grains (Fig. 7.2b); ii) the local average velocity profile is well described by a Bagnold profile; iii) the volume fraction ϕ and the inertial number I remain mostly constant throughout the layer, for all the studied inclination angles. As proposed in several studies [91, 160, 161], dimensional analysis shows that only one dimensionless parameter is required to describe granular flows, the inertial number I (besides the microscopic friction coefficient). The flow properties are characterized through the frictional, $\mu = \mu(I)$, and the dilatancy, $\phi = \phi(I)$ laws. The macroscopic friction coefficient μ is determined by the shear to normal stress ratio [91, 101, 160]. For the inclined-plane geometry considered here, both the macroscopic friction coefficient and the pressure are prescribed through the inclination θ of the plane and the height H of the flowing layer [160]. In a continuum-limit approximation, the effective friction coefficient for this setup is thus fixed to a constant value, $\mu = \tan(\theta) \simeq \theta$ for the range of inclination angles of interest. From dimensional analysis and since μ does not depend on z/d , we can conclude that I and ϕ are constant throughout the layer and fully determined by the inclination angle θ and the microscopic friction coefficient.

As previously shown, Fig. 7.2c confirms that $\mu(I)$ is well described by $\mu - \mu_c \sim I^\gamma$, with $\gamma = 0.40 \pm 0.01$ for frictionless grains [111, 149]. For frictional grains, $\gamma = 0.95 \pm 0.01$ for moderate inclination angles ($I \lesssim 0.1$) in agreement with previous observations [100, 152, 158, 159]. It should be noted that for large inclination angles, we observe a change of the exponent that becomes close to the value of frictionless systems $\gamma = 0.4$. The exponent for frictional grains does not depend on the (finite) values of the microscopic friction coefficients, thus indicating the singularity of the frictionless limit. In contrast, μ_c depends on the microscopic friction coefficients, but even for frictionless assemblies a non-zero value close to 0.1 is observed [110, 149]. The exact origin of this residual macroscopic friction remains unclear, but should be related to the steric constraints associated with granular topography [162].

The dilatancy laws obtained from the DEM simulations are shown in Fig. 7.2d and compared to data from the literature [120, 160, 163]. For all these combined data, the evolution of the packing fraction with I can be empirically described by the relation $\phi_c - \phi \sim I^\alpha$, where $\phi_c = \phi(I \rightarrow 0)$ is the volume fraction at kinetic arrest, and with $\alpha = 0.89 \pm 0.1$ and 0.73 ± 0.34 , for frictional and frictionless grains, respectively. Note that for frictionless grains, another functional form was proposed [149]: $1/\phi - 1/\phi_c \sim I^{0.4}$ but remains valid only for very small inertial numbers, namely $I \lesssim 10^{-2}$.

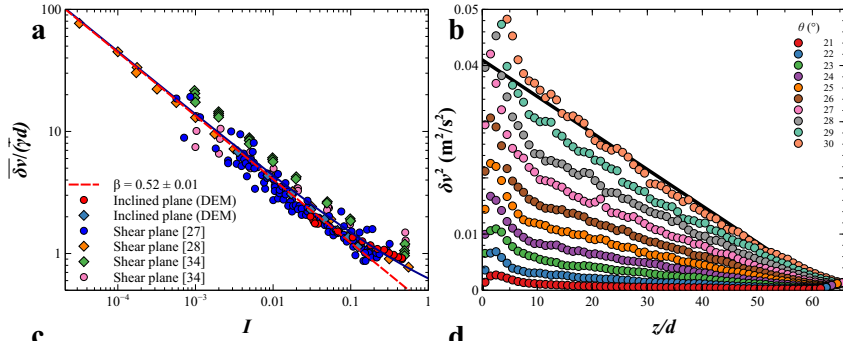


Figure 7.3: a) Thickness-averaged standard deviation $\overline{\delta v}$ of the velocity field normalized by a typical shear velocity $\bar{\gamma}d$, as a function of the inertial number I , for frictionless (diamonds) and frictional (circles) grains. Results from previous works [149, 160, 164] are also shown for comparison. The dashed line correspond to fit with $\delta v/\bar{\gamma} \sim I^{-\beta}$, the value of β is provided in legend (the fit is limited to small I 's values, $I < 0.05$). The solid line is a guide for the eyes and corresponds to $a(1 + b/I^{0.52})$ with $a=0.25$ and $b=1.5$. b) Local variance $\delta v^2(z) = \langle |v(z, t) - \langle v(z, t) \rangle|^2 \rangle$ of the velocity field $v(z, t)$, as a function of rescaled normal coordinate z/d , for a layer of frictional grains initially characterized by $H_i = 60d$ and various inclination angles θ as indicated. An affine solid line is added as a guide for the eye.

7.2 Theoretical analysis

We investigate the microscopic origin of these laws. As proposed by several authors, the velocity fluctuations and the diffusion coefficient of the grains are strong indicators of their dynamics [164, 165].

A dense granular flow is characterized by rapid collisions involving sudden changes of the velocity direction and renewal of the contact network. Assuming that all these events occur at high frequency compared to the evolution of mean-field quantities, they can be described through a granular temperature [161]. A reasonable assumption is to consider that this temperature is related to the local velocity fluctuations, through the proportionality relation:

$$k_B T(z) \sim m \delta v^2(z) \quad \text{with} \quad \delta v^2(z) = \langle |v(z, t) - \langle v(z, t) \rangle|^2 \rangle, \quad (7.2)$$

the local variance of the velocity field $v(z, t)$ along the flow direction. Figure 7.3a shows the evolution of the dimensionless standard deviation $\overline{\delta v}/(d\bar{\gamma})$, where $\bar{A} = \frac{1}{H} \int_0^H dz A(z)$ represents the thickness average of $A(z)$, as a function of the inertial number, for frictional and frictionless grains. We stress that the dimensionless standard deviation is independent of z due to the Bagnold profile satisfied by $\langle v(z, t) \rangle$ and the affine spatial behaviour of the variance observed in Fig. 7.3b. Interestingly, no matter the frictional nature of the grains, all the data reported here and in the literature collapse onto a single master curve showing a decrease of the relative velocity fluctuations with increasing inertial number. For small I values ($I < 0.07$), the dimensionless standard deviation decreases as $I^{-0.52 \pm 0.01}$, while it

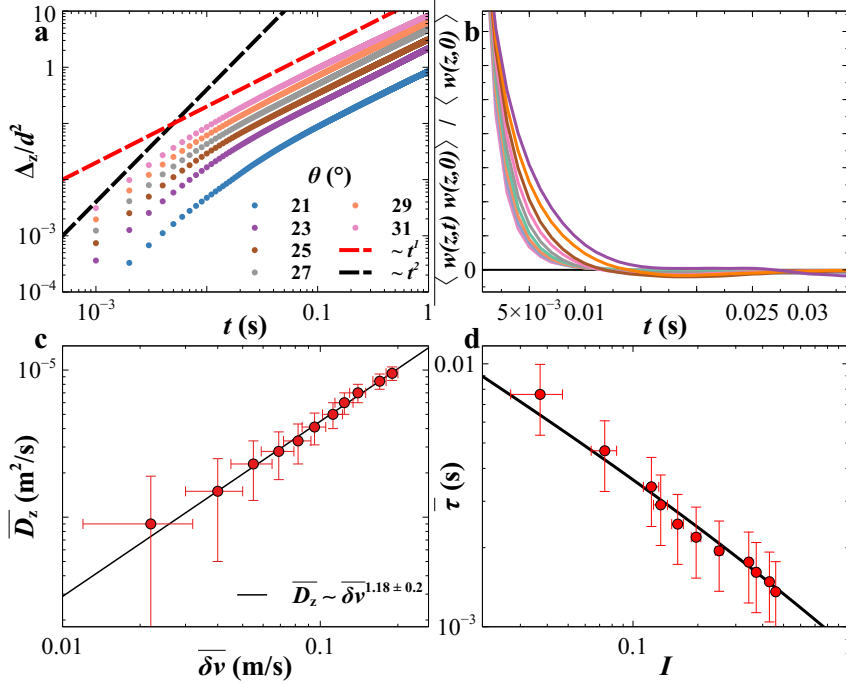


Figure 7.4: a) Mean square displacement Δ_z along the z coordinate averaged over all the grains. b) Time correlations of the velocity following z for a layer of frictional grains initially characterized by $H_1 = 30d$ and various inclination angles as indicated. Inset: Log-lin plot of the velocity correlations. c) Thickness-averaged diffusion coefficient \overline{D}_z along z as a function of the thickness-averaged standard deviation $\overline{\delta v}$ of the velocity field for fictional grains. The solid line indicates a fitted expression as provided in the legend. d) Correlation time $\overline{\tau}$ of the thickness-averaged velocity fluctuations as a function the inertial number I . The black solid line corresponds to $0.26 d/(l_c \overline{\gamma})$, with $l_c/d = a(1 + b/I^{0.52})$ with $a=0.25$ and $b=1.5$ found in panel a.

seems to saturate to a constant value at large I [164]. Interpolating the two asymptotic behaviours through a simple crossover form, one gets $\overline{\delta v}/(d\dot{\gamma}) = a(1 + b/I^{0.52})$, that fits well the data with $a = 0.25$ and $b = 1.5$ (see black line in Fig. 7.3a).

Let us now investigate the impact of the effective thermal energy on the grain dynamics. As shown by the time evolution of their thickness-averaged mean-square displacement along z (see Fig. 7.4a), the grains globally diffuse perpendicularly to the flow direction, at long time with an associated thickness-averaged diffusion coefficient $\overline{D_z}$ increasing with the inclination angle θ . Furthermore, as shown in Fig. 7.4c, $\overline{D_z}$ increases linearly with the thickness-averaged standard deviation $\overline{\delta v}$ of the velocity field. This linear relation can be understood from the thickness-averaged Kubo relation [1]:

$$\overline{D_z} = \int dt \overline{\langle w(z,t)w(z,0) \rangle} \sim \overline{\tau(z)\delta v^2(z)} \sim d\overline{\delta v}, \quad (7.3)$$

with $w(z,t)$ the velocity field along z , at position z and time t , and where we assumed isotropic local velocity correlations of amplitude $\delta v^2(z)$ decaying in an exponential fashion over a local characteristic time $\tau(z) \sim d/\delta v(z)$. In addition, given the affine trends in Fig. 7.3b, one can show that $\overline{\tau} \sim d/\overline{\delta v}$. The thickness-averaged temporal correlations functions $\overline{\langle w(z,t)w(z,0) \rangle}$ of the velocity field along z , as calculated from the DEM trajectories (Fig. 7.4b), appear to decay faster with increasing θ . Neglecting long-time power-law tails, we can show that the exponential-decay time of $\overline{\langle w(z,t)w(z,0) \rangle}$ is well approximated by $\sim \overline{\tau}$. Besides, the velocity correlations suggest the existence of dynamic clusters that persist over the correlation time. We thus hypothesize the existence of a characteristic, mesoscopic and a priori z -dependent size $l_c(z)$ over which dynamic clusters persist during the time $\tau(z)$. This is reminiscent of the vortices discussed by Kharel and Rognon [164]. As proposed by DeGiuli and Wyart, these clusters produce an amplification of the velocity fluctuations that is estimated through a “lever” effect [166, 167]. Specifically, one has $l_c(z) \sim \frac{d}{\tau(z)\dot{\gamma}(z)}$, and, with the definition $\tau \sim d/\delta v$, one gets:

$$\frac{\delta v(z)}{d\dot{\gamma}(z)} \sim l_c(z)/d, \quad (7.4)$$

where the amplification factor appears clearly. Interestingly, since the left-hand side of the latter relation is independent of z , as discussed above, one gets that the dynamic-cluster size l_c is in fact independent of z for the inclined-plane configuration. Figure 7.4d shows $\overline{\tau}$, as estimated from the thickness-averaged temporal correlations functions shown in Fig. 7.4b, as a function of I . The data are in agreement with the relation $\overline{\tau} \sim \frac{d}{l_c\dot{\gamma}}$ with the l_c derived from the crossover expression between the two asymptotic regimes of Fig. 7.3a. Since the expression for l_c is independent of the frictional nature of the grains, this agreement suggests that the size of the dynamic clusters is mainly determined by the collisions between grains, but not by the microscopic friction between them. Furthermore, from Fig. 7.3a this dynamic-cluster size is expected to diverge at kinetic arrest – which is reminiscent of the hypothetical cooperative length associated with the glass and jamming

transitions. It should however be noted that some influence of the microscopic friction coefficient has been observed by DeGiuli and Wyart [166, 167], but for very small values of $I < 10^{-3}$ that are well below the range considered here.

In the following, we aim deriving the macroscopic rheological laws from the microscopic fluctuations and correlations. From dimensional analysis, we have recalled that a single parameter determines the flow properties. In the inclined-plane geometry, all dimensionless parameters are uniquely determined by the inclination angle $\theta \simeq \mu$. Therefore, the dimensionless ratio $Pd^3/(k_B T)$ should be constant in the layer for inclined-plane experiments. In a continuous mean-field approximation, the pressure field is hydrostatic, precisely:

$$P(z) = \phi \rho_p g (H - z) \cos \theta \simeq \phi \rho_p g (H - z). \quad (7.5)$$

It thus follows that the effective temperature must vary with the depth according to $T(z) \propto (H - z)$. As observed in Fig. 7.3b, apart from slight boundary deviations, the affine relation $\delta v^2(z) \propto (H - z)$ is satisfied for all the tested inclination angles θ , which supports the definition of the effective temperature through $k_B T(z) \sim m \delta v^2(z)$. Interestingly, the effective temperature and the associated mechanical noise are maximal near the substrate and vanish at the free interface. This suggests that the collisions between mobile grains and the glued ones at the substrate is the source of temperature in the system. Furthermore, using the definition of the inertial number, the pressure can be written as $P(z) \sim \frac{m \dot{\gamma}(z)^2}{d I^2}$. Combining this relation with $\delta v(z) \sim l_c \dot{\gamma}(z)$, and the definition of the effective temperature, one gets:

$$Pd^3/(k_B T) \sim d^2/(l_c^2 I^2). \quad (7.6)$$

The cluster size can be derived from free volume and cluster fractal shape arguments. Indeed, the required free volume to allow the motion of a grain implies the collective motion of N_c grains forming a dynamic cluster. The number of grains involved scale as $N_c \sim 1/(\phi_c - \phi)$. Assuming chain-like clusters with random walk-like geometry [168, 169], their size should be given by $l_c \propto N_c^\nu$ with $1/2 \leq \nu \leq 3/5$ (clusters being described as random walks or self-avoiding random walks). The size of the cluster then scales with the packing fraction as $l_c \sim d/(\phi_c - \phi)^\nu$. Inserting this relation in the expression for the pressure yields:

$$Pd^3/(k_B T) \sim (\phi_c - \phi)^{2\nu}/I^2. \quad (7.7)$$

By identifying the latter relation with the equation of state (EOS) for hard-sphere fluids near the jamming transition [139, 145], that is $Pd^3/(k_B T) = \phi_J/(\phi_J - \phi)$, the dilatancy law can be established in terms of ν :

$$(\phi_c - \phi) \sim I^{2/(2\nu+1)}. \quad (7.8)$$

with $0.91 \leq 2/(2\nu + 1) \leq 1$, provided that we assume that $\phi_J = \phi_c$. These dependencies in inertial numbers are in agreement with the observations. For the dilatancy law, Fig. 1d shows that the exponent $\alpha = 2/(2\nu + 1)$ is equal to 0.89 ± 0.10 for frictional and 0.73 ± 0.34

for frictionless grains. The large uncertainty observed for frictionless data is related to the lack of values at large I . For the cluster size, the theory predicts a law:

$$l_c \sim d/I^\beta \quad \text{with} \quad \beta = 2\nu/(2\nu + 1). \quad (7.9)$$

As shown in Fig. 7.3a, we observe $\beta = 0.52 \pm 0.01$ in very good agreement with the prediction for this exponent, namely $0.5 \leq \beta \leq 0.54$. The universal agreement for both frictionless and frictional grains can be related to the evolution of the cluster size with inertial number, and reflects once again the dominance of collisions over friction in the dynamics. The validity of the hard-sphere-fluid EOS is probably limited to moderate inertial numbers, in other words $I \lesssim 0.5$, where the granular system can be considered as a fluid and where the mechanical noise ensures that no long-range correlations develop. Indeed, it is likely that a transition to another dynamics regime appears close to the jamming, where the mechanical fluctuations become less relevant. For very small values of inertial numbers, different dilatancy laws were proposed with exponent close to 0.4-0.53 [149, 170]. Recent investigations of frictionless systems with varying restitution coefficients have shown that close to jamming, the exponent describing the dilatancy law can vary from 0.6 to 1.5, while it should be close to 1 for large values of I [171].

7.3 Microscopic picture

Let us finally propose a microscopic picture for the $\mu(I)$ rheological law. To do so, we consider the steady-state balance of driving and dissipated powers for a test grain located in a slab of thickness d at height z . First, to estimate the driving contribution, we consider that the grain experiences the sum of gravitational and friction forces projected in the flow direction, and that θ and θ_c are small, leading to an effective driving force $\sim \rho_p \phi g (H - z) d^2 (\theta - \theta_c)$. Since the grain moves over a distance d within a time $\dot{\gamma}(z)^{-1}$, the net local driving power is:

$$\dot{W}_d(z) \sim \rho_p \phi g (H - z) d^3 (\theta - \theta_c) \dot{\gamma}(z). \quad (7.10)$$

Secondly, we assume that the energy is mainly dissipated through the collisions with other grains, characterized by the characteristic decay time $\tau(z) \sim d/[l_c \dot{\gamma}(z)]$. The local power dissipated by collisions can thus be estimated by:

$$\dot{W}_c(z) \sim m \delta v^2(z) / \tau(z). \quad (7.11)$$

Balancing $\dot{W}_d(z)$ with $\dot{W}_c(z)$, and recalling that $\delta v \sim \dot{\gamma} l_c$, leads to $\dot{\gamma}^2 \sim g d \phi (H - z) (\theta - \theta_c) / l_c^3$. At small angles, and thus small I , Fig. 7.3a shows that the cluster size is adequately described by the relation: $l_c \sim d I^{-\beta}$. Inserting this expression in the previous one, together with the definition of I , yields the general relation:

$$\dot{\gamma} \sim \left[\frac{g \phi (H - z)}{d^2} \right]^{1/2} (\theta - \theta_c)^{1/(2-3\beta)}. \quad (7.12)$$

First, this expression is compatible with the z -dependency of the Bagnold velocity profile, $\langle v(z, t) - v(0, t) \rangle \propto H^{3/2} - (H - z)^{3/2}$. Secondly, recalling that $\mu \simeq \theta$, together with the definition of I , Eq. (7.12) yields the friction law:

$$\mu - \mu_c \sim I^{2-3\beta}. \quad (7.13)$$

Considering the theoretical range of β that is derived from ν , $0.50 \leq \beta \leq 0.54$, we obtain a prediction for the exponent, i.e. $0.38 \leq (2 - 3\beta) \leq 0.50$, in close agreement with the law $\mu - \mu_c \sim I^{0.40 \pm 0.01}$ observed for frictionless grains shown in Fig. 7.2c.

We emphasize that the proposed model, based on a fractal dimension for the chain-like clusters related to a simple random walk, is able to properly predict three different laws based on the measurements of velocity fluctuations ($\delta v / \dot{\gamma} \sim l_c \sim dI^{-0.52}$), packing fractions ($\phi_c - \phi \sim I^{0.9}$) and flow velocity ($\mu - \mu_c \sim I^{0.4}$).

One might expect Eq. (7.12) to also hold for frictional systems, since the velocity fluctuations and cluster size behave similarly with the inertial number for both frictional and frictionless systems. However, Eq. (7.12) cannot explain the $\mu - \mu_c \sim I$ relation observed for frictional grains in Fig. 7.2c. This disagreement is in fact not surprising. In the derivation of Eq. (7.12), it is assumed that all the energy dissipation arises from collisions between grains. This is a very reasonable assumption for frictionless systems, but an additional source of dissipation is expected from the mobilization of frictional contacts. Unfortunately, including frictional dissipation in a theoretical model for dense granular flows remains a highly debated issue [158, 166, 167]. Nevertheless, interestingly, Fig. 7.2c shows that for large-enough inertial numbers, the data obtained for frictional systems collapse onto the law of frictionless systems. This observation suggests that, in the limit of large I , the energy dissipation is universal and of collisional origin.

We also note that changing the value of the microscopic sliding friction coefficient μ_s , from 0.3 to 1, only shifts the threshold values $\mu_c(\mu_s)$ and $\phi_c(\mu_s)$ but has no impact on the scaling laws.

7.4 Discussion

We have demonstrated from numerical simulations and examination of existing literature data that the dilatancy law is consistent for both frictionless and frictional assemblies. This law can be better understood by comparing two key elements:

First, the equation of state constructed from hydrostatic pressure, an effective granular temperature related to velocity fluctuations, and the inertial number; and second, the equation of state of hard-sphere fluids near the jamming transition. In contrast, the macroscopic laws of friction are observed because frictionless and frictional assemblies are inherently different. For frictionless assemblies, we can rationalize the observations from a grain-level energy balance that includes gravity, effective friction, and collisions. This also

allows us to recover the Bagnold profile for the local mean velocity field. The derivation of a macroscopic friction law for frictional assemblies remains an open question. Addressing this issue will likely require an additional dissipation term, one that accounts for the formation of frictional contacts.

A new and interesting approach to handle granular material problems by Moshe *et al.* has recently been published [172, 173]. This theory proposes a geometric derivation for a mechanical screening in amorphous solids, which is in some way analogous to theories of electrostatic screening such as dielectrics and the Debye-Hückel theory. So far, these ideas have been tried only for static scenarios. An attempt to include dynamics, in the non-equilibrium steady state, may be a way to overcome some of the difficulties we encountered in the present study. A relation to screening phenomena, if exists, might lead to a connection with the first part of this manuscript.

Chapter 8

Appendix – Part II

In this appendix, we show some basic flow quantities obtained from DEM simulations. Specifically, the dependence on friction, the flow profile as a function of depth, and the velocity correlations.

8.1 Friction

Additional simulations were carried out while changing the value of the microscopic sliding friction coefficient μ_s , from 0.3 to 1. As shown in Fig 8.1, we note that it only shifts the threshold values $\mu_c(\mu_s)$ and $\phi_c(\mu_s)$ but has no impact on the scaling laws. By simply subtracting the threshold value, we obtain a collapse of all our data on a single master curve.

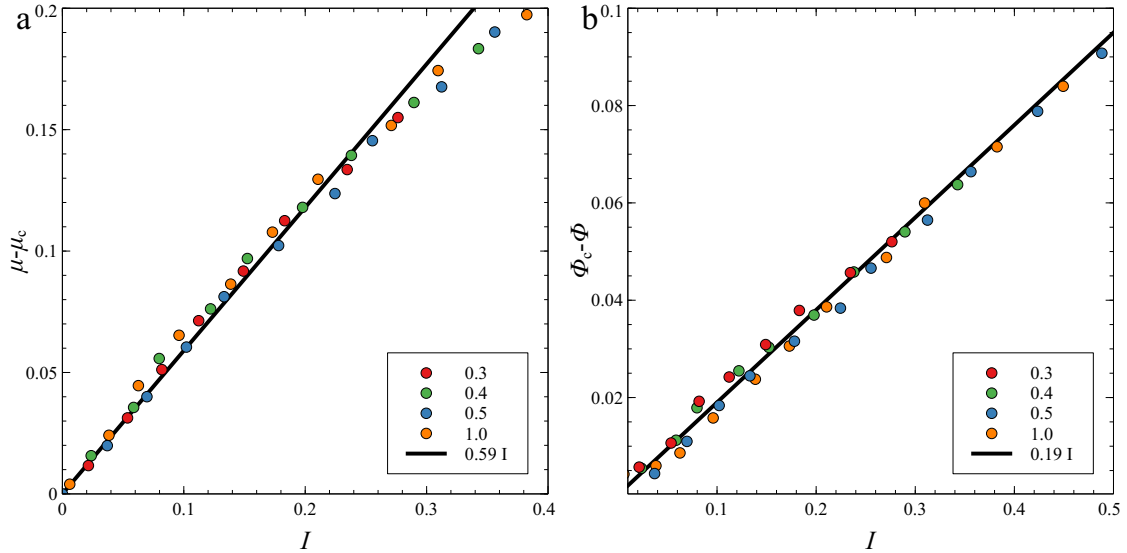


Figure 8.1: a) Shifted effective friction coefficient, $\mu - \mu_c$ as a function of the inertial number $I = \dot{\gamma}d\sqrt{\rho_p/P}$, obtained for a layer of grains with an initial layer thicknesses $H_i = 20d$ and various microscopic sliding frictions μ_s as indicated. The solid line indicates a linear fit of the small I values as provided in legend. b) Shifted volume fraction $\phi_c - \phi$ as a function of the inertial number I . The solid line indicates a linear fit as provided in legend.

8.2 Bagnold-like flows

In order to check the validity of our DEM simulations of granular flows on inclined planes, we study in details the properties of the flow. We observe that the local time-averaged velocity profile is well described by a Bagnold profile $\langle v(z) - v(0) \rangle \sim H^{3/2} - (H - z)^{3/2}$ (see Fig. 8.2a). Besides, the inertial number I (see Fig. 8.2b) and the volume fraction ϕ (see Fig. 8.2c) remain mostly constant throughout the layer (except at both boundaries) for all the studied inclination angles. These observations are in good agreement with previously reported observations [91, 100, 105, 152, 153].

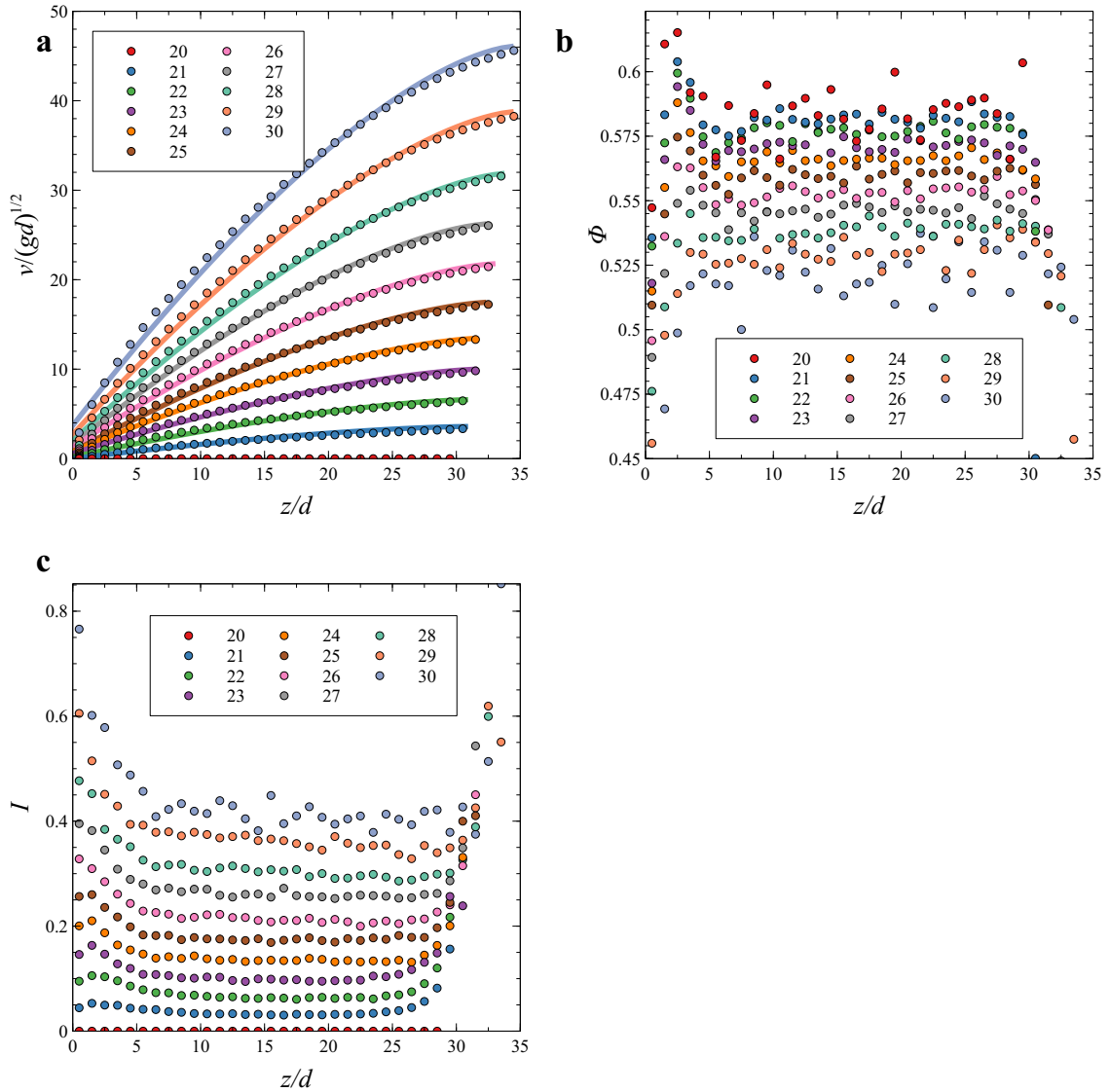


Figure 8.2: Evolution of the rescaled local velocity (a), volume fraction ϕ (b) and inertial number I (c) as functions of rescaled normal coordinate z/d for a layer of frictional grains initially characterized by $H_i = 30d$ and various inclination angles θ as indicated. The curves in (a) corresponds to the best fit of the Bagnold profile expression.

8.3 Velocity correlations and diffusion

As shown in Fig. 8.3a, we calculate the mean square displacement (Δ_z , MSD) along the z coordinate averaged over all the grains for various inclination angles. From those MSD, the thickness-averaged diffusion coefficient, $\overline{D_z}$ is evaluated by fitting the data in the diffusive regime, i.e. where $\Delta_z = 2\overline{D_z}t$. In addition, we also evaluate the time correlation of the z -component of the velocity w , averaged over the layer thickness, for various inclination angles. The thickness averaged correlation times, $\overline{\tau}$ were obtained by fitting the correlation curves with decreasing exponentials of the type $\sim e^{-t/\overline{\tau}}$.

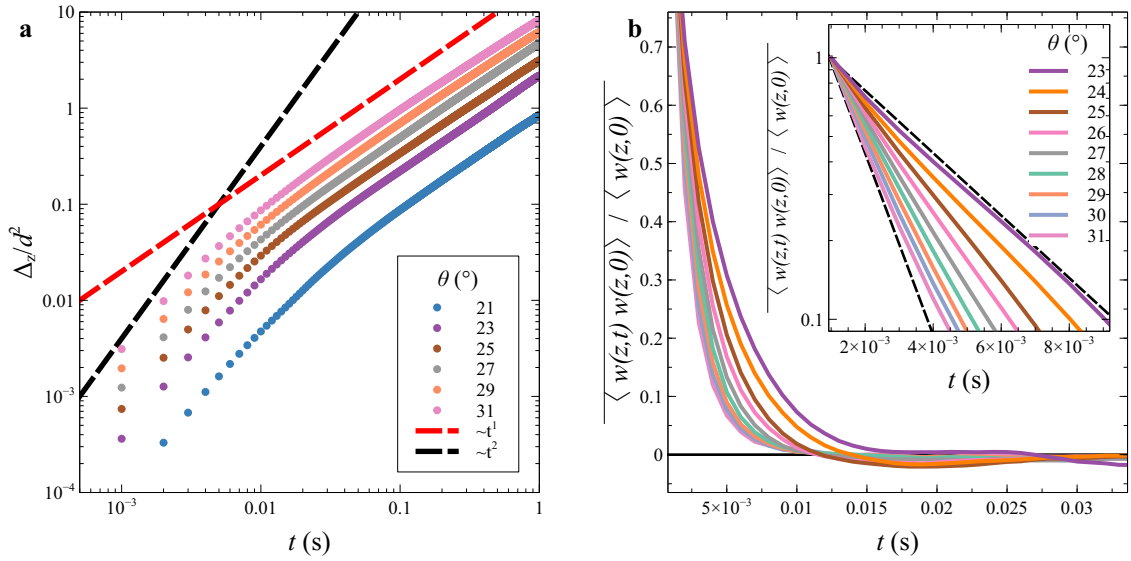


Figure 8.3: (a) Mean square displacement Δ_z along the z coordinate averaged over all the grains and (b) time correlations of the velocity following z for a layer of frictional grains initially characterized by $H_i = 30d$ and various inclination angles as indicated. Inset: Log-linear plot of the velocity correlations.

Part III

Polymer glasses and confinement

Chapter 9

Basic concepts in glass and polymer physics

Some liquids do not undergo a first-order phase transition to the crystalline solid state when cooled to low temperatures, but rather exhibit a metastable “supercooled” liquid-like behavior with sharply increasing relaxation times as the temperature is lowered [174–178] – a phenomenon known as the glass transition [140, 179].

While recent theoretical breakthroughs have shown the existence of an ideal glass transition in infinite spatial dimensions [180], a complete understanding of the formation of real glassy materials remains a central unsolved problem in condensed matter physics [181]. In addition to the interest in this fundamental problem, glassy materials are widely used and their rheology and stability have significant technological importance.

9.1 Glass Transition

The phenomenon of glass transition has long fascinated researchers in condensed matter physics. It refers to the transformation of a supercooled liquid into a glassy state, characterized by a dramatic increase in viscosity. This transition is conventionally characterized by the temperature T_g , known as the glass transition temperature. The occurrence of this transition is not limited to silica glasses. It is also observed in various materials such as glycerol, polymers, oxides, and metals [182]. In general, physicists use the word glass to describe materials that exhibit mechanical properties similar to those of solids but lack the long-range structural order.

Unlike a classical phase transition, this change does not occur at a precise temperature, but over a range, and its exact nature is determined by several factors, including cooling rate, pressure, and molecular weight of the material. The mechanical properties of the glass are also affected by these factors [183].

Glasses are out of equilibrium materials. As the material is cooled, packing frustration begins, eventually reaching a point where there is not enough available thermal energy to allow the system to explore all the different possible configurations on accessible time scales [140]. In other words, the system falls out of equilibrium and becomes trapped in a (non-equilibrium) local energy minima state associated with the conditions it has

experienced.

At its core, the glass transition is a dynamical phenomenon. It marks a shift in the internal degrees of freedom of the material as the supercooled liquid cools and achieves kinetic stability, but not thermodynamic stability. This characteristic distinguishes the glass transition from a classical phase transition, where the system reaches a new thermodynamic equilibrium state [140].

This non-equilibrium transition occurs over a range of temperatures and glass transition temperature T_g marks the boundary between the supercooled liquid state and the glassy state. During the transition, the material undergoes dramatic changes in physical properties, including thermal expansion, heat capacity, and viscosity, while the structural order remains essentially unchanged. The glass transition temperature is not a constant for a given material, but depends on the history of the material, especially the rate of cooling.

Since T_g has no unique value for a given system, in contrast to classical phase transitions, it is usually determined by tracing the change in some macroscopic quantity (such as specific volume) with temperature and extrapolating the trend of the curves at high and low temperatures. The intersection of the two extrapolated curves marks the glass transition, see Fig. 9.1.

Is T_g a meaningful concept? As we already mentioned, the glass transition temperature depends on how long our available experimental time is, and thus on the cooling rate. This poses issues with the definition of a “transition”: what is the point in fixing a transition at a temperature whose value depends on the experimental protocol. However, in many systems the increase of the relaxation time is sharp enough to make it hard to move significantly the value of T_g , even by a substantial change in the cooling rate. The reason for this is that, whatever is the true underlying physical mechanism, the increase of the relaxation time when decreasing the temperature is at least exponential. To fix ideas, let us assume that we have a simple liquid in equilibrium. The relaxation time τ is governed by Boltzmann statistics so the dependence on the temperature is $\tau = \tau_0 \exp\left(\frac{\Delta E_0}{k_b T}\right)$, where ΔE_0 is some characteristic energy barrier and τ_0 is some characteristic microscopic relaxation time. At the glass transition $T = T_g$ we roughly have:

$$\tau = \tau_0 \exp\left(\frac{\Delta E_0}{k_b T_g}\right). \quad (9.1)$$

We obtain, by differentiating both sides of Eq. (9.1) and rearranging the terms:

$$dT_g = -\left(\frac{k_b T_g^2}{\tau_0 \Delta E_0}\right) \exp\left(-\frac{\Delta E_0}{k_b T_g}\right) d\tau, \quad (9.2)$$

which shows that a change we allow in τ , has an exponentially small effect on T_g .

9.1.1 Thermodynamic point of view

From a thermodynamic perspective, the glass transition is difficult to define because it lacks the long-range order and sharp discontinuity typically associated with phase transitions. Instead, it manifests as a second-order-like transition with an increase in heat capacity but no latent heat. As the system cools, it loses the ability to find the free energy minimum – the crystalline state. This is characteristic of a supercooled liquid in a metastable state. Therefore, macroscopically the system is out of equilibrium, but locally atoms or molecules may be in a local energy minimum.

Stated differently, for a probability distribution over phase space of a system that presents a supercooled liquid state, the average value (the crystal state) and the typical value (what is observed, a liquid) are not the same. This can be remedied and the system can still be treated as equilibrium by ignoring the crystalline state and redefining a probability distribution over a subset of phase space. In this subspace, the average and the typical states are the same¹.

The so-called Kauzmann paradox arises from the comparison of the entropy of the supercooled liquid and the corresponding crystalline state. As the temperature decreases, the difference in entropy between the supercooled liquid and the crystal also decreases, so the entropy curve of the supercooled liquid is extrapolated to a temperature (T_K , the Kauzmann temperature, see Fig. 9.1) where the supercooled liquid would have the same entropy as the crystal. Below T_K , the liquid would theoretically have a lower entropy than the crystal. Generally speaking, the fact that some phase of matter would have lower entropy than the crystal does not violate any law of thermodynamics. However, the third law of thermodynamics would be violated if the entropy of the supercooled liquid continued to decrease well below T_K without any change in slope, since otherwise one would find that it becomes zero above $T = 0$.

In reality, for a finite cooling rate, the material undergoes a transition and the slope of the entropy changes in such a way that no catastrophe is manifested. This paradox serves as a stimulus for several theoretical approaches to understanding the glass transition.

9.1.2 Dynamics

The unique dynamics of the glass transition can be explained by the relaxation time of the system. In a high-temperature liquid, the system quickly adapts to temperature changes and easily establishes a new equilibrium. However, as the temperature decreases, the viscosity increases and the time required for the system to rearrange and reach equilibrium increases significantly, especially around T_g . This critical slowing down of the relaxation dynamics is a key feature of glass-forming materials.

The viscosity of simple liquids exhibits an Arrhenius-like dependence on temperature,

¹Surprisingly, this procedure is related to observations in the domain of economics. In particular, distinguishing between seemingly profitable games [184].

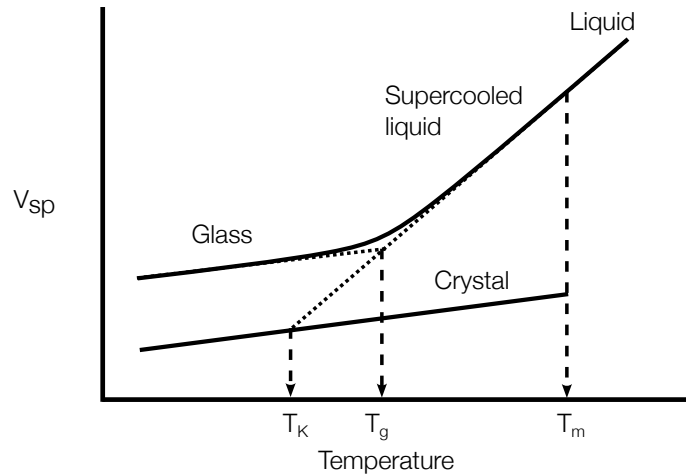


Figure 9.1: Specific volume or entropy plotted as a function of temperature for a glass-forming material. At high temperature, the system is in an equilibrium liquid state where the molecules easily slide past each other. Upon cooling, if the glass-former avoids crystallization, the system enters into a supercooled liquid regime. The dynamics begin to slow as cooperative motion sets in. Upon cooling further, the system falls out of equilibrium at T_g into a glass whose thermal expansion is comparable to that of the crystal. The value of T_g depends on the cooling protocol. In other words, if the system is cooled more slowly, it reaches a lower temperature before finally falling out of equilibrium into a glass.

where the viscosity grows exponentially with the inverse of the temperature: $\eta \sim \exp\left(\frac{\Delta E}{k_B T}\right)$. This relation can be understood in terms of relaxation processes that respect Boltzmann statistics, ΔE being some energy barrier for a relaxation process to occur. Supercooled liquids show a non-Arrhenius temperature dependence characterized by a significant slowing of the dominant relaxation time τ_α and an apparent divergence of the viscosity within a relatively small temperature range (T_g to $T_g + 50$ K). This behavior is often well fitted by the empirical Vogel-Fulcher-Tammann (VFT) equation:

$$\tau_\alpha = \tau_0 \exp\left(\frac{A}{T - T_0}\right) \quad \text{and} \quad \eta \sim \tau_\alpha, \quad (9.3)$$

where τ_0 , A , and T_0 are parameters of the empirical model, and depend on the material.

In 1965, Adam and Gibbs [185] came up with an explanation for the non-Arrhenius behavior. They argued that the conventional transition state theory for liquids, which assumes that a single molecule crosses energy barriers created by its neighbors, is inadequate. Instead, viscous flow occurs through increasingly cooperative rearrangements of groups of particles.

According to the Adam-Gibbs model, the relaxation time of the liquid is controlled by the configurational entropy S_c . This quantity is defined by subtracting the vibrational entropy,

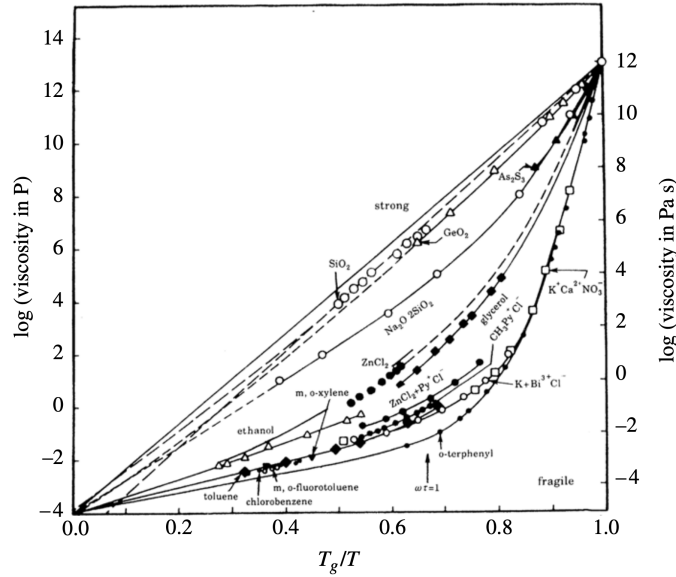


Figure 9.2: Logarithm of viscosity versus rescaled inverse temperature for many substances. This representation of the data shows pure Arrhenius behavior as a straight line. This is typical for so-called “strong” glass formers. On the other hand, a sharper super-Arrhenius increase in viscosity corresponds to “fragile” glass formers (Figure taken from [178]).

S_v , from the total entropy. In their model $\Delta E(T) \sim \frac{1}{S_c(T)}$ which leads to:

$$\tau_\alpha = \tau_0 \exp\left(\frac{C}{T S_c(T)}\right), \quad (9.4)$$

where C is a constant containing a term $\Delta\mu$ which is the free energy barrier that the rearranging group must cross. It is clear that as long as the configurational entropy remains constant, this is just another form of the Arrhenius law. What makes the equation unique is that due to the increase in heat capacity at the glass transition, configurational entropy increases with temperature. This adds another temperature dependence to the exponential law. Finally, if the excess configurational entropy vanishes at some finite temperature due to Kauzmann’s paradox, then we can write:

$$S_c = \int_{T_K}^T \frac{\Delta C_p(T)}{T} dT \approx \Delta C_p \log(T/T_K), \quad (9.5)$$

with ΔC_p being the difference of specific heat between the liquid and the glassy state. By plugging Eq. (9.5) into Eq. (9.4) one gets:

$$\tau_\alpha = \tau_0 \exp\left(\frac{D}{T \log(T/T_K)}\right), \quad (9.6)$$

which recovers qualitatively the non-Arrhenius behavior of the VFT formula in Eq. (9.3). This work provided a connection between thermodynamic and dynamic quantities, launched a wide range of investigations and played a central role in glass transition studies [186–189].

To relate these ideas to polymer glass formers, we first review some basic concepts from the field of polymer physics.

9.2 Polymer physics

Polymers are an integral part of our daily lives, from the natural bio-polymers of DNA and proteins to the synthetic polymers that make up plastics and textiles. A polymer is a substance or material consisting of large, string-like molecules composed of many repeating subunits called monomers. Polymer physics is a specialized branch of physics that seeks to understand the behavior and properties of these important materials.

Understanding the behavior of polymers requires statistical approaches. The behavior of large polymers, those with many monomers, can be efficiently described in the thermodynamic limit of infinitely many monomers. The effect of thermal fluctuations on polymers in liquid solutions is continuous and significant, requiring the use of principles from statistical mechanics and dynamics to model them.

9.2.1 Molecular weight

Molecular weight is a critical parameter in the characterization of polymers as it significantly influences the material properties. Due to the typically broad distribution of molecular weights in a polymer sample, there are several ways to express the molecular weight of polymers.

The most straightforward concept is the number averaged molecular weight (M_n). It is calculated by summing the product of the number of molecules (N_i) and their respective molecular weights (M_i), divided by the total number of molecules:

$$M_n = \frac{\sum N_i M_i}{\sum N_i}, \quad (9.7)$$

However, the number averaged molecular weight does not take into account the weight fraction of different species in the distribution. Therefore, the weight averaged molecular weight (M_w) is introduced. It is the sum of the product of the number of molecules (N_i), their molecular weight (M_i), and the molecular weight divided by the sum of the product of the number of molecules and their molecular weight:

$$M_w = \frac{\sum N_i M_i^2}{\sum N_i M_i}. \quad (9.8)$$

Since these averages often give different values for the same polymer sample, the polydispersity index (PDI) is used to characterize the width of the molecular weight distribution. It is the ratio of the weight averaged molecular weight to the number average molecular weight:

$$\text{PDI} = \frac{M_w}{M_n}. \quad (9.9)$$

If all polymer chains in a sample had exactly the same length, they would all have the same molecular weight and the polydispersity index would be 1. In reality, due to the nature of most polymerization processes, the polymer chains have a distribution of lengths and therefore molecular weights, resulting in a $\text{DPI} > 1$.

A high polydispersity index indicates a broad molecular weight distribution and a low polydispersity index indicates a narrow molecular weight distribution. The polydispersity index can affect the physical properties of the polymer, such as its rheological behavior, mechanical strength, and crystallinity. In this work we will consider polymer systems with PDI close to 1 experimentally. In the theoretical treatment we assume PDI equals 1.

9.2.2 Gaussian chains

In the statistical approach to polymer physics, an analogy is often drawn between a polymer and a random walk in certain cases, a self-avoiding random walk. The simplest polymer model is represented by the ideal chain, which corresponds to a simple random walk on a lattice. The molecular weight of a polymer chain is determined by the number of monomers it contains, denoted as N , and the size of an individual monomer is equal to the distance between adjacent vertices of the lattice, denoted as a . Consequently, the length of the polymer chain, denoted by L , can be expressed as $L = Na$.

As N increases, the conformation of the polymer chain can be modeled by a Gaussian distribution. At high molecular weights, it becomes possible to move to a continuous description of the polymer chain using Brownian motion. In this continuous limit, we assume that a tends to zero and N tends to infinity, while the product $L = a\sqrt{N}$ remains finite. Under these conditions, the probability distributions of the lengths in the polymer chain can be accurately described by the paths of Brownian motion. This allows the application of statistical mechanics and other tools from probability theory to model the behavior of large polymer chains.

We define the end-to-end distance of an ideal polymer chain as follows:

$$\mathbf{R} = \sum_{i=1}^N \mathbf{a}_i. \quad (9.10)$$

Since the trajectory corresponds to a random walk where $\langle \mathbf{a}_i \rangle = 0$ and $\langle \mathbf{R} \rangle = 0$, the mean value of the end-to-end distance is zero. However, the mean square value reads:

$$\langle \mathbf{R}^2 \rangle = \sum_{i,j=1}^N \langle \mathbf{a}_i \mathbf{a}_j \rangle = Na^2. \quad (9.11)$$

Therefore, a scale for the size of the polymer is $R_0 = a\sqrt{N}$. The quantity is closely related

to the radius of gyration of a polymer, which is defined as:

$$R_g^2 = \frac{1}{N} \sum_{i=1}^N \langle (\mathbf{R}_i - \mathbf{R}_{cm})^2 \rangle, \quad (9.12)$$

with $\mathbf{R}_{cm} = \frac{1}{N} \sum_{i=1}^N \mathbf{R}_i$ the center of mass. It is the usual way to describe the dimensions of a polymer chain [190]. Within the Gaussian chain approximation, $R_g^2 = \langle \mathbf{R}^2 \rangle / 6$. The probability $P(\mathbf{R})$ that a chain starts at 0 and ends at \mathbf{R} is given by:

$$P(\mathbf{R}) = \frac{A_N(\mathbf{R})}{(2d)^N}. \quad (9.13)$$

Here, $A_N(\mathbf{R})$ corresponds to the number of paths starting at 0 and ending at \mathbf{R} , and $(2d)^N$ represents the total number of paths in dimension d . Since \mathbf{R} is the sum of a large number of independent random variables, the central limit theorem can be utilized, leading to a Gaussian probability for the end-to-end distribution:

$$P(\mathbf{R}) = \left(\frac{3}{2\pi N a^2} \right)^{3/2} e^{-\frac{3\mathbf{R}^2}{2Na^2}}. \quad (9.14)$$

This is of course an approximate formula in the large N limit, but for many applications it will be a useful simplification. This property is well known in the context of random walks. However, a chain does not perfectly follow a Gaussian distribution because chain segments cannot overlap one another in space, what is known as the excluded volume effect. We can model the polymer by a path on a lattice with the constraint that a path cannot pass through the same node of the lattice twice. These types of random walks are called self-avoiding random walks, where one finds a different exponent in Eq. (9.11). In 3 dimensions, the exponent is close to $3/5$ [191].

The upcoming study in the next chapter deals with polymer melts, where a fascinating screening phenomenon occurs. The excluded volume effect is screened and the “naive” random walk calculation surprisingly turns out to be correct [192]. Put simply, in a melt, on average, any point in space is occupied by a monomer. This means that space is homogeneous. When space is homogeneous, each polymer segment must displace other segments to fit in. Displacing other parts of the same chain is equivalent to displacing other chains. This renders spreading (the common terminology is swelling) useless. Therefore, the simple random walk distribution is expected to be recovered.

9.2.3 Persistence length

The concept of persistence length is an important parameter that characterizes the stiffness of a polymer chain. The persistence length can be understood as the length scale over which a polymer chain remains aligned along a tangent before bending due to thermal fluctuations. In other words, beyond this length, a polymer chain can be treated as an unbiased random walk. This notion allows us to reduce a polymer chain that has stiffness

to a similar chain that is completely flexible but contains a fraction of the real number of monomers [191].

If we imagine a polymer as a string of beads (where each bead represents a monomer), a rigid rod would have a large persistence length (since it resists bending), while a floppy string would have a small persistence length.

In mathematical terms, the persistence length (usually denoted as L_p) is defined by the tangent-tangent correlation function. If $\mathbf{t}(s)$ is a unit vector tangent to the chain at the point s along the chain, then the average value of the scalar product $\mathbf{t}(s) \cdot \mathbf{t}(0)$ typically decays exponentially with s/L_p :

$$\langle \mathbf{t}(s) \cdot \mathbf{t}(0) \rangle = e^{-s/L_p}. \quad (9.15)$$

Here, the brackets $\langle \rangle$ denote an ensemble average. This equation essentially says that the direction of the tangent at a point s along the chain becomes uncorrelated with the tangent at the origin over a distance of the order of the persistence length. Incorporating this into the Gaussian chain model would only affect the numerical factor of the results, but not the scaling. In other words, a stiff polymer chain with N monomers, unit size of a and persistent length L_p could be replaced by an ideal chain of length $\frac{Na}{L_p}$ and unit size L_p .

9.2.4 Polymer melts

A polymer melt is a state of a polymer that occurs at temperatures above its glass transition temperature (T_g) and below its decomposition temperature. Above T_g , the polymer chains have enough thermal energy to move freely and the material behaves more like a liquid than a solid, although it is not actually a liquid in the same way that water or oil are. This is due to the long, tangled nature of the polymer chains, which cannot easily flow past each other as they do in small-molecule liquids. The viscosity of a polymer melt is typically much higher than that of a small-molecule liquid. In fact, the exact dependence of viscosity on chain length is one of the open problems in polymer physics. Current models predict $\eta \sim N^3$, while experimental data suggest that the exponent should be in the range 3.3 to 3.4. See [191] for a detailed discussion.

In a polymer melt, the chains become highly entangled, resulting in unique rheological (flow) properties. For example, when a force is applied to a polymer melt, it initially resists deformation and behaves like a solid. However, if the force is maintained, the polymer chains will begin to slide past each other and the material will flow like a liquid. This behavior, known as viscoelasticity, is a defining characteristic of polymer melts.

9.2.5 Glass transition in polymers

In polymers, the chain segments are so tightly packed that movement is limited by the close presence of adjacent monomers, which may or may not be on the same chain. This is why chain connectivity does not play a dominant role in the glass transition and probably why

the glass transition in polymers exhibits most of the same characteristics as other small molecule glass formers. However, the absolute value of T_g exhibited by different polymers is influenced by their structure, chain stiffness and length [193].

A key phenomenology that explains the temperature dependence of the relaxation behavior in polymers is the Adam-Gibbs theory (Eq. (9.6)), which we have already discussed. This fact is of great importance, as it suggests that the structure of the macromolecules constituting the melt is, to some extent, unimportant in the glass transition process, and that the constraints imposed by the structure of the macromolecules do not play a major role in the kinetic arrest. The glass transition process in thin polymer films introduces an additional level of complexity compared to bulk polymers and serves as a valuable experimental model to study the so-called cooperative length scale proposed by Adam and Gibbs [194].

9.3 Measuring the glass transition temperature

Determining the glass transition temperature of an amorphous polymer typically involves a calorimetric measurement, the most common method for this purpose. Looking at a graph of calorific power versus temperature, there are four ways to determine T_g , each corresponding to different stages in the structural evolution of the system. It is important to note that the T_g value depends on the convention used for measurement.

Another method used to measure T_g is ellipsometry, an optical technique based on the change of state of the polarization of light when reflected on a flat surface. This technique is very sensitive and particularly effective for thin polymer films. It measures the reflection coefficient and the phase shift ratio of the parallel and perpendicular components of elliptically polarized light reflected from a surface. The glass transition temperature can be determined from the thickness and refractive index due to the difference in the coefficient of thermal expansion.

Chapter 10

On the bridge hypothesis in the glass transition of freestanding polymer films

10.1 Thin glassy films

Within glass-forming materials in the supercooled liquid state, particles are crowded and must move in a correlated manner to allow for a reorganization or relaxation event [185]. This phenomenology has been used to propose the emergence of a dynamical cooperative length scale [195]. The general idea is that for a relaxation process to occur, all particles within a region characterized by the cooperative length scale must reorganize simultaneously. To probe this hypothetical length scale, several different methods have been considered. The use of numerical simulations bulk [196] showed that these clusters of particles change their structure from compact (scales like 3rd power of a length scale) to stringy (fractal) around the glass transition. Other studies used mimetic jammed colloidal systems [98, 197] to find that the structure of these clusters can heavily depend on the sign of the interaction potential between the particles. An alternative strategy consisted in studying finite-size effects on the glass-transition temperature T_g , *namely* through systems with a similar nanometric size as the cooperative length at stake [198–201]. In particular, experiments and numerical studies investigating thin glassy polymer films. Starting with the famous study by Keddie at 1994 [202] and later many more have been performed [203–212].

These studies have revealed a set of rich and exotic phenomena. Most notably, a reduction of T_g in thin films of many materials was observed and was further attributed to a combination of the dynamical correlation length with an enhanced liquid-like surface mobility in glasses. These observations have been studied from a theoretical point of view as well, but there is no definitive consensus yet on the exact underlying mechanisms at play [169, 213–222].

Moreover, beyond the above generic confinement and interfacial behaviours of glassy materials made of small molecules or oligomers, and apart from possible residual stresses and artefacts induced by sample-preparation protocols [224], whether or not specific polymeric effects exist within the glassy physics is an interesting fundamental question with important practical implications given the widespread use of thin plastic films. Accordingly, freestanding polymer films with a thickness h comparable to the macromolecular radius

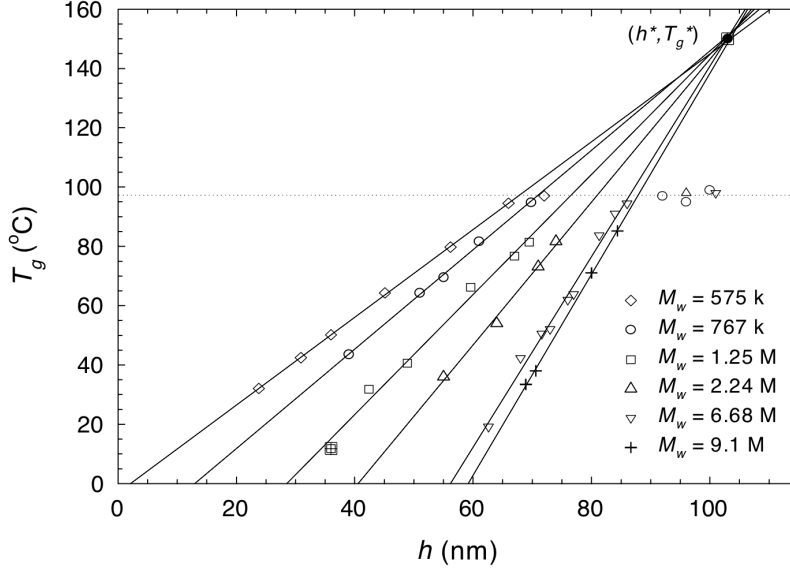


Figure 10.1: Glass-transition temperature T_g of freestanding polystyrene films as a function of film thickness h , for various average molecular weights M_w . By extrapolating the low-thickness linear regimes towards larger thicknesses, one empirically finds a universal crossing point, denoted by (h^*, T_g^*) . Figure reproduced from Ref. [223].

of gyration R_g were experimentally studied [223, 225–228]. The experiments showed that, for molecular weights $M_w < 378 \times 10^3$ – *in other words* ~ 3600 monomeric units – T_g does not exhibit any dependence on M_w , and the curves can be mapped onto the one for low- M_w supported films. However, for larger M_w , the T_g dependence on h and M_w becomes non-trivial, as shown in Fig. 10.1: at large thicknesses, T_g is equal to the bulk value T_g^{bulk} ; at small thicknesses, T_g decreases in an affine way with decreasing h , together with a slope moderately increasing with M_w . As such, the glass-transition temperature follows the empirical law:

$$T_g = T_g^* + f(M_w)(h - h^*), \quad (10.1)$$

for $h < h_c$, where $h_c = h^* + (T_g^{\text{bulk}} - T_g^*)/f(M_w)$ is a M_w -dependent critical thickness separating the two regimes, with f a slowly increasing function of M_w , and where h^* and T_g^* are the coordinates of an apparent universal crossing point obtained by extrapolating the low-thickness linear regime of Eq. (10.1) towards larger thicknesses (see Fig. 7.2). The function $f(M_w)$ was suggested to be logarithmic-like [225], a form which, perhaps coincidentally, is also present in other interfacial polymeric effects [229]. The existence of such a sharp transition in thin supercooled polymeric films suggests a change of dominating relaxation mechanism around h_c , from a generic bulk molecular one above h_c , to a purely confinement-induced polymeric one below h_c – indicating a probable connexion between h_c and some typical macromolecular polymeric length scale. In addition, the empirical trends suggest that the polymeric mechanism starts to be present below the universal onset thickness h^* , but remains less efficient than the bulk one for $h_c < h < h^*$. Moreover, it was proposed that the polymeric relaxation mechanism in thin supercooled polymer films requires two

free interfaces to be connected by bridges consisting of individual macromolecules [225] – which we refer to as the bridge hypothesis.

The glass transition in thin polymer films was further shown to have even a finer structure, with in fact two glass transitions occurring with some finite temperature gap in between them [230], corroborating the existence of three competing distinct relaxation mechanisms [231]: a bulk one, a confined molecular/monomeric one, and a confined polymeric one. These features are consistent with the observations made in Ref. [223], where a flow behavior in thin freestanding polymer films was only measured near T_g^{bulk} – independently of the actually-measured T_g . Moreover, by removing one of the two free interfaces of a freestanding polymer film, it was experimentally shown that the polymeric behaviour totally disappears [228, 232], which seems to corroborate the seminal bridge hypothesis. As a side remark, we note that the coupling between different relaxation mechanisms in the bulk was experimentally investigated in details recently, and revealed the role of intramolecular cooperative dynamics in the bulk polymeric glass transition [233].

As an early attempt to rationalize the affine trend in Eq. (10.1), de Gennes proposed a model based on free-volume arguments and an original sliding mechanism involving the reptation-like propagation of stress kinks along the macromolecular bridges [234, 235]. The focus on bridges is in alignment with the experimental finding that the phenomenon could be dramatically reduced by eliminating one of the free surfaces.

The basic idea of the models is that segments of chains connecting the two interfaces can slide relatively easily because both ends of the segments are free to move on the surface. These segments are called bridges and they provide an alternative relaxation mode that becomes more effective than the standard α relaxation at a certain thickness. This model assumed an infinite molecular weight, as well as a Gaussian-tail distribution of the free volumes along the chain backbone, and involved an ideal-random walk scaling for the average bridge length. Despite its merits, the sliding model suffered from intrinsic limitations, and could not reproduce all the experimental observations [228].

Milner and Lipson suggested a delayed-glassification model [236], extending the sliding model and computing the bridge-length distribution for infinite molecular weights, that led to a depth-dependent T_g and a decrease in the overall measured T_g [237]. The main difference between the delayed-glassification model and the sliding model is the way in which the propagation of kinks is treated. In the sliding model, it is treated as a series of Bernoulli trails, while in the delayed-glassification model, it is addressed as a first passage problem. But, once again, while the qualitative picture seemed appealing, the model could not reproduce the experimental data in a quantitative fashion.

To date, there is actually no model which quantitatively captures the M_w dependence of T_g in thin polymer films. In his seminal work [234], de Gennes suggested to refine his approach by performing a complete statistical treatment of the bridge distribution for finite-sized polymer chains in a thin film. This is thus the topic of the present work, where

we compute the bridge-length distribution, its mean value, and its proportion within a film, and use the obtained results in order to critically revisit de Gennes' sliding mechanism. We note that loops, namely chain portions connecting two points of a single interface, are not considered here for two reasons. First, supported films also contain loops but do not show the M_w behaviour of freestanding films [225, 228, 232]. Secondly, as will be discussed later in Sec. 10.4, adding loops to the calculation does not change the fundamentally M_w dependence.

10.2 Sliding mechanism

Here, we first recall the main ingredients of the sliding model [234]. Therein, the relaxation time τ is essentially set by the time required for a kink, that is some localised stress, to travel along a bridge, namely a portion of polymer chain connecting the two free interfaces. The kink travels along the chain backbone using successive independent jumps indexed by i and involving volumes ω_i , which are assumed to be normally and identically Gaussian-tail distributed, as:

$$p(\omega_i) = \sqrt{\frac{2}{\pi\omega_0^2}} e^{-\frac{\omega_i^2}{2\omega_0^2}}, \quad (10.2)$$

where the standard deviation ω_0 is assumed to be small compared to the monomer size $\sim a^3$, in order to reflect the fact that relaxation along the chain is easier than bulk molecular relaxation. The average relaxation time of this sequential process thus reads:

$$\tau = \tau_0 \left\langle \exp \left(\frac{1}{v_f(T)} \sum_i \omega_i \right) \right\rangle_{\mathcal{P}}, \quad (10.3)$$

where the average is made over the ensemble $\{\omega_i\}$ against the distributions $\mathcal{P} = \prod_i p(\omega_i)$, and where $v_f(T)$ is the free volume at temperature T . As classically done (see chapter 11 in [238]), v_f is assumed to vanish at a finite temperature T_V and to evolve in an affine way with temperature, so that:

$$v_f(T) = \alpha a^3 (T - T_V), \quad (10.4)$$

where α is the expansion coefficient. Assuming that the sliding mechanism process happens along a bridge of average number of units $\langle b \rangle$ and recalling the the individual process i are independent gives:

$$\tau/\tau_0 \sim \exp \left[\frac{1}{4} \langle b \rangle \omega_0^2 / v_f^2(T) \right]. \quad (10.5)$$

Since the logarithm of the normalized time τ/τ_0 does not change drastically around the effective glass transition, the expression in the square brackets in Eq. (10.5) is a constant. We can use this fact together with Eq. (10.4) to find:

$$T_g - T_V \propto \sqrt{\langle b \rangle}. \quad (10.6)$$

Introducing the film thickness h , and assuming that $\langle b \rangle \sim h^2$ – which is only valid for infinite ideal random walks – then leads to the affine trend with h in Eq. (10.1). We now aim at calculating the exact bridge-length distribution for finite-sized polymer chains, in order to investigate whether or not the M_w dependence in Eq. (10.1) can also be captured by the sliding model.

10.3 Bridge statistics

We consider a film made of a dense (supercooled) polymer melt consisting of identical chains, containing N monomers of size a (e.g. for polystyrene, one has a rescaled ideal monomeric size $a \approx 0.75$ nm) each. The film is assumed to be infinite in the (x, y) -plane, and to have two flat free interfaces located at the dimensionless vertical coordinates $z = 0$ and $z = H$ where $H = h/a$ is the nondimensional thickness of the sample. We define a bridge as a segment of a polymer chain that connects the two free interfaces, as shown in Fig. 10.2.

First, we are interested in the probability density of the dimensionless bridge length $B = b/a$, at a certain position z inside the film. We start by picking a monomer at a distance z from the lower interface. This monomer belongs to a polymer chain. From the position of the picked monomer, there are two branches of the polymer chain. As we deal with a (supercooled) polymer melt, these two branches can be properly described by Gaussian statistics [190]. For large N , in other words high molecular weight, one can invoke the continuous description of Brownian motion. As such, the probability density of the bridge length can be constructed using a constrained sum of the first-passage “times” of two Brownian motions. The polymer chain is of total length N , so that the test monomer considered above is at a distance P from one end of the chain, and at a distance $N - P$ from the other end (see Fig. 10.2), with P uniformly distributed in $[0, N]$. Denoting l_1 and l_2 the first-passage “times” of the chain from the test monomer to the $z = 0$ and $z = H$ interfaces, respectively, with $l_1 \leq P$ and $l_2 \leq N - P$, the bridge length reads $B = l_1 + l_2$. Therefore, the probability density $\rho(N, H, B, P, z)$ that a monomer located at a distance z from the bottom interface, and at position P along a chain of total length N , belongs to a bridge of length B , reads:

$$\rho = 2 \iint_{I_1 \times I_2} dl_1 dl_2 \delta(l_1 + l_2 - B) f_0(z, l_1) f_H(z, l_2), \quad (10.7)$$

with $I_1 = [0, P]$, $I_2 = [0, N - P]$, where the factor 2 accounts for the possibility of the two bridge subparts to be exchanged, and where $f_0(z, l_1)$ and $f_H(z, l_2)$ are the first-passage-time probability densities to the bottom and top interfaces, after “times” l_1 and l_2 , respectively, when starting at a distance z from the bottom interface. See the derivation in appendix 12.1. For a detailed review of the subject see [239]. By performing one of the

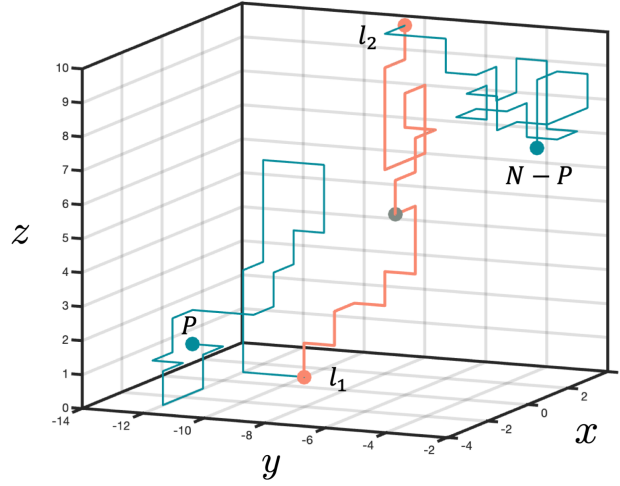


Figure 10.2: Sketch of the problem studied, as obtained from numerical simulation. We consider an ideal random walk with N steps in a box of dimensionless thickness $H = 10$ along the z -axis. A randomly chosen monomer (grey), located at an altitude z , is P steps away from one of the walk ends, and $N - P$ steps away from the other end. The chosen monomer is connected to both the $z = 0$ and $z = H$ interfaces, with paths of dimensionless lengths l_1 and l_2 , respectively, forming a bridge (orange) of dimensionless length $B = l_1 + l_2$. Another part (blue) of the random walk does not belong to the bridge.

two integrations, Eq. (10.7) becomes:

$$\rho = 2 \int_I dl f_0(z, l) f_H(z, B - l). \quad (10.8)$$

with $I = [\max(0, B - N + P), \min(B, P)]$. Then, uniformly averaging Eq. (10.8) with respect to P and z , gives the probability density $\bar{\rho}(N, H, B)$ that a randomly chosen monomer inside the film belongs to a bridge of length B , between 0 and N , as:

$$\bar{\rho} = \frac{4\pi^2 D^2 (N - B) B}{H^4 N} \sum_{k=1}^{\infty} k^2 (-1)^{k+1} e^{-D\lambda_k^2 B}, \quad (10.9)$$

where $\lambda_k = \frac{k\pi}{H}$ and $D = \frac{1}{2d}$, with $d = 3$ the space dimension. By integrating Eq. (10.9) over B , from 0 to N , one gets the fraction $\phi(N, H)$ of monomers belonging to bridges, as:

$$\phi = \frac{1}{3} - \frac{7H^2}{90DN} + \frac{4}{\pi^2} \sum_{k=1}^{\infty} \frac{(-1)^{k+1}}{k^2} e^{-D\lambda_k^2 N} \left(1 + \frac{2H^2}{\pi^2 DN k^2} \right), \quad (10.10)$$

where we note the expected diffusive-like self-similarity in the variable H/\sqrt{DN} . The limit $1/3$ at infinite N is intuitive, since any sub-part of the chain containing a given monomer then touches two interfaces, either twice the top one, or twice the bottom one, or once

each of the two interfaces, with equal chances.

We now turn to the central quantity of interest in this work, the average dimensionless bridge length $\langle B \rangle$, which is a function of N and H . The average bridge length is the first moment of the distribution:

$$\langle B \rangle = \frac{1}{\phi(N, H)} \int_0^N B \bar{\rho}(N, H, B) dB. \quad (10.11)$$

The integral can be evaluated exactly from Eq. (10.9), leading to:

$$\begin{aligned} \langle B \rangle = \frac{1}{\phi(N, H)} & \left[\frac{7H^2}{90D} - \frac{31H^4}{1260ND^2} \right. \\ & \left. + \frac{4N}{\pi^2} \sum_{k=1}^{\infty} \frac{(-1)^{k+1}}{k^2} u_k(N, H) e^{-D\lambda_k^2 N} \right], \end{aligned} \quad (10.12)$$

where, for convenience, we invoked the auxiliary function:

$$u_k = 1 + \frac{4H^2}{\pi^2 DN k^2} + \frac{6H^4}{\pi^4 D^2 N^2 k^4}. \quad (10.13)$$

By expanding Eq. (10.12), one finds in particular the large- N asymptotic behavior:

$$\langle B \rangle \simeq \frac{7H^2}{30D} - \frac{61H^4}{3150D^2N} + O\left(\frac{1}{N^2}\right), \quad (10.14)$$

that exhibits the $\langle B \rangle \sim H^2$ scaling invoked in the sliding model [234], as well as the first finite-size correction to it.

10.4 Finite-size sliding mechanism

We now examine the modification of the sliding mechanism for polymer chains of finite length. By plugging Eq. (10.12) into Eq. (10.6), one can get an exact expression for $T_g(H, N)$ from the sliding mechanism. Expanding the latter, one gets the large- N asymptotic behavior:

$$T_g - T_V \propto \frac{H}{\sqrt{D}} \left(1 - \frac{61H^2}{735DN} \right)^{1/2}. \quad (10.15)$$

In Fig. 10.3, we plot $\sqrt{\langle B \rangle}$ as a function of H , for different values of N , by numerically evaluating Eq. (10.12). While we recover the linear behaviour introduced in Ref. [234] in the strong-confinement regime, the leading term in the large- N asymptotics is independent of N . In other words – and even without discussing the intercept – the slope of the affine regime cannot exhibit the logarithmic-like dependence in N seen in the experiments [223, 225] (see Fig. 10.1 and Eq. (10.1)), preventing the current refined sliding mechanism from explaining them, even qualitatively. We stress that Eq. (10.12) is essentially of the form:

$$\langle B \rangle = \frac{H^2}{D} \mathcal{F}\left(\frac{H}{\sqrt{ND}}\right), \quad (10.16)$$

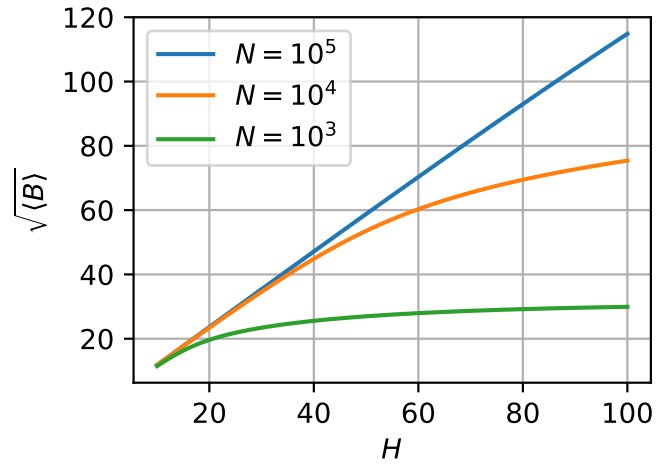


Figure 10.3: Square root of the average dimensionless bridge length $\langle B \rangle$ as a function of dimensionless film thickness H , for three chain lengths N , obtained from the numerical evaluation of Eq. (10.12) using a cut-off after 100 terms in the sum. The results have been checked to weakly depend on the cut-off value in this range.

with \mathcal{F} a scaling function, which, combined with Eq. (10.6), cannot lead to the factorized form of Eq. (10.1). We also stress that including loops in addition, or exclusively, does not help too, as all these types of paths can be seen under the same category of survival processes, and therefore exhibit a large- N saturation of their average lengths around the value of the film thickness.

Chapter 11

Perspective

11.1 Discussion

Examining our results from a broader perspective, the dependence on details such as the relaxation process along each bridge (Bernoulli trials in PGDG's [234] work and first exit time in Milner and Lipson's [236] delayed glassification model) or the choice of the free volume distribution in Eq. (10.2) is unsettling. Indeed, many other choices could have been made.

In an attempt to generalize our findings to some variations of the sliding mechanism, we assume that the relaxation time is of the general form:

$$\tau = \tau_0 \mathcal{H} \left[\langle B \rangle, \frac{a^3}{v_f(T)} \right], \quad (11.1)$$

where τ_0 is a reference time scale, and \mathcal{H} is an increasing function of both its arguments. Indeed, the relaxation time is expected to increase with increasing bridge length or decreasing free volume. Therefore, and because the effective glass-transition temperature T_g of a film is assumed to be reached when τ reaches the reference relaxation time of a bulk material at T_g^{bulk} [234], a relation of the following form must be satisfied:

$$v_f(T_g) = a^3 \mathcal{G}(\langle B \rangle), \quad (11.2)$$

where \mathcal{G} is an increasing function. In the sliding model [234], one has $\mathcal{G}(x) \propto \sqrt{x}$ for instance. For comparison, in the delayed-glassification model [236], one has $\mathcal{G}(x) \propto \log(x)$. As a side remark, a linear relation between free volume v_f and temperature T was assumed (see Eq. (10.4)), in view of thermal expansion in a sufficiently narrow temperature range, but we stress that any behavior of the form $v_f \sim (T - T_V)^\beta$ with a positive exponent β would lead to the same conclusion.

Let us now exhibit a necessary condition that should be satisfied by a model to ensure its applicability for describing experimental facts. The trends in Fig. (10.1) are consistent with Eq. (10.1), and a factor $f(M_w)$ slowly diverging with M_w [225]. Assuming the latter divergence to be true implies that:

$$\lim_{M_w \rightarrow \infty} \frac{\partial T_g}{\partial h} = +\infty. \quad (11.3)$$

Combining the latter equation with Eq. (10.4), and assuming T_V and α to be independent of h , leads to:

$$\lim_{N \rightarrow \infty} \frac{1}{a^3} \frac{\partial v_f(T_g)}{\partial H} = +\infty. \quad (11.4)$$

Finally, by combining Eq. (11.4) with Eq (11.2), one gets the requirement that:

$$\lim_{N \rightarrow \infty} \mathcal{G}'(\langle B \rangle) \frac{\partial \langle B \rangle}{\partial H} = +\infty. \quad (11.5)$$

However, from Eq. (10.14), we see that the left-hand side of Eq. (11.5) equals:

$$\lim_{N \rightarrow \infty} \mathcal{G}'(\langle B \rangle) \frac{\partial \langle B \rangle}{\partial H} = \frac{7H}{15D} \mathcal{G}' \left(\frac{7H^2}{30D} \right), \quad (11.6)$$

which is positive, but finite. Hence, even a generalized formulation of the sliding model following Eq. (11.1) cannot describe the experimental data. As a result, within the Gaussian framework, we can conclude that a different mechanism is needed to explain the M_w dependence of the T_g reductions in thin freestanding polymer films.

11.2 Proposed experiment

Here we propose a relatively simple experiment that can test the de Gennes Sliding mechanism. In the spirit of the experiments done by Forrest [203, 223]. Preparing pairs of samples of spin coated polystyrene film for ellipsometric measurements of T_g , as described in [203, 223]. Their thickness should be ranging between 200-300 nm and that are composed of polymer melt with molecular weight ranging between 0.5-1.2 Mg (10^6 g) . Thinner sample pairs would be ideal but to our best of knowledge, the samples becomes very fragile to manipulate.

From this point, before the measurement procedure, these sample pairs should be sandwiched and heated above the glass transition temperature for a short time compared with the reptation time [240], to allow the samples to adhere without having the individual polymers of each sample to penetrate too deeply into the other sample. This will guaranty that no path will link the two interfaces. At this stage the sample is ready to pass the same measurements of T_g as described in [203, 223] for free standing films. In case where the reduction in glass transition temperature would be statistically indistinguishable from the measurements in [223] (accounting for the double thickness) that would mean that the Sliding mechanism is indeed obsolete. Similar experiments have been done, but with a different measuring method, which does not allow us to compare to the data acquired previously [193].

11.3 Conclusion

We have computed in chapter 10 the probability density function of the bridge length in a thin film made of a dense equilibrium assembly of identical finite-sized polymer chains.

The calculations were performed in the Gaussian-chain framework. We have then used the obtained expressions in order to refine and critically discuss the sliding model for the anomalous glass transition in thin freestanding polymer films. Our analysis suggests that the sliding model, as well as similar models based on free-volume arguments, cannot capture the intricate chain-length dependence of the experimental data. Another key physical ingredient, with a dependence on the molecular weight, seems to be missing. Finally, there are two points to highlight as we think they justify further investigation: firstly, the remarkable stability of the films above the measured M_w -dependent T_g ; secondly, the proposed existence of a second T_g [193, 230], more closely associated with flow and the ways in which it is manifested in thin polymer films.

Chapter 12

Appendix – Part III

12.1 Exit probabilities

The probability that Brownian particle travels a path of length l , starting at z' and reaching an interface at $z = 0$, or at $z = h$, for the first time is called first passage density [239]. These random processes are well known and have been studied extensively. The first passage densities are computed directly from the density of paths of length l going from z' to z without touching the interfaces. This density is denoted $P_c(z, l|z', 0)$ and verifies the diffusion equation in single spatial dimension with absorbing boundary conditions in $z = 0$ and $z = h$:

$$\frac{dP_c}{dt} = D \frac{d^2}{dz^2} P_c \quad (12.1)$$

$$P_c(z = 0) = P_c(z = h) = 0, \quad (12.2)$$

with delta function initial condition located at z' , $P_c(z, 0|z', 0) = \delta(z - z')$. The solution of this partial differential equation is:

$$P_c(z, l|z', 0) = \frac{2}{h} \sum_{k=1}^{\infty} \sin(\lambda_k z') \sin(\lambda_k z) \exp(-D\lambda_k^2 l), \quad (12.3)$$

with $\lambda_k = \frac{\pi k}{h}$. The density of paths of length l reaching the interface for the first time is given by the probability flux at the edge given by Fick's law:

$$f_{edge} = -D \frac{dP_c}{dz} \Big|_{z=edge} . \quad (12.4)$$

Note that the sign should be chosen such that at each edge we look at the flux going out of the slab. Evaluating that gives:

$$f_0 = \frac{2D}{h} \sum_{k=1}^{\infty} \lambda_k \sin(\lambda_k z') \exp(-D\lambda_k^2 l), \quad (12.5)$$

and for the $z = h$ edge we get:

$$f_h = \frac{2D}{h} \sum_{k=1}^{\infty} (-1)^{k+1} \lambda_k \sin(\lambda_k z') \exp(-D\lambda_k^2 l), \quad (12.6)$$

which are the two probability densities that have been used in chapter 10.3.

Bibliography

- [1] R. K. Pathria and P. D. Beale. *Statistical Mechanics*. Elsevier, 2011.
- [2] H. E. Stanley. Scaling, universality, and renormalization: Three pillars of modern critical phenomena. *Reviews of Modern Physics*, 71(S6):S358, 1999.
- [3] A. Barrat, M. Barthelemy, and A. Vespignani. *Dynamical Processes on Complex Networks*. Cambridge University Press, 2008.
- [4] SM Klimenko, TI Tikchonenko, and VM Andreev. Packing of dna in the head of bacteriophage t2. *Journal of molecular biology*, 23(3):523–IN21, 1967.
- [5] Victor A Bloomfield. Dna condensation by multivalent cations. *Biopolymers: Original Research on Biomolecules*, 44(3):269–282, 1997.
- [6] Moshe Levy. Social phase transitions. *Journal of Economic Behavior & Organization*, 57(1):71–87, 2005.
- [7] Didier Sornette. *Critical phenomena in natural sciences: chaos, fractals, selforganization and disorder: concepts and tools*. Springer Science & Business Media, 2006.
- [8] Tamás Vicsek and Anna Zafeiris. Collective motion. *Physics Reports*, 517(3-4):71–140, 2012.
- [9] Haggai Bonneau, Vincent Démery, and Elie Raphaël. Temporal response of the conductivity of electrolytes. *Journal of Statistical Mechanics: Theory and Experiment*, 2023(7):073205, jul 2023.
- [10] Denis Dumont, Haggai Bonneau, Thomas Salez, Elie Raphael, and Pascal Damman. Microscopic foundation of the μ (i) rheology for dense granular flows on inclined planes. *Physical Review Research*, 5(1):013089, 2023.
- [11] Haggai Bonneau, Maxence Arutkin, Rainni Chen, James A Forrest, Elie Raphaël, and Thomas Salez. On the bridge hypothesis in the glass transition of freestanding polymer films. *The European Physical Journal E*, 46(3):8, 2023.
- [12] Luigi Galvani. De viribus electricitatis in motu musculari. commentarius. *De Bonoiensis Scientiarum et Artium Intituo atque Academie Commentarii*, 7:363–418, 1791.
- [13] Alessandro Volta. Xvii. on the electricity excited by the mere contact of conducting substances of different kinds. in a letter from mr. alexander volta, frs professor of

- natural philosophy in the university of pavia, to the rt. hon. sir joseph banks, bart. kbpr s. *Philosophical transactions of the Royal Society of London*, (90):403–431, 1800.
- [14] S. Arrhenius. Über die dissociation der in wasser gelösten stoffe. *Z. Phys. Chem.*, 1:631–648, 1887.
- [15] JH van't Hoff. Die rolle des osmotischen druckes in der analogie zwischen lösungen und gasen. *Zeitschrift für physikalische Chemie*, 1(1):481–508, 1887.
- [16] Francois-Marie Raoult. Loi générale des tensions de vapeur des dissolvants. *CR Hebd. Seances Acad. Sci*, 104:1430–1433, 1887.
- [17] Friedrich Wilhelm Georg Kohlrausch. *Das leitvermögen der elektrolyte, insbesondere der lösungen*. BG Teubner, 1898.
- [18] William Sutherland. Lxxv. a dynamical theory of diffusion for non-electrolytes and the molecular mass of albumin. *The London, Edinburgh, and Dublin Philosophical Magazine and Journal of Science*, 9(54):781–785, 1905.
- [19] NIELS Bjerrum. A new form for the electrolytic dissociation theory. In *Proceedings of the Seventh Internacional Congreso of Applied Chemistry Londres*, volume 27, pages 55–50, 1909.
- [20] P. Debye and E. Hückel. Theory of electrolytes—part II: law of the limit of electrolytic conduction. *Physikalische Zeitschrift*, 24:305–325, 1923.
- [21] L. Onsager. Report on a revision of the conductivity theory. *Transactions of the Faraday Society*, 23:341–349, 1927.
- [22] Niels Bjerrum. *Untersuchungen über Ionenassoziation*. AF Høst, 1926.
- [23] Raymond M Fuoss and Lars Onsager. Conductance of unassociated electrolytes. *The Journal of Physical Chemistry*, 61(5):668–682, 1957.
- [24] Lars Onsager and Shoon Kyung Kim. Wien Effect in Simple Strong Electrolytes. *The Journal of Physical Chemistry*, 61(2):198–215, 1957.
- [25] Margaret Robson Wright. *An introduction to aqueous electrolyte solutions*. John Wiley & Sons, 2007.
- [26] Y. Levin. Electrostatic correlations: from plasma to biology. *Rep. Prog. Phys.*, 65:1577, 2002.
- [27] Shamik Gupta and Stefano Ruffo. The world of long-range interactions: A bird's eye view. *International Journal of Modern Physics A*, 32(09):1741018, mar 2017.
- [28] Freddy Bouchet, Shamik Gupta, and David Mukamel. Thermodynamics and dynamics of systems with long-range interactions. *Physica A: Statistical Mechanics and its Applications*, 389(20):4389–4405, oct 2010.

-
- [29] Ramin Golestanian. Collective behavior of thermally active colloids. *Phys. Rev. Lett.*, 108:038303, Jan 2012.
- [30] L Onsager. Theory of electrolytes, i, *phys. Z*, 27:388–392, 1926.
- [31] JL Lebowitz and Elliott H Lieb. Existence of thermodynamics for real matter with coulomb forces. *Physical Review Letters*, 22(13):631, 1969.
- [32] Elliott H Lieb. The stability of matter. *Reviews of Modern Physics*, 48(4):553, 1976.
- [33] David C Brydges and Ph A Martin. Coulomb systems at low density: A review. *Journal of Statistical Physics*, 96:1163–1330, 1999.
- [34] Lars Onsager. Deviations from ohm’s law in weak electrolytes. *The Journal of chemical physics*, 2(9):599–615, 1934.
- [35] Ralf Blossey. *The Poisson-Boltzmann Equation: An Introduction*. Springer Nature, 2023.
- [36] David Andelman, Yoram Burak, and Henri Orland. *Electrostatic Interactions in Soft and Biological Matter: Ions, Membranes, Polymers and Colloids*. to be published.
- [37] Itamar Borukhov, David Andelman, and Henri Orland. Random polyelectrolytes and polyampholytes in solution. *The European Physical Journal B-Condensed Matter and Complex Systems*, 5:869–880, 1998.
- [38] Sahin Buyukdagli and Ralf Blossey. Beyond poisson–boltzmann: fluctuations and fluid structure in a self-consistent theory. *Journal of Physics: Condensed Matter*, 28(34):343001, 2016.
- [39] Roland R Netz and Henri Orland. Beyond poisson-boltzmann: Fluctuation effects and correlation functions. *The European Physical Journal E*, 1:203–214, 2000.
- [40] John O’M Bockris, Amulya KN Reddy, and Maria E Gamboa-Adelco. *Modern Electrochemistry Vol. 1*. Springer, 2006.
- [41] David Andelman. Introduction to electrostatics in soft and biological matter. *Soft condensed matter physics in molecular and cell biology*, 6:97–122, 2006.
- [42] Martin Z Bazant, Katsuyo Thornton, and Armand Ajdari. Diffuse-charge dynamics in electrochemical systems. *Physical review E*, 70(2):021506, 2004.
- [43] Todd M Squires and Martin Z Bazant. Induced-charge electro-osmosis. *Journal of Fluid Mechanics*, 509:217–252, 2004.
- [44] Laurent Joly, Christophe Ybert, Emmanuel Trizac, and Lydéric Bocquet. Hydrodynamics within the electric double layer on slipping surfaces. *Physical review letters*, 93(25):257805, 2004.

- [45] Yuki Uematsu and Takeaki Araki. Electro-osmotic flow of semidilute polyelectrolyte solutions. *The Journal of chemical physics*, 139(9):094901, 2013.
- [46] John L Anderson. Colloid transport by interfacial forces. *Annual review of fluid mechanics*, 21(1):61–99, 1989.
- [47] Alessandro Siria, Philippe Poncharal, Anne-Laure Biance, Rémy Fulcrand, Xavier Blase, Stephen T Purcell, and Lydéric Bocquet. Giant osmotic energy conversion measured in a single transmembrane boron nitride nanotube. *Nature*, 494(7438):455–458, 2013.
- [48] Kang Kim, Yasuya Nakayama, and Ryoichi Yamamoto. Direct numerical simulations of electrophoresis of charged colloids. *Physical review letters*, 96(20):208302, 2006.
- [49] SR Maduar, AV Belyaev, V Lobaskin, and OI Vinogradova. Electrohydrodynamics near hydrophobic surfaces. *Physical review letters*, 114(11):118301, 2015.
- [50] Vladimir Lobaskin, Burkhard Dünweg, Martin Medebach, Thomas Palberg, and Christian Holm. Electrophoresis of colloidal dispersions in the low-salt regime. *Physical Review Letters*, 98(17):176105, 2007.
- [51] Umberto Marini Bettolo Marconi, Simone Melchionna, and Ignacio Pagonabarraga. Effective electrodiffusion equation for non-uniform nanochannels. *The Journal of chemical physics*, 138(24), 2013.
- [52] William M Haynes. *CRC handbook of chemistry and physics*. CRC press, 2016.
- [53] David S. Dean. Langevin equation for the density of a system of interacting Langevin processes. *Journal of Physics A: Mathematical and General*, 29(24):L613–L617, 1996.
- [54] Kyozi Kawasaki. Stochastic model of slow dynamics in supercooled liquids and dense colloidal suspensions. *Physica A: Statistical Mechanics and its Applications*, 208(1):35–64, 1994.
- [55] Michael te Vrugt, Hartmut Löwen, and Raphael Wittkowski. Classical dynamical density functional theory: from fundamentals to applications. *Advances in Physics*, 69(2):121–247, 2020.
- [56] Antonio Russo, Sergio P Perez, Miguel A Durán-Olivencia, Peter Yatsyshin, José A Carrillo, and Serafim Kalliadasis. A finite-volume method for fluctuating dynamical density functional theory. *Journal of Computational Physics*, 428:109796, 2021.
- [57] Umberto Marini Bettolo Marconi and Pedro Tarazona. Dynamic density functional theory of fluids. *The Journal of chemical physics*, 110(16):8032–8044, 1999.
- [58] B. Øksendal. *Stochastic differential equations: an introduction with applications*. Springer, 5th edition, 2000.

-
- [59] John Happel and Howard Brenner. *Low Reynolds number hydrodynamics: with special applications to particulate media*, volume 1. Springer Science & Business Media, 1983.
- [60] V. Démery and D. S. Dean. The conductivity of strong electrolytes from stochastic density functional theory. *Journal of Statistical Mechanics: Theory and Experiment*, 2016(2):023106, 2016.
- [61] Jean-Philippe Péraud, Andrew J. Nonaka, John B. Bell, Aleksandar Donev, and Alejandro L. Garcia. Fluctuation-enhanced electric conductivity in electrolyte solutions. *Proceedings of the National Academy of Sciences*, 114(41):10829–10833, 2017.
- [62] Aleksandar Donev, Alejandro L. Garcia, Jean-Philippe Péraud, Andrew J. Nonaka, and John B. Bell. Fluctuating Hydrodynamics and Debye-Hückel-Onsager Theory for Electrolytes. *Current Opinion in Electrochemistry*, 13:1–10, 2019.
- [63] Yael Avni, Ram M. Adar, David Andelman, and Henri Orland. Conductivity of concentrated electrolytes. *Phys. Rev. Lett.*, 128:098002, Mar 2022.
- [64] Yael Avni, David Andelman, and Henri Orland. Conductance of concentrated electrolytes: Multivalency and the wien effect. *The Journal of Chemical Physics*, 157(15):154502, 2022.
- [65] Ram M Adar, Samuel A Safran, Haim Diamant, and David Andelman. Screening length for finite-size ions in concentrated electrolytes. *Physical Review E*, 100(4):042615, 2019.
- [66] Saeed Mahdisoltani and Ramin Golestanian. Long-Range Fluctuation-Induced Forces in Driven Electrolytes. *Phys. Rev. Lett.*, 126(15):158002, Apr 2021.
- [67] V. Kaiser, S. T. Bramwell, P. C. W. Holdsworth, and R. Moessner. Onsager’s Wien effect on a lattice. *Nat Mater*, 12(11):1033–1037, 11 2013. Letter.
- [68] Dominika Lesnicki, Chloe Y. Gao, Benjamin Rotenberg, and David T. Limmer. Field-dependent ionic conductivities from generalized fluctuation-dissipation relations. *Phys. Rev. Lett.*, 124:206001, May 2020.
- [69] Dominika Lesnicki, Chloe Y. Gao, David T. Limmer, and Benjamin Rotenberg. On the molecular correlations that result in field-dependent conductivities in electrolyte solutions. *The Journal of Chemical Physics*, 155(1):014507, 2021.
- [70] Alexis Poncet, Olivier Bénichou, Vincent Démery, and Gleb Oshanin. Universal long ranged correlations in driven binary mixtures. *Physical review letters*, 118(11):118002, 2017.
- [71] Łukasz Richter, Paweł J. Żuk, Piotr Szymczak, Jan Paczesny, Krzysztof M. Bąk, Tomasz Szymborski, Piotr Garstecki, Howard A. Stone, Robert Hołyst, and Carlos

- Drummond. Ions in an AC Electric Field: Strong Long-Range Repulsion between Oppositely Charged Surfaces. *Phys. Rev. Lett.*, 125(5):056001, Jul 2020.
- [72] Paul Robin, Nikita Kavokine, and Lydéric Bocquet. Modeling of emergent memory and voltage spiking in ionic transport through angstrom-scale slits. *Science*, 373(6555):687–691, 2021.
- [73] P. Robin, T. Emmerich, A. Ismail, A. Niguès, Y. You, G.-H. Nam, A. Keerthi, A. Siria, A. K. Geim, B. Radha, and L. Bocquet. Long-term memory and synapse-like dynamics in two-dimensional nanofluidic channels. *Science*, 379(6628):161–167, 2023.
- [74] Saeed Mahdisoltani and Ramin Golestanian. Transient fluctuation-induced forces in driven electrolytes after an electric field quench. *New Journal of Physics*, 23(7):073034, jul 2021.
- [75] David S. Dean, Vincent Démery, V. Adrian Parsegian, and Rudolf Podgornik. Out-of-equilibrium relaxation of the thermal Casimir effect in a model polarizable material. *Phys. Rev. E*, 85(3):031108, 2012.
- [76] David S. Dean and Rudolf Podgornik. Relaxation of the thermal Casimir force between net neutral plates containing Brownian charges. *Phys. Rev. E*, 89(3):032117, Mar 2014.
- [77] Jose M Ortiz De Zarate and Jan V Sengers. *Hydrodynamic fluctuations in fluids and fluid mixtures*. Elsevier, 2006.
- [78] Sangtae Kim and Seppo J Karrila. *Microhydrodynamics: principles and selected applications*. Courier Corporation, 2013.
- [79] Dorian Brogioli and Alberto Vailati. Diffusive mass transfer by nonequilibrium fluctuations: Fick’s law revisited. *Phys. Rev. E*, 63:012105, Dec 2000.
- [80] Crispin Gardiner. *Stochastic methods*. Springer Berlin, 2009.
- [81] Maximilian Behr, Peter Benner, and Jan Heiland. Solution formulas for differential Sylvester and Lyapunov equations. *Calcolo*, 56(4):51, 2019.
- [82] Robert Piessens, Elise de Doncker-Kapenga, Christoph W Überhuber, and David K Kahaner. *Quadpack: a subroutine package for automatic integration*, volume 1. Springer Science & Business Media, 2012.
- [83] Pauli Virtanen, Ralf Gommers, Travis E. Oliphant, Matt Haberland, Tyler Reddy, David Cournapeau, Evgeni Burovski, Pearu Peterson, Warren Weckesser, Jonathan Bright, Stéfan J. van der Walt, Matthew Brett, Joshua Wilson, K. Jarrod Millman, Nikolay Mayorov, Andrew R. J. Nelson, Eric Jones, Robert Kern, Eric Larson, C J Carey, İlhan Polat, Yu Feng, Eric W. Moore, Jake VanderPlas, Denis Laxalde, Josef Perktold, Robert Cimrman, Ian Henriksen, E. A. Quintero, Charles R. Harris,

- Anne M. Archibald, Antônio H. Ribeiro, Fabian Pedregosa, Paul van Mulbregt, and SciPy 1.0 Contributors. SciPy 1.0: Fundamental Algorithms for Scientific Computing in Python. *Nature Methods*, 17:261–272, 2020.
- [84] Jean-Pierre Hansen and Ian Ranald McDonald. *Theory of simple liquids: with applications to soft matter*. Academic press, 2013.
- [85] Lars Onsager. Electrostatic interaction of molecules. *Journal of Physical Chemistry*, 43(2):189–196, 1939.
- [86] Nikita Kavokine, Paul Robin, and Lydéric Bocquet. Interaction confinement and electronic screening in two-dimensional nanofluidic channels. *The Journal of Chemical Physics*, 157(11), 2022.
- [87] Manoel Manghi, John Palmeri, Francois Henn, Adrien Noury, Fabien Picaud, Guillaume Herlem, and Vincent Jourdain. Ionic conductance of carbon nanotubes: confronting literature data with nanofluidic theory. *The Journal of Physical Chemistry C*, 125(42):22943–22950, 2021.
- [88] Olivier Bernard, Marie Jardat, Benjamin Rotenberg, and Pierre Illien. On analytical theories for conductivity and self-diffusion in concentrated electrolytes. *arXiv preprint arXiv:2306.16737*, 2023.
- [89] Paul Robin, Mathieu Lizée, Qian Yang, Théo Emmerich, Alessandro Siria, and Lydéric Bocquet. Disentangling 1/f noise from confined ion dynamics. *Faraday Discussions*, 2023.
- [90] Benjamin Rotenberg, Sophie Marbach, et al. Ionic fluctuations in finite volumes: fractional noise and hyperuniformity. *Faraday Discussions*, 2023.
- [91] Bruno Andreotti, Yoël Forterre, and Olivier Pouliquen. *Granular media: between fluid and solid*. Cambridge University Press, 2013.
- [92] Matthias Sperl. Experiments on corn pressure in silo cells—translation and comment of janssen’s paper from 1895. *Granular Matter*, 8(2):59–65, 2006.
- [93] G Ovarlez, C Fond, and E Clément. Overshoot effect in the janssen granular column: a crucial test for granular mechanics. *Physical Review E*, 67(6):060302, 2003.
- [94] Peter Schall and Martin Van Hecke. Shear bands in matter with granularity. *Annual Review of Fluid Mechanics*, 42:67–88, 2010.
- [95] Alexandre Kabla and Georges Debrégeas. Local stress relaxation and shear banding in a dry foam under shear. *Physical review letters*, 90(25):258303, 2003.
- [96] Anthony Rosato, Katherine J Strandburg, Friedrich Prinz, and Robert H Swendsen. Why the brazil nuts are on top: Size segregation of particulate matter by shaking. *Physical review letters*, 58(10):1038, 1987.

- [97] Aaron S Keys, Adam R Abate, Sharon C Glotzer, and Douglas J Durian. Measurement of growing dynamical length scales and prediction of the jamming transition in a granular material. *Nature physics*, 3(4):260–264, 2007.
- [98] Andrea J Liu and Sidney R Nagel. The jamming transition and the marginally jammed solid. *Annu. Rev. Condens. Matter Phys.*, 1(1):347–369, 2010.
- [99] Ken Sakaie, Denis Fenistein, Timothy J Carroll, Martin van Hecke, and Paul Umbanhowar. Mr imaging of reynolds dilatancy in the bulk of smooth granular flows. *Europhysics Letters*, 84(3):38001, 2008.
- [100] GDR MiDi gdrmidi@ polytech. univ-mrs. fr <http://www.lmgc.univ-montp2.fr/MIDI/>. On dense granular flows. *The European Physical Journal E*, 14:341–365, 2004.
- [101] Pierre Jop, Yoël Forterre, and Olivier Pouliquen. A constitutive law for dense granular flows. *Nature*, 441(7094):727–730, 2006.
- [102] J-P Bouchaud, Michael E Cates, J Ravi Prakash, and Sam F Edwards. A model for the dynamics of sandpile surfaces. *Journal de Physique I*, 4(10):1383–1410, 1994.
- [103] Mehdi Bouzid, Adrien Izzet, Martin Trulsson, Eric Clément, Philippe Claudin, and Bruno Andreotti. Non-local rheology in dense granular flows: Revisiting the concept of fluidity. *The European Physical Journal E*, 38:1–15, 2015.
- [104] Ken Kamrin. Non-locality in granular flow: Phenomenology and modeling approaches. *Frontiers in Physics*, 7:116, 2019.
- [105] Leonardo E Silbert, James W Landry, and Gary S Grest. Granular flow down a rough inclined plane: transition between thin and thick piles. *Physics of Fluids*, 15(1):1–10, 2003.
- [106] Yoël Forterre and Olivier Pouliquen. Long-surface-wave instability in dense granular flows. *Journal of Fluid Mechanics*, 486:21–50, 2003.
- [107] Olivier Pouliquen. Scaling laws in granular flows down rough inclined planes. *Physics of fluids*, 11(3):542–548, 1999.
- [108] Tamás Börzsönyi, Thomas C Halsey, and Robert E Ecke. Avalanche dynamics on a rough inclined plane. *Physical Review E*, 78(1):011306, 2008.
- [109] F Malloggi, Bruno Andreotti, and E Clément. Nonlocal effects in sand flows on an inclined plane. *Physical Review E*, 91(5):052202, 2015.
- [110] Hugo Perrin, Matthieu Wyart, Bloen Metzger, and Yoel Forterre. Nonlocal effects reflect the jamming criticality in frictionless granular flows down inclines. *Physical Review Letters*, 126(22):228002, 2021.

-
- [111] Mehdi Bouzid, Martin Trulsson, Philippe Claudin, Eric Clément, and Bruno Andreotti. Nonlocal rheology of granular flows across yield conditions. *Physical review letters*, 111(23):238301, 2013.
- [112] Ken Kamrin and Georg Koval. Nonlocal constitutive relation for steady granular flow. *Physical review letters*, 108(17):178301, 2012.
- [113] Julie Goyon, Annie Colin, G Ovarlez, A Ajdari, and L Bocquet. Spatial cooperativity in soft glassy flows. *Nature*, 454(7200):84–87, 2008.
- [114] David L Henann and Ken Kamrin. A predictive, size-dependent continuum model for dense granular flows. *Proceedings of the National Academy of Sciences*, 110(17):6730–6735, 2013.
- [115] Zhu Tang, Theodore A Brzinski, Michael Shearer, and Karen E Daniels. Nonlocal rheology of dense granular flow in annular shear experiments. *Soft matter*, 14(16):3040–3048, 2018.
- [116] Kuniyasu Saitoh and Brian P Tighe. Nonlocal effects in inhomogeneous flows of soft athermal disks. *Physical review letters*, 122(18):188001, 2019.
- [117] Ken Kamrin and David L Henann. Nonlocal modeling of granular flows down inclines. *Soft matter*, 11(1):179–185, 2015.
- [118] Denis Dumont, Pierre Soulard, Thomas Salez, Elie Raphaël, and Pascal Damman. Microscopic picture of erosion and sedimentation processes in dense granular flows. *Physical Review Letters*, 125(20):208002, 2020.
- [119] Heinrich M Jaeger, Sidney R Nagel, and Robert P Behringer. Granular solids, liquids, and gases. *Reviews of modern physics*, 68(4):1259, 1996.
- [120] Yoël Forterre and Olivier Pouliquen. Flows of dense granular media. *Annu. Rev. Fluid Mech.*, 40:1–24, 2008.
- [121] Abhinendra Singh, Christopher Ness, Ryohei Seto, Juan J de Pablo, and Heinrich M Jaeger. Shear thickening and jamming of dense suspensions: the “roll” of friction. *Physical Review Letters*, 124(24):248005, 2020.
- [122] Nicolas Estrada, Alfredo Taboada, and Farhang Radjai. Shear strength and force transmission in granular media with rolling resistance. *Physical Review E*, 78(2):021301, 2008.
- [123] BM Guy, JA Richards, DJM Hodgson, E Blanco, and WCK Poon. Constraint-based approach to granular dispersion rheology. *Physical review letters*, 121(12):128001, 2018.
- [124] Maurice A Carrigy. Experiments on the angles of repose of granular materials 1. *Sedimentology*, 14(3-4):147–158, 1970.

- [125] Hugo Perrin, Cécile Clavaud, Matthieu Wyart, Bloen Metzger, and Yoël Forterre. Interparticle friction leads to nonmonotonic flow curves and hysteresis in viscous suspensions. *Physical Review X*, 9(3):031027, 2019.
- [126] Daniel Howell, Robert P Behringer, and Christian Veje. Stress fluctuations in a 2d granular couette experiment: a continuous transition. *Physical Review Letters*, 82(26):5241, 1999.
- [127] C-h Liu, Sydney R Nagel, DA Schecter, SN Coppersmith, Satya Majumdar, Onuttom Narayan, and TA Witten. Force fluctuations in bead packs. *Science*, 269(5223):513–515, 1995.
- [128] Sam F Edwards and RBS Oakeshott. Theory of powders. *Physica A: Statistical Mechanics and its Applications*, 157(3):1080–1090, 1989.
- [129] Dapeng Bi, Silke Henkes, Karen E Daniels, and Bulbul Chakraborty. The statistical physics of athermal materials. *Annu. Rev. Condens. Matter Phys.*, 6(1):63–83, 2015.
- [130] Ephraim S Bililign, Jonathan E Kollmer, and Karen E Daniels. Protocol dependence and state variables in the force-moment ensemble. *Physical review letters*, 122(3):038001, 2019.
- [131] Stefano Martiniani, K Julian Schrenk, Kabir Ramola, Bulbul Chakraborty, and Daan Frenkel. Numerical test of the edwards conjecture shows that all packings are equally probable at jamming. *Nature physics*, 13(9):848–851, 2017.
- [132] Ye Yuan, Yi Xing, Jie Zheng, Zhifeng Li, Houfei Yuan, Shuyang Zhang, Zhikun Zeng, Chengjie Xia, Hua Tong, Walter Kob, et al. Experimental test of the edwards volume ensemble for tapped granular packings. *Physical Review Letters*, 127(1):018002, 2021.
- [133] Stephen Corteen Cowin and Masao Satake. Continuum mechanical and statistical approaches in the mechanics of granular materials. *Journal of Rheology*, 23(2):243–256, 1979.
- [134] AM Taylor-Noonan, D Gollin, ET Bowman, and WA Take. The influence of image analysis methodology on the calculation of granular temperature for granular flows. *Granular Matter*, 23(4):96, 2021.
- [135] Veronique Trappe, V Prasad, Luca Cipelletti, PN Segre, and David A Weitz. Jamming phase diagram for attractive particles. *Nature*, 411(6839):772–775, 2001.
- [136] Gijs Katgert, Brian P Tighe, and Martin van Hecke. The jamming perspective on wet foams. *Soft Matter*, 9(41):9739–9746, 2013.
- [137] Étienne Fodor and M Cristina Marchetti. The statistical physics of active matter: From self-catalytic colloids to living cells. *Physica A: Statistical Mechanics and its Applications*, 504:106–120, 2018.

-
- [138] Dapeng Bi, Xingbo Yang, M Cristina Marchetti, and M Lisa Manning. Motility-driven glass and jamming transitions in biological tissues. *Physical Review X*, 6(2):021011, 2016.
- [139] Giorgio Parisi and Francesco Zamponi. Mean-field theory of hard sphere glasses and jamming. *Reviews of Modern Physics*, 82(1):789, 2010.
- [140] Ludovic Berthier and Giulio Biroli. Theoretical perspective on the glass transition and amorphous materials. *Reviews of modern physics*, 83(2):587, 2011.
- [141] Andrea J Liu and Sidney R Nagel. Jamming is not just cool any more. *Nature*, 396(6706):21–22, 1998.
- [142] Daniel Bonn, Morton M Denn, Ludovic Berthier, Thibaut Divoux, and Sébastien Manneville. Yield stress materials in soft condensed matter. *Reviews of Modern Physics*, 89(3):035005, 2017.
- [143] Atsushi Ikeda, Ludovic Berthier, and Peter Sollich. Disentangling glass and jamming physics in the rheology of soft materials. *Soft Matter*, 9(32):7669–7683, 2013.
- [144] Atsushi Ikeda, Ludovic Berthier, and Peter Sollich. Unified study of glass and jamming rheology in soft particle systems. *Physical review letters*, 109(1):018301, 2012.
- [145] Salvatore Torquato and Frank H Stillinger. Jammed hard-particle packings: From kepler to bernal and beyond. *Reviews of modern physics*, 82(3):2633, 2010.
- [146] Adrian Baule, Flaviano Morone, Hans J Herrmann, and Hernán A Makse. Edwards statistical mechanics for jammed granular matter. *Reviews of modern physics*, 90(1):015006, 2018.
- [147] Robert P Behringer and Bulbul Chakraborty. The physics of jamming for granular materials: a review. *Reports on Progress in Physics*, 82(1):012601, 2018.
- [148] Osborne Reynolds. On the dilatancy of media composed of rigid particles in contact, with experimental illustration. *Philosophical Magazine, Series 5*, 20:469–481, 1885.
- [149] Pierre-Emmanuel Peyneau and Jean-Noël Roux. Frictionless bead packs have macroscopic friction, but no dilatancy. *Physical review E*, 78(1):011307, 2008.
- [150] Peidong Yu, Matthias Schröter, and Matthias Sperl. Velocity distribution of a homogeneously cooling granular gas. *Physical Review Letters*, 124(20):208007, 2020.
- [151] Nikolai V Brilliantov and Thorsten Pöschel. *Kinetic theory of granular gases*. Oxford University Press on Demand, 2004.
- [152] Oleh Baran, Deniz Ertas, Thomas C Halsey, Gary S Grest, and Jeremy B Lechman. Velocity correlations in dense gravity-driven granular chute flow. *Physical Review E*, 74(5):051302, 2006.

- [153] Leonardo E Silbert, Deniz Ertas, Gary S Grest, Thomas C Halsey, Dov Levine, and Steven J Plimpton. Granular flow down an inclined plane: Bagnold scaling and rheology. *Physical Review E*, 64(5):051302, 2001.
- [154] Jean Rajchenbach. Flow in powders: From discrete avalanches to continuous regime. *Physical Review Letters*, 65(18):2221, 1990.
- [155] Ralph Alger Bagnold. Experiments on a gravity-free dispersion of large solid spheres in a newtonian fluid under shear. *Proceedings of the Royal Society of London. Series A. Mathematical and Physical Sciences*, 225(1160):49–63, 1954.
- [156] Christoph Kloss, Christoph Goniva, Alice Hager, Stefan Amberger, and Stefan Pirker. Models, algorithms and validation for opensource dem and cfd-dem. *Progress in Computational Fluid Dynamics, an International Journal*, 12(2-3):140–152, 2012.
- [157] Pierre Jop, Yoël Forterre, and Olivier Pouliquen. Crucial role of sidewalls in granular surface flows: consequences for the rheology. *Journal of fluid mechanics*, 541:167–192, 2005.
- [158] Emilien Azéma and Farhang Radjai. Internal structure of inertial granular flows. *Physical review letters*, 112(7):078001, 2014.
- [159] Liuchi Li and José E Andrade. Identifying spatial transitions in heterogenous granular flow. *Granular Matter*, 22(2):52, 2020.
- [160] Frédéric Da Cruz, Sacha Emam, Michaël Prochnow, Jean-Noël Roux, and François Chevoir. Rheophysics of dense granular materials: Discrete simulation of plane shear flows. *Physical Review E*, 72(2):021309, 2005.
- [161] Gregg Lois, Anaël Lemaître, and Jean M Carlson. Numerical tests of constitutive laws for dense granular flows. *Physical Review E*, 72(5):051303, 2005.
- [162] Pierre-Emmanuel Peyneau and Jean-Noël Roux. Solidlike behavior and anisotropy in rigid frictionless bead assemblies. *Physical Review E*, 78(4):041307, 2008.
- [163] Olivier Pouliquen, Cyril Cassar, Pierre Jop, Yoel Forterre, and Maxime Nicolas. Flow of dense granular material: towards simple constitutive laws. *Journal of Statistical Mechanics: Theory and Experiment*, 2006(07):P07020, 2006.
- [164] Prashidha Kharel and Pierre Rognon. Vortices enhance diffusion in dense granular flows. *Physical review letters*, 119(17):178001, 2017.
- [165] Kuniyasu Saitoh and Takeshi Kawasaki. Critical scaling of diffusion coefficients and size of rigid clusters of soft athermal particles under shear. *Frontiers in Physics*, 8:99, 2020.
- [166] E DeGiuli, Gustavo Düring, E Lerner, and M Wyart. Unified theory of inertial granular flows and non-brownian suspensions. *Physical Review E*, 91(6):062206, 2015.

-
- [167] E DeGiuli, JN McElwaine, and M Wyart. Phase diagram for inertial granular flows. *Physical Review E*, 94(1):012904, 2016.
- [168] Smarajit Karmakar, Chandan Dasgupta, and Srikanth Sastry. Growing length scales and their relation to timescales in glass-forming liquids. *Annu. Rev. Condens. Matter Phys.*, 5(1):255–284, 2014.
- [169] Thomas Salez, Justin Salez, Kari Dalnoki-Veress, Elie Raphaël, and James A Forrest. Cooperative strings and glassy interfaces. *Proceedings of the National Academy of Sciences*, 112(27):8227–8231, 2015.
- [170] Daniel Vågberg, Peter Olsson, and S Teitel. Critical scaling of bagnold rheology at the jamming transition of frictionless two-dimensional disks. *Physical Review E*, 93(5):052902, 2016.
- [171] Daniel Vågberg, Peter Olsson, and S Teitel. Shear banding, discontinuous shear thickening, and rheological phase transitions in athermally sheared frictionless disks. *Physical Review E*, 95(5):052903, 2017.
- [172] Chandana Mondal, Michael Moshe, Itamar Procaccia, Saikat Roy, Jin Shang, and Jie Zhang. Experimental and numerical verification of anomalous screening theory in granular matter. *Chaos, Solitons & Fractals*, 164:112609, 2022.
- [173] Noemie S Livne, Amit Schiller, and Michael Moshe. Geometric theory of mechanical screening in two-dimensional solids. *Physical Review E*, 107(5):055004, 2023.
- [174] H Vogel. The law of the relationship between viscosity of liquids and the temperature phys. *Phys. Z*, 1921.
- [175] Gordon S Fulcher. Analysis of recent measurements of the viscosity of glasses. *Journal of the American Ceramic Society*, 8(6):339–355, 1925.
- [176] GHWZ Tammann and W Hesse. Die abhängigkeit der viscosität von der temperatur bie unterkühlten flüssigkeiten. *Zeitschrift für anorganische und allgemeine Chemie*, 156(1):245–257, 1926.
- [177] Malcolm L Williams, Robert F Landel, and John D Ferry. The temperature dependence of relaxation mechanisms in amorphous polymers and other glass-forming liquids. *Journal of the American Chemical society*, 77(14):3701–3707, 1955.
- [178] C Austen Angell. Formation of glasses from liquids and biopolymers. *Science*, 267(5206):1924–1935, 1995.
- [179] MD Ediger and Peter Harrowell. Perspective: Supercooled liquids and glasses. *The Journal of chemical physics*, 137(8):080901, 2012.
- [180] Giorgio Parisi, Pierfrancesco Urbani, and Francesco Zamponi. *Theory of simple glasses: exact solutions in infinite dimensions*. Cambridge University Press, 2020.

- [181] Philip W Anderson. Through the glass lightly. *Science*, 267(5204):1615–1616, 1995.
- [182] J Jackle. Models of the glass transition. *Reports on Progress in Physics*, 49(2):171, 1986.
- [183] Hans Sillescu. Heterogeneity at the glass transition: a review. *Journal of Non-Crystalline Solids*, 243(2-3):81–108, 1999.
- [184] Ole Peters. The ergodicity problem in economics. *Nature Physics*, 15(12):1216–1221, 2019.
- [185] Gerold Adam and Julian H Gibbs. On the temperature dependence of cooperative relaxation properties in glass-forming liquids. *The journal of chemical physics*, 43(1):139–146, 1965.
- [186] Theodore R Kirkpatrick, Devarajan Thirumalai, and Peter G Wolynes. Scaling concepts for the dynamics of viscous liquids near an ideal glassy state. *Physical Review A*, 40(2):1045, 1989.
- [187] Vassiliy Lubchenko and Peter G Wolynes. Theory of structural glasses and super-cooled liquids. *Annu. Rev. Phys. Chem.*, 58:235–266, 2007.
- [188] Jacek Dudowicz, Karl F Freed, and Jack F Douglas. Generalized entropy theory of polymer glass formation. *Advances in Chemical Physics*, 137:125, 2008.
- [189] Ranko Richert and CA Angell. Dynamics of glass-forming liquids. v. on the link between molecular dynamics and configurational entropy. *The Journal of chemical physics*, 108(21):9016–9026, 1998.
- [190] Masao Doi and Samuel Frederick Edwards. *The theory of polymer dynamics*, volume 73. oxford university press, 1988.
- [191] Pierre-Gilles De Gennes. *Scaling concepts in polymer physics*. Cornell university press, 1979.
- [192] Paul J Flory. The configuration of real polymer chains. *The Journal of Chemical Physics*, 17(3):303–310, 1949.
- [193] Connie B Roth. *Polymer glasses*. CRC Press, 2016.
- [194] Simone Napolitano, Emmanouil Glynos, and Nicholas B Tito. Glass transition of polymers in bulk, confined geometries, and near interfaces. *Reports on Progress in Physics*, 80(3):036602, 2017.
- [195] E Donth. Characteristic length of the glass transition. *Journal of Polymer Science Part B: Polymer Physics*, 34(17):2881–2892, 1996.

-
- [196] Jacob D Stevenson, Jörg Schmalian, and Peter G Wolynes. The shapes of cooperatively rearranging regions in glass-forming liquids. *Nature Physics*, 2(4):268–274, 2006.
- [197] Zexin Zhang, Peter J Yunker, Piotr Habdas, and AG Yodh. Cooperative rearrangement regions and dynamical heterogeneities in colloidal glasses with attractive versus repulsive interactions. *Physical review letters*, 107(20):208303, 2011.
- [198] Jan Bares. Glass transition of the polymer microphase. *Macromolecules*, 8(2):244–246, 1975.
- [199] Catheryn L Jackson and Gregory B McKenna. The melting behavior of organic materials confined in porous solids. *The Journal of Chemical Physics*, 93(12):9002–9011, 1990.
- [200] Peter Scheidler, Walter Kob, and Kurt Binder. The relaxation dynamics of a simple glass former confined in a pore. *Europhysics Letters*, 52(3):277, 2000.
- [201] Ludovic Berthier. Finite-size scaling analysis of the glass transition. *Physical review letters*, 91(5):055701, 2003.
- [202] Joseph L Keddie, Richard AL Jones, and Rachel A Cory. Size-dependent depression of the glass transition temperature in polymer films. *Europhysics letters*, 27(1):59, 1994.
- [203] JA Forrest, K Dalnoki-Veress, JR Stevens, and JR Dutcher. Effect of free surfaces on the glass transition temperature of thin polymer films. *Physical review letters*, 77(10):2002, 1996.
- [204] F Varnik, J Baschnagel, and K Binder. Reduction of the glass transition temperature in polymer films: A molecular-dynamics study. *Physical Review E*, 65(2):021507, 2002.
- [205] Christopher J Ellison and John M Torkelson. The distribution of glass-transition temperatures in nanoscopically confined glass formers. *Nature materials*, 2(10):695–700, 2003.
- [206] J Baschnagel and F Varnik. Computer simulations of supercooled polymer melts in the bulk and in confined geometry. *Journal of Physics: Condensed Matter*, 17(32):R851, 2005.
- [207] Mataz Alcoutlabi and Gregory B McKenna. Effects of confinement on material behaviour at the nanometre size scale. *Journal of Physics: Condensed Matter*, 17(15):R461, 2005.
- [208] Z Fakhraai and JA Forrest. Measuring the surface dynamics of glassy polymers. *Science*, 319(5863):600–604, 2008.

- [209] Zhaohui Yang, Yoshihisa Fujii, Fuk Kay Lee, Chi-Hang Lam, and Ophelia KC Tsui. Glass transition dynamics and surface layer mobility in unentangled polystyrene films. *Science*, 328(5986):1676–1679, 2010.
- [210] Yu Chai, Thomas Salez, Joshua D McGraw, Michael Benzaquen, Kari Dalnoki-Veress, Elie Raphaël, and James A Forrest. A direct quantitative measure of surface mobility in a glassy polymer. *Science*, 343(6174):994–999, 2014.
- [211] Heedong Yoon and Gregory B McKenna. Substrate effects on glass transition and free surface viscoelasticity of ultrathin polystyrene films. *Macromolecules*, 47(24):8808–8818, 2014.
- [212] MD Ediger and JA Forrest. Dynamics near free surfaces and the glass transition in thin polymer films: a view to the future. *Macromolecules*, 47(2):471–478, 2014.
- [213] KL Ngai, AK Rizos, and DJ Plazek. Reduction of the glass temperature of thin freely standing polymer films caused by the decrease of the coupling parameter in the coupling model. *Journal of non-crystalline solids*, 235:435–443, 1998.
- [214] D Long and F Lequeux. Heterogeneous dynamics at the glass transition in van der waals liquids, in the bulk and in thin films. *The European Physical Journal E*, 4:371–387, 2001.
- [215] Stephan Herminghaus, Karin Jacobs, and Ralf Seemann. The glass transition of thin polymer films: some questions, and a possible answer. *The European Physical Journal E*, 5:531–538, 2001.
- [216] JEG Lipson and Scott Thomas Milner. Percolation model of interfacial effects in polymeric glasses. *The European Physical Journal B*, 72:133–137, 2009.
- [217] JA Forrest. What can we learn about a dynamical length scale in glasses from measurements of surface mobility? *The Journal of chemical physics*, 139(8):084702, 2013.
- [218] Chi-Hang Lam and Ophelia KC Tsui. Crossover to surface flow in supercooled unentangled polymer films. *Physical Review E*, 88(4):042604, 2013.
- [219] JA Forrest and K Dalnoki-Veress. When does a glass transition temperature not signify a glass transition? *ACS Macro Letters*, 3(4):310–314, 2014.
- [220] Stephen Mirigian and Kenneth S Schweizer. Communication: Slow relaxation, spatial mobility gradients, and vitrification in confined films. *The Journal of chemical physics*, 141(16):161103, 2014.
- [221] Paul Z Hanakata, Beatriz A Pazmiño Betancourt, Jack F Douglas, and Francis W Starr. A unifying framework to quantify the effects of substrate interactions, stiffness, and roughness on the dynamics of thin supported polymer films. *The Journal of chemical physics*, 142(23):234907, 2015.

-
- [222] Maxence Arutkin, Elie Raphaël, James A Forrest, and Thomas Salez. Cooperative strings and glassy dynamics in various confined geometries. *Physical Review E*, 101(3):032122, 2020.
- [223] James A Forrest and Kari Dalnoki-Veress. The glass transition in thin polymer films. *Advances in Colloid and Interface Science*, 94(1-3):167–195, 2001.
- [224] Günter Reiter, Moustafa Hamieh, Pascal Damman, Séverine Sclavons, Sylvain Gabriele, Thomas Vilmin, and Elie Raphaël. Residual stresses in thin polymer films cause rupture and dominate early stages of dewetting. *Nature materials*, 4(10):754–758, 2005.
- [225] K Dalnoki-Veress, JA Forrest, PG De Gennes, and JR Dutcher. Glass transition reductions in thin freely-standing polymer films: a scaling analysis of chain confinement effects. *Le Journal de Physique IV*, 10(PR7):Pr7–221, 2000.
- [226] CB Roth and JR Dutcher. Glass transition temperature of freely-standing films of atactic poly (methyl methacrylate). *The European Physical Journal E*, 12:103–107, 2003.
- [227] CB Roth, A Pound, SW Kamp, CA Murray, and JR Dutcher. Molecular-weight dependence of the glass transition temperature of freely-standing poly (methyl methacrylate) films. *The European Physical Journal E*, 20:441–448, 2006.
- [228] Soyoung Kim and John M Torkelson. Distribution of glass transition temperatures in free-standing, nanoconfined polystyrene films: A test of de gennes’ sliding motion mechanism. *Macromolecules*, 44(11):4546–4553, 2011.
- [229] Miguel Aubouy, Manoel Manghi, and Elie Raphaël. Interfacial properties of polymeric liquids. *Physical Review Letters*, 84(21):4858, 2000.
- [230] Justin E Pye and Connie B Roth. Two simultaneous mechanisms causing glass transition temperature reductions in high molecular weight freestanding polymer films as measured by transmission ellipsometry. *Physical review letters*, 107(23):235701, 2011.
- [231] Ophelia KC Tsui. Anomalous dynamics of polymer films. *Polymer thin films*, pages 267–294, 2008.
- [232] Oliver Bäumchen, Joshua D McGraw, James A Forrest, and Kari Dalnoki-Veress. Reduced glass transition temperatures in thin polymer films: Surface effect or artifact? *Physical Review Letters*, 109(5):055701, 2012.
- [233] Daniel L Baker, Matthew Reynolds, Robin Masurel, Peter D Olmsted, and Johan Mattsson. Cooperative intramolecular dynamics control the chain-length-dependent glass transition in polymers. *Physical Review X*, 12(2):021047, 2022.

- [234] PG De Gennes. Glass transitions in thin polymer films. *The European Physical Journal E*, 2(3):201–205, 2000.
- [235] Pierre-Gilles de Gennes. Glass transitions of freely suspended polymer films. *Comptes Rendus de l'Académie des Sciences-Series IV-Physics*, 1(9):1179–1186, 2000.
- [236] Scott T Milner and Jane EG Lipson. Delayed glassification model for free-surface suppression of T_g in polymer glasses. *Macromolecules*, 43(23):9865–9873, 2010.
- [237] Jane EG Lipson and Scott T Milner. Local and average glass transitions in polymer thin films. *Macromolecules*, 43(23):9874–9880, 2010.
- [238] John D Ferry. *Viscoelastic properties of polymers*. John Wiley & Sons, 1980.
- [239] Sidney Redner. *A guide to first-passage processes*. Cambridge university press, 2001.
- [240] Pierre-Gilles de Gennes. Entangled polymers. *Physics Today*, 36(6):33–39, 1983.

RÉSUMÉ

L'objet de cette thèse est l'étude théorique de trois problèmes croisés en physique statistique hors équilibre. Le premier concerne l'étude de la réponse temporelle d'un système ionique soumis à une variation brusque d'un champ électrique extérieur. En particulier, nous étudions le comportement des fonctions de corrélation densité-densité et des courants électriques induits. En nous appuyant sur la théorie de la densité fonctionnelle stochastique et en intégrant les interactions hydrodynamiques, nous effectuons une étude complète du courant électrique total en fonction des corrélations ioniques. Nous montrons que les corrélations ne suivent pas la même trajectoire lorsque le champ est activé ou désactivé. Ainsi, le courant décroît exponentiellement lorsque le champ est désactivé, alors qu'il décroît algébriquement jusqu'à sa valeur stationnaire lorsque le champ est activé. Cette différence est due à un effet non linéaire. De plus, nous démontrons que le comportement à long terme des corrélations est dominé par un processus de diffusion anisotrope, ce qui explique la décroissance algébrique des courants. Le deuxième problème explore la diminution anormale de la température de transition vitreuse observée dans les films minces de polymères autoportés de haut poids moléculaire. En considérant les statistiques exactes de marches aléatoires de taille finie confinées entre deux plans, nous évaluons de manière critique le mécanisme original de relaxation proposé par de Gennes. Nos résultats indiquent que ce mécanisme ne permet pas d'expliquer les principales caractéristiques observées dans les expériences et qu'une nouvelle approche théorique s'avère donc être nécessaire. Enfin, le troisième problème se trouve dans l'étude des écoulements granulaires denses le long de plans inclinés. En analysant les simulations obtenues par la méthode des éléments discrets, nous retrouvons les caractéristiques essentielles des écoulements granulaires, notamment l'existence d'une contrainte critique, le profil de vitesse de Bagnold et des lois de frottement et de dilatation distinctes. Notre analyse microscopique détaillée met en évidence la formation d'amas de grains. Ces connaissances permettent le développement d'un modèle théorique de lois d'échelle, offrant une meilleure compréhension des principes régissant les écoulements granulaires denses.

MOTS CLÉS

Physique statistique hors de l'équilibre, électrolytes, polymères, matière granulaire, matière molle

ABSTRACT

In this thesis, we examine three interrelated problems within the domain of non equilibrium statistical physics using theoretical tools. These problems share the existence of long range correlations where stationary flows and disorder prevent reaching an equilibrium state. Using the distinct properties of these systems we explore different aspects of non equilibrium states. The first problem centers around the examining temporal responses of ionic systems, subject to a quench of an external electric field. In particular, we study the response of the density-density correlation functions and induced electric currents. Leveraging Stochastic Density Functional Theory and integrating hydrodynamic interactions, we analyse the total electric current as a function of ionic density-density correlation functions. The correlations do not follow the same trajectory when the field is switched on or off. Accordingly, the current decays exponentially when the field is switched off, yet it relaxes algebraically to its stationary value when the field is switched on, rooted in a non-linear effect. Moreover we demonstrate that the long range behavior of the correlations is dominated by an anisotropic diffusion process, which accounts for the algebraic decay of the currents. The second problem explores the anomalous decrease in the glass-transition temperature observed in thin freestanding polymer films of high molecular weight. We critically assess the de Gennes' sliding mechanism, which proposes a hypothetical relaxation mode by considering the exact statistics of finite-sized random walks confined between two planes. Our findings challenge the hypothesis, indicating that the sliding mechanism cannot capture the main features observed in the experiments, thus necessitating a new theoretical approach. The third problem revolves around the study of dense granular flows down inclined planes. Analyzing discrete element method simulations, we recover critical features of granular flows; including the existence of a critical stress, the Bagnold velocity profile, and distinct friction and dilatancy laws. Our microscopic analysis uncovers the formation of grain clusters. These insights permit the development of a theoretical scaling model, providing a comprehensive understanding of the principles governing dense granular flows.

KEYWORDS

Non-equilibrium statistical physics, electrolytes, polymers, granular matter, soft matter